

DETERMINATION OF UPPER MANTLE HETEROGENEITY BENEATH  
AEGEAN-ANATOLIAN REGION FROM TRAVEL TIME  
TOMOGRAPHY

by

Dođan Aksarı

B.S., Geophysical Engineering, İstanbul Technical University, 2001

M.S., Geophysics, Bođaziçi University, 2006

Submitted to the Kandilli Observatory and  
Earthquake Research Institute in partial fulfillment of  
the requirements for the degree of  
Doctor of Philosophy

Graduate Program in Geophysics

Bođaziçi University

2019

To my wife Canan,

## ACKNOWLEDGEMENTS

I wish to express my deepest gratitude to my advisor Prof. Dr. Hayrullah Karabulut for his valuable advices and guidance of this work.

The Kandilli Observatory and Earthquake Research Institute (KOERI), at the Boğaziçi University (BU), The Scientific and Technological Research Council of Turkey (TÜBİTAK) - Marmara Research Center (MRC) and Republic of Turkey Prime Ministry - Disaster & Emergency Management Authority - Presidential of Earthquake Department (AFAD) provided support, including data, laboratory and office work.

I also want to express my gratitude to the department members, staff, and students of the Department of Geophysics, the members of Regional Earthquake-Tsunami Monitoring Centre (RETMC) and the members of the KOERI, BU.

I want to thank also to Dr. Anne Paul from the Institute des Sciences de la Terre (France) for providing the **Seismic Imaging of the Mantle Beneath the Aegean-Anatolian Domain (SIMBAAD)** data. She also provided guidance on Teleseismic Tomography analysis. I would like to thank Dr. Nick Rawlinson for providing Teleseismic Tomography Code.

I am deeply indebted to my friend Tuğçe Afacan Ergün whose assistance and encouragement made this work possible towards the end.

Finally, I am particularly grateful to my parents, for helping and assisting me in all the stages of this work. Without their help, this study would never have been possible. Special thanks to my wife for her patience and support.

## ABSTRACT

### **DETERMINATION OF UPPER MANTLE HETEROGENEITY BENEATH AEGEAN-ANATOLIAN REGION FROM TRAVEL TIME TOMOGRAPHY**

The objective of this work is to determine the heterogeneities of the upper mantle in the Aegean-Anatolian domain using teleseismic tomography. A waveform dataset was prepared from 798 teleseismic earthquakes with magnitudes greater than 5.5 between January 2004 and December 2015. 417 stations from permanent and temporary networks with more than 64,000 direct P phases are used in the computations. The relative travel times of P waves with respect to the ak135 (Kennett et al. 1995) earth model are computed using waveform cross-correlations technique.

The tomographic images are computed as perturbations with respect to ak135 earth model. An algorithm named as fast marching method (FMM) (Sethian, 1996a, 1996b) based on the solution of Eikonal equation is used in the forward computation of the travel times. The inversion is performed using subspace inversion scheme. Trade-off curves are plotted and several synthetic tests are performed in order to select optimum parameters (damping and smoothing) for tomography and the resolution and model roughness were investigated. The tomographic images obtained to a depth of 700 km.

The computed tomographic images show a heterogeneous upper mantle structure in the Aegean-Anatolian domain. The results are similar to the previously published images mostly but provides higher resolution for the study area. Both Hellenic and Cyprus subductions are imaged to the depth of 700 km. The tear (Pliny-Strabo Tear) between two subduction zones is clearly observed reaching to 660 km discontinuity. A smaller scale tear (Antalya Bay Tear) is also observed on the Cyprus slab around Paphos Transform Fault. The Anatolian plate is underlined by low velocity mantle material with thickness increasing from west to east. The northern block of the North Anatolian Fault (NAF) is observed as high velocity body observable to a depth of 100-200 km. NAF has a sharp velocity contrast between the north and south.

## ÖZET

### **EGE-ANADOLU BÖLGESİNİN ALTINDAKİ ÜST MANTO YAPISININ TELESİSMİK TOMOGRAFİ YÖNTEMİ İLE GÖRÜNTÜLENMESİ**

Bu çalışmanın amacı, teleseismik tomografi kullanarak Ege-Anadolu bölgesi üst mantosunun heterojenliğini tespit etmektir. Ocak 2004 ile Aralık 2015 arasında  $M > 5.5$  olan 798 teleseismik depremden oluşan bir veri seti hazırlanmıştır. Hesaplamalarda, kalıcı ve geçici ağırlara ait 417 istasyon ve 64.000'den fazla P fazı kullanılmıştır. ak135 hız modelini göre çapraz korelasyon tekniği kullanılarak P dalgalarının bağıl hareket süreleri hesaplanmıştır.

Tomografik görüntüler ak135 hız modeline göre pertürbasyonlar olarak hesaplanmaktadır. Seyahat sürelerinin düz hesaplanmasında, Eikonal denkleminin çözümüne dayanan FMM olarak adlandırılan bir algoritma kullanılır. İnversiyon, Subspace inversiyon yöntemi kullanılarak gerçekleştirilir. Tomografi için optimum parametreleri (sönüm ve yumuşatma) seçmek amacıyla trade-off eğrisi çizilerek ve çeşitli sentetik testler yapılarak çözünürlük ve model pürüzlülüğü araştırıldı. Tomografi görüntüleri 700 km derinliğe ulaştı.

Hesaplanan tomografik görüntüler Ege-Anadolu bölgesinde heterojen bir üst manto yapısı göstermektedir. Sonuçlar daha önce yayınlanmış görüntülere benzer ancak çalışma alanı için daha yüksek çözünürlük sağlar. Hem Ege hem de Kıbrıs dalma-batma zonları 700 km derinliğe kadar görüntülendi. İki alt bölge arasındaki yırtılmanın (Pliny-Strabo Yırtığı) 660 km süreksizliğe ulaştığı açıkça gözlenmektedir. Paphos Transform Fayı çevresindeki Kıbrıs dalan levhası üzerinde daha küçük ölçekte bir yırtık (Antalya Körfezi Yırtığı) gözlenmektedir. Anadolu plakası, kalınlığı batıdan doğuya doğru artan düşük hızlı manto malzemesi üzerinde görülmektedir. Kuzey Anadolu Fayı'nın kuzeybatı bloğu (KAF) 100-200 km derinliğe kadar gözlemlenebilen yüksek hızlı bir cisim olarak görülmektedir. Kuzey Anadolu Fayı'nın kuzeyi ve güneyi arasında keskin bir hız kontrastına görülmektedir.

## TABLE OF CONTENTS

ACKNOWLEDGEMENTS .....	iv
ABSTRACT.....	v
ÖZET .....	vi
TABLE OF CONTENTS.....	vii
LIST OF FIGURES .....	ix
LIST OF SYMBOLS .....	xiv
LIST OF ACRONYMS / ABBREVIATIONS .....	xv
1. INTRODUCTION.....	1
2. REGION OF INTEREST: AEGEAN – ANATOLIAN REGION.....	3
2.1 Tectonic Setting of the Region .....	3
2.2 Previous Studies.....	7
2.3 Seismicity.....	13
3. METHODOLOGY .....	16
3.1 Model Parameterization .....	16
3.2 Forward Calculation .....	18
3.2.1 Ray-based Methods.....	18
3.2.2 Grid-based Methods.....	19
3.3 Inversion .....	21
3.3.1 Backprojection .....	22
3.3.2 Gradient Methods .....	23
4. TELESEISMIC TRAVELTIME TOMOGRAPHY .....	28
4.1 Data.....	28
4.1.1 Event Distribution and Data Preparation .....	29
4.1.2 Statistics of the Catalog .....	36
4.1.3 Crustal Correction.....	38
4.2 Model Parameterization and Ray Tracing .....	38
4.3 Selecting Smoothing and Damping Parameter .....	39
4.4 Resolution Test and Data Coverage.....	41
4.5 Results.....	45

4.6 Discussion.....	50
5. CONCLUSIONS.....	57
REFERENCES .....	58

## LIST OF FIGURES

- Figure 2.1. Tectonic map shows the fundamental active structures (see Jolivet et al., 2013 for the detailed description for the denotations). ..... 3
- Figure 2.2. Ff cross sections belong to the study volume. The length of the cross section is  $\sim 20^\circ$ . 2<sup>nd</sup> figure indicates the models, 3<sup>rd</sup> figure indicates the recovery tests and at the 4<sup>th</sup> figure the ray density distribution is plotted. They observed the fast material belong to Aegean slab from the surface to the bottom frontier of their model. They also found a low velocity amplitude at the Aegean basin, north of the Hellenic trench (Piromallo and Morelli, 2003). ..... 7
- Figure 2.3. (a), (b), (c), (d) show the map views of tomographic results at 150, 350, 650 and 900 km and (e) cross-section CC' is taken from PM0.5. CC' indicates that the positive velocity anomalies come from the upper mantle continue to the mid-mantle. (f) panel indicates the box-car recovery test which is located the same location of the slice at CC' (Faccenna et al., 2003). ..... 8
- Figure 2.4. Comparison of four different tomographic models. Four horizontal layers plotted for the models; 70, 150, 300, and 450 km. (Facenna et al., 2014). .... 9
- Figure 2.5. Cross sections of four tomographic models of Figure 2.4 (Facenna et al., 2014). ..... 10
- Figure 2.6. Interpretation of the five section across the study area. AA': 39°N; B'B: 40°N23°E-35°N30°E; CC': 34°N30°E-42°N32°E; DC': 34°N33°E-42°N32°E; EE': 28.5°E (See Biryol et al. (2011) for detailed location of the slices and explanations). ..... 11

Figure 2.7.	The results of the teleseismic tomographic by Portner et al. 2018. Shading area restricted by a solid black line show the 0.5 hit quality contour. Green circles are earthquake locations. Red triangles indicate volcanoes. See Portner et al. 2018 for the abbreviations and other details.....	12
Figure 2.8.	Cross sections through the tomography model by Portner et al. 2018. Locations of the slices are shown at Figure 2.7A with white dashed lines. Topography and tectonic features are labeled above the profiles. See Portner et al. 2018 for the abbreviations and other details.....	13
Figure 2.9.	Seismicity of the eastern Mediterranean region for the period of 1999-2019 with magnitudes greater than or equal to 2.5 (EMSC Catalog). .....	14
Figure 2.10.	Focal mechanisms of earthquakes over the Aegean Anatolian region (Modified from Jolivet et al., 2013). .....	15
Figure 3.1.	2D velocity field defined using (a) constant velocity blocks; (b) cubic B-spline patches (Rawlinson et al., 2010). .....	17
Figure 3.2.	Two different models; continuous and discontinuous changes in seismic property (a) interfaces of the layers continuous horizontally and seismic structure $wi(x, z)$ changes smoothly; (b) interfaces of the layers set up irregularly and seismic structure $wi(x, z)$ changes smoothly (Rawlinson and Sambridge, 2003). .....	17
Figure 3.3.	Representation of the two basic approaches to ray-tracing: (a) shooting and (b) bending. For shooting, trajectory of the initial ray at the source is perturbed until the receiver is reached. For bending, and initial path (not a ray-path) connecting the source and receiver is perturbed until a ray-path is reached (redrawn from Thurber, 1993). .....	19
Figure 3.4.	Principle of the narrow band method. See text for detail (Rawlinson and Sambridge, 2003). .....	21

Figure 3.5.	Principal of the FMM in 2-D. See text for detail (Rawlinson and Sambridge, 2003). .....	21
Figure 3.6.	Trade-off curves to choose appropriate damping or smoothing parameters for an inversion. (a) Model perturbation for values of $\epsilon$ and data fit. (b) Model roughness for values of $\eta$ and data fit (Rawlinson and Sambridge, 2003). .....	23
Figure 4.1.	Station distribution used in this study. Blue triangles indicate Turkey, Greece and Cyprus permanent broadband stations, Red, Green and Pink stars indicate SIMBAAD broadband temporary stations. Green stars indicate west profile and pink stars indicate east profile. ....	28
Figure 4.2.	Distribution of the 798 teleseismic events (red circles) used in the tomographic inversion. Straight black circles indicate 30°, 60°, 90° and 120° the great circle distance from the study area. ....	29
Figure 4.3	Data preparation steps. ....	30
Figure 4.4.	Examples using various events from different locations: The top figure shows the map of station residuals for each event. Residuals (in seconds) are calculated the relative to the picked arrival times after alignment. The title of each map shows the details of the event. Red circles indicate negative arrival time residuals and blue circles positive. Inset world map show the location of the study area and epicenter of the event. Event depth, nearest and far Great circle arc distances between event and stations, back-azimuth of event to the center of the study area are also shown on the inset map. The legend of the size of the residuals can be found at the upper right corner of the map. ....	32
Figure 4.5.	Number of observation of each station. The red squares show the magnitude of the number of observations. ....	36

- Figure 4.6. RMS of travel time residuals calculated from ak135. The size of the circle is proportional to the magnitude of the RMS in seconds. ....37
- Figure 4.7. Standard deviation of travel time residuals calculated from ak135. The circles are scaled with the magnitude of the standard deviation in seconds. ....38
- Figure 4.8. Ak135 velocity model used for constructing initial model. Blue line indicates P-wave velocity and red line indicates S-wave velocity regarding depth. ....39
- Figure 4.9. Trade-off curves used to estimate optimum smoothing and damping parameters. (a) Damping parameter fixed at  $\varepsilon = 5.0$  and smoothing parameter is changing. In this case,  $\eta = 10.0$  is chosen from the curve. (b) Smoothing parameter fixed at  $\eta = 10.0$  and damping parameter is changing. The value  $\varepsilon = 5.0$  is chosen as optimum. ....40
- Figure 4.10. Frequency histograms showing fit to observed arrival time residual data of (a) .....41
- Figure 4.11. Synthetic checkerboard resolution test results. The 1<sup>st</sup> and 2<sup>nd</sup> row show horizontal slices taken through the input model at 150, 300, 450, 600 km depth and the recovered pattern of anomalies for the same depth. The 3<sup>rd</sup> and 4<sup>th</sup> rows show EW Cross-sections taken through the input at 37.0°N, 38.5°N and 40.0°N and the recovered pattern of anomalies for the same latitude with input model. The 5<sup>th</sup> and 6<sup>th</sup> rows show that NS Cross-sections taken through the input at 23.5°E, 27.5°E, 31.5°E, 35.5°E and the recovered pattern of anomalies for the same longitude with input model. ...43
- Figure 4.12. Synthetic spike resolution test results. The 1<sup>st</sup> and 2<sup>nd</sup> rows show horizontal slices taken through the input model and recovered pattern of anomalies at 150, 300, 450 and 600 km depth. The 3<sup>rd</sup> and 4<sup>th</sup> rows show Cross-sections through the input model and recovered pattern of anomalies at 37.0°N and 38.0°N. 5<sup>th</sup> and 6<sup>th</sup> rows show Cross-sections

	through the input model and recovered pattern of anomalies at 23.0°E, 27.0°E, 31.0°E and 35.0°E.....	44
Figure 4.13	Horizontal sections through the three-dimensional final model from 50 km to 750 km with 50 km intervals as P-wave velocity perturbations from a reference one-dimensional model. ....	47
Figure 4.14.	Cross-sections through the three-dimensional solution model at 0.5° intervals from 35.0°N to 39.5°N in East-West direction. ....	48
Figure 4.15.	Cross-sections through the three-dimensional solution model at 0.5° intervals from 22.5°E to 37°E in North-South direction.....	49
Figure 4.16	Map of study area including tectonic provinces, major structural features. Green dashed lines show the location of the cross sections tomograms shown in Figure 4.17 and Figure 4.18.....	54
Figure 4.17	Cross sections taken through the A1-A1' (39.0°N) and A2-A2' (37.0°N) profiles. Small white circles are the earthquake hypocenters ( $M_w \geq 4.0$ ) for the period 1973-2017 taken from USGS. Topographic profiles are plotted at the top of the images with the 10x exaggeration. Green line indicates bottom line of the crust. Black dashed horizontal lines indicate 410 km and 660 km discontinuities. Red colors indicated slow velocities and blue color indicates fast velocities.....	55
Figure 4.18	Cross sections taken through the B-B' (25.0°E), C-C' (27.0°E), D-D' (28.5°E), E-E' (30.5°E), F-F' (33.0°E), G-G' (35.0°E), and H-H' (37.0°E) profiles. See Figure 4.17 for details. ....	56

## LIST OF SYMBOLS

$d$	observations
$dl$	differential path length
$\mathbf{d}$	traveltime perturbations
$\mathbf{G}$	coefficient Matrix - ray length
$\mathbf{G}$	Fréchet matrix
$\hat{\mathbf{H}}$	hessian matrix
$m_0$	initial model
$m$	model parameters
$\mathbf{m}$	slowness perturbations
$n$	dimension of model space
$R$	receiver
$s$	slowness
$S$	source
$S(\mathbf{m})$	objective function
$t$	travel time
$v$	velocity
$\vec{x}$	position vector
$\nabla T$	traveltime gradient
$\hat{\mathbf{y}}$	gradient vector
$\delta\mathbf{m}$	perturbation to the current model
$\epsilon$	damping factor
$\eta$	smoothing factor
$\phi_n$	set of conjugate directions
$\Phi(\mathbf{m})$	regularization term
$\Psi(\mathbf{m})$	difference between the observed and predicted data
$\Omega(\mathbf{m})$	regularization term

## LIST OF ACRONYMS / ABBREVIATIONS

AFAD	Republic Of Turkey Prime Ministry - Disaster & Emergency Management Authority - Presidential of Earthquake Department
ak135	Travel Time Tables Developed by B.L.N. Kennett
ART	Algebraic Reconstruction Technique
BD	Bey Daglari
CA	Central Anatolia
CAP	Central Anatolia Province
CAVZ	Central Anatolia Volcanic Zone
CG	Conjugate Gradient
EACP	The East Anatolian Contractional Province
EAF	East Anatolian Fault
EAFZ	East Anatolian Fault Zone
EMSC	European Mediterranean Seismological Center
FBFZ	Fethiye-Burdur Fault Zone
FM	Fréchet matrix
FMM	Fast Marching Method
FMTT	Fast Marching Teleseismic Tomography
G-N	Gauss-Newton
HP-LT	High Pressure-Low Temperature
HT-LP	High Temperature-Low Pressure
KAF	Kuzey Anadolu Fayı
KAIVF	Kirka-Afyon-Isparta Volcanic Fields
KOERI	Kandilli Observatory and Earthquake Research Institute
KVF	Kula Volcanic Fields
MRC	Marmara Research Center
NAF	North Anatolian Fault
NAFZ	North Anatolian Fault Zone
NAP	North Anatolian Province
NCDS	North Cycladic Detachment System
OF	Objective Function

PREM	Preliminary Reference Earth Model
q-N	quasi-Newton
RETMC	Regional Earthquake-Tsunami Monitoring Center
SAC	Seismic Analysis Code
SD	Steepest Descent
SIMBAAD	Seismic Imaging of the Mantle Beneath the Aegean-Anatolian Domain
SIRT	Simultaneous Iterative Reconstruction Techniques
SiM	Subspace Inversion Method
STEP	Subduction Transform Edge Propagator
SVD	Singular Value Decomposition
TÜBİTAK	The Scientific and Technological Research Council of Turkey
USGS	United States Geological Survey
WAEP	Western Anatolia Extensional Province

## 1. INTRODUCTION

One of the objective of seismology is to determine the internal structure of the earth from earth's physical properties such as velocity and density. Seismic waves generated by earthquakes greater than certain magnitude, travels throughout the Earth. By studying the propagation characteristics (travel times, dispersion, etc.) of seismic waves for the last century, we have learned much about the Earth's interior.

On global scale, the earth's internal structure is simple. The Earth's interior is divided into roughly two parts, core and mantle. The global earth models, PREM (Dziewonski and Anderson 1981) and ak135, are characterized by the average properties of the radially symmetric earth varying with depth only. However, if we are interested in the part of lithosphere (e.g., crust and uppermost mantle) we need more information and detailed models. The strong lateral heterogeneities are observed in the presence of subducting lithosphere and thermal anomalies in the upper mantle. Among many observations and methodologies, seismic tomography has provided major contributions to our knowledge of the Earth.

Seismic tomography is the technique of imaging zones of complex, heterogeneous velocity and attenuation structure of earth by using redundant measurements of some property of seismic waves (Iyer, 1989). Teleseismic tomography is a powerful tool used to obtain about the deep velocity perturbations in the Earth, using travel times recorded by a regional network from distant sources. Teleseismic tomography was developed by Aki (Aki et al., 1977) and has been used for different regions (Achauer et al., 1992; Evans and Achauer, 1993; Kulakov et al., 1995, Wittlinger et al., 1998). The results of tomography are used for the estimation of the appraisal of temperature, density and other parameters (Sobolev et al., 1996).

To investigate the structure of the upper mantle beneath Aegean-Anatolian region, we performed teleseismic tomography. Our objective is to provide better constraints on the structure of the subducting African lithosphere. This study was motivated by the goal of further enhancing the resolution of the tomographic image in the study area.

In the second chapter, tectonic setting of the study area is summarized and some major tectonic structures are mapped. Results of the previous studies are summarized. The seismological characteristics of the region are presented with details.

In Chapter 3, the tomographic methods are summarized: model parameterization, forward calculation and inversion methods are explained in details.

Chapter 4 presents the application steps of the teleseismic tomography: the data processing, model parameterization, selection of smoothing and damping parameters, and resolution tests. Finally, the results are presented and discussed with the tectonics of the region and compared with the previous studies.

## 2. REGION OF INTEREST: AEGEAN – ANATOLIAN REGION

### 2.1 Tectonic Setting of the Region

The collision of the Arabian and the Eurasian plates (Figure 2.1) along a localized collision front controls the tectonic escape of the Anatolian plate (Barka and Kadinski-Cade, 1988). This movement is accomplished along two major strike-slip boundaries; the right-lateral NAF and the left-lateral East Anatolian Fault Zones (EAFZ) (Figure 1). The right-lateral NAF extends for about 1200 km from eastern Turkey to Aegean Sea in an arc parallel to the Black Sea coast (Ketin, 1948). Over much of its length, the fault is simple and single structure and takes up most of the strain associated with the westward movements of the Anatolian plate. In western Turkey, the fault splits into two main strands in the Marmara region and its passage across the Aegean is more complicated.

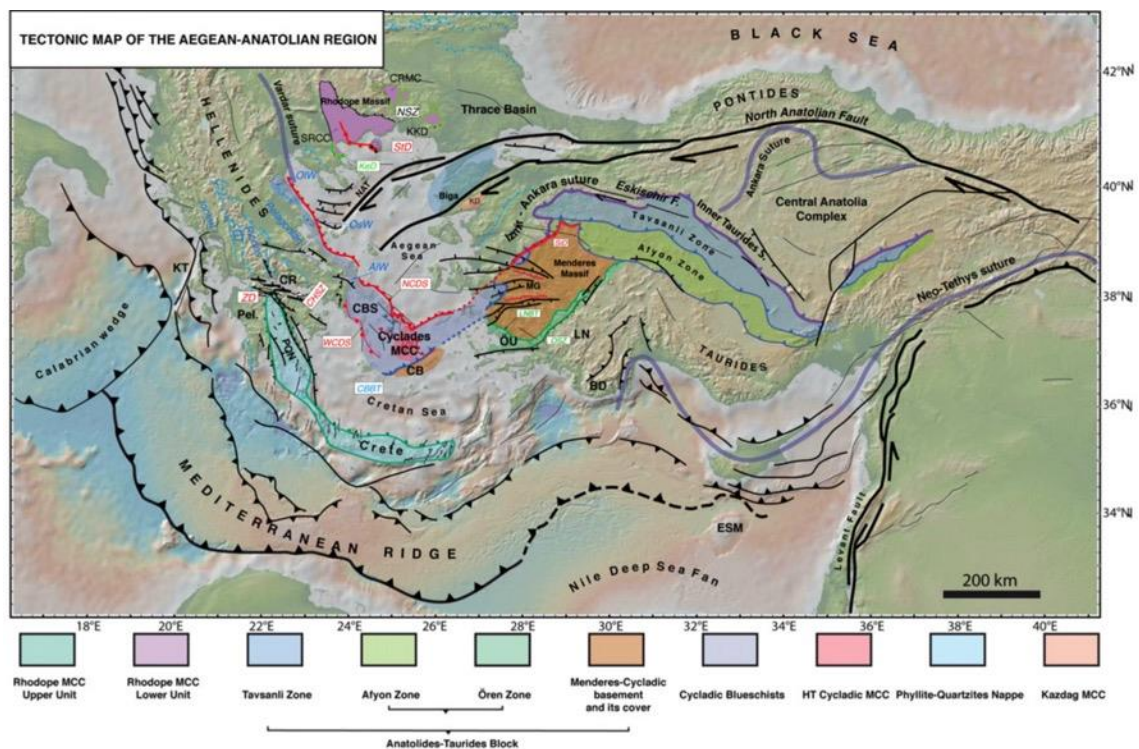


Figure 2.1. Tectonic map shows the fundamental active structures (see Jolivet et al., 2013 for the detailed description for the denotations).

The North Aegean Sea, continental Greece and western Turkey are currently undergoing a continental lithospheric extension in from the N-S and the NE-SW direction (McKenzie, 1978; Le Pichon and Angelier, 1981; Şengör et al., 1985). However, different views exist on the driving mechanism. Some authors associate the extension with slab pull of retreating Aegean Subduction Zone due to asthenospheric flow (McKenzie, 1978; Le Pichon and Angelier, 1981). Some authors declare the interaction of the Arabian plate with Eurasia and the apparent extrusion of Anatolia towards the west from the zone of most intense convergence where stresses transmitted horizontally through the crust (McKenzie, 1978; Dewey and Şengör, 1979; Taymaz et al., 1991). Others suggest orogenic collapse causes extension by thinning of the thickened crust coming after the termination of the Neotethys Ocean (Seyitoğlu & Scott 1991; Seyitoğlu et al. 1992). Aegean region is under the influence of extension after all the late Eocene-Early Oligocene ~35 Ma (Jolivet and Brun, 2010; Jolivet and Faccenna, 2000) but the initiation of the extension and subduction was expected 13 Ma old (Le Pichon and Angelier, 1979). Previous works (e.g. Jolivet and Brun, 2010) on the Aegean Sea describe the longtime deformation of the Aegean Sea and the exhumation of extensional metamorphic cores. This description shows the interaction between strike-slip movement along the NAF and extension in the Aegean region (Armijo et al., 1996, 1999, 2003). Armijo et al., 1992 reported that in Evia and the Corinth Rift active extension is recorded in the prolongation of NAF. In the backarc domain and the accretionary wedge, metamorphic units (High Pressure-Low Temperature HP-LT or High Temperature-Low Pressure HT-LP) which originates below crustal-scale detachments faults and extensional ductile shear zones (Brun and Faccenna, 2008; Ring et al., 2007, 2010) are observed. However, some places in Aegean such as the North Cycladic Detachment System (NCDS), there is a lithospheric scale detachment (Jolivet et al., 2013). According to Jolivet et al., 2013 Cycladic metamorphic core complexes have two-phase results. In the first phase, there is crustal thickening in HP-LT condition in the Eocene near the front of the subduction (accretionary wedge) and in the second phase there is crustal thinning under HT-LP conditions in the backarc region. Previous tomographic studies showed that below the Aegean region, the structure of the lithosphere is very thin (Piromallo and Morelli, 2003; Salaün et al., 2012). The crust below the Cretan Sea and the North Aegean Trough is about 15 km (Sodoudi et al., 2006; Tirel et al., 2004). The geometry of the African Slab is presented with the recent tomographic studies (Van Hinsbergen et al., 2010; Biryol et al., 2010; Portner et al., 2018) which showed that there are three major tears along the 1500 km long slab. One

major tear, which divides the slab into two parts, is located below the Western Turkey and the second is located under the Corinth Rift and Kephallonia fault (van Hinsbergen et al., 2010; Suckale et al., 2009). The third one is located on the Cyprus slab.

WA is enclosed with the Aegean extensional domain, where the topography was built by the grabens and the core complexes. These structures formed an orogenic wedge (Figure 1). Although the age of the mechanisms controlling extension varies from 5 Ma to 60 Ma (Bozkurt, 2001), Bozkurt and Sözbilir, 2004 reported that N-S extension started in the Late Oligocene-Early Miocene (30 Ma). WA can be divided into several metamorphosed units in the north Anatolides and in the south Taurides (Bozkurt and Oberhänsli, 2001). Anatolides consists of different regions, Tavşanlı zone that consists of distal sediments and volcanic rocks (Cetinkaplan et al., 2008; Okay, 2002), while Afyon zone and Ören unit are composed of low-grade HP metamorphism (Rimmelé et al., 2006; Oberhänsli et al., 2001). Menderes Massif is also composed of metamorphic material (Bozkurt and Oberhänsli, 2001). Simav detachment is the most essential one, which assumed a noteworthy role in shaping the northern part of the Menderes Massif (Isik et al., 2004; Ring and Collins, 2005). The crust of the Menderes Massif (30 km) is thicker than in the Cyclades (25 km) (Jolivet et al., 2013) but thinner than Central Anatolia (CA) (35 km) (Mutlu and Karabulut, 2011).

North Anatolian Fault Zone (NAFZ) is described E-W striking right lateral strike slip faults. NAFZ follows the north margin of the Anatolian Plate (Koçyiğit, 1996; Bozkurt 2001; Şengör et al. 2005), is ~5-7 Ma old and has ~25-85 km offsets cumulatively (Bozkurt 2001; Şengör et al. 2005). Latest geophysical studies showed that the crustal thickness around the NAFZ ~25-40 km (Laigle et al. 2008; Becel et al. 2009; Özacar et al. 2010).

EAFZ and NAFZ bounds CA and causes it to extrude westward along fault zones. CA is the westernmost part of the Iranian-Anatolian high plateau at an average altitude of 1.5 km. The uplift of the central Anatolian plateau is recent (8 Ma; Schildgen et al., 2014) and assumed to be related to delamination and slab break-off on its propagation from EA. SW-NE strike slip faults are the main tectonic elements of this region. Some of these structures are related to the convergence between African and Anatolian Plates and counterclockwise rotation of the Anatolian block (Reilinger et al. 1997; Taymaz et al. 2007a,b). Although CA has a flat topography compared to Western and Eastern Anatolia. This area is additionally

portrayed by ~13 Ma to Recent post-collision associated volcanism that was trailed by emplacement of a few stratovolcanoes (Notsu et al. 1995). Its transitional character is attested by undisturbed Miocene sediments observed at an elevation > 1000 km (Cosentino et al., 2012). The present-day internal deformation there appears to be significantly less than in western and eastern Anatolia as observed from seismic activity.

Isparta angle is the frontier between the WA and CA and is one of the most complex area in the region. Sultandağı Fault with the NW-SE striking (Boray et al. 1985) at the north to the east, Fethiye-Burdur Fault Zone (FBFZ) with the NE-SW striking at the north to the west and Anaximander Mountains at southwest bounded Isparta angle (Taymaz and Price 1992; Price and Scott 1994).

After geodetic data have become available, a significant development was made on the active tectonics of the Aegean-Anatolian region (Kahle et al., 1995, Le Pichon et al., 1995 and McClusky et al., 2000). GPS studies have shed light on some of the questions related to the motion of the plates involved in the regional tectonics. Reilinger et al. (2006) studied secular velocity field at the zone of interaction of the Nubian, Somalian, Arabian and Eurasian plates for the period 1988-2005. They observed that the velocity field (see Reilinger et al. (2006)) shows a counterclockwise rotation (similar to asthenospheric flow) with a radius of ~1200 km of a broad area including the Aegean, Arabian and Anatolian regions and central Iran and Zagros (Le Pichon and Kreemer, 2010). Rates of motion associated with this rotation increase towards the Hellenic-Cyprus trench system (Floyd et al., 2010; Aktug et al., 2009; Reilinger et al., 2010; Le Pichon and Kreemer, 2010). According to Reilinger et al. (2006), this increasing rate of motion towards the Hellenic and Cyprus trenches suggests that the primary forces responsible for westward motion of Anatolia, and perhaps counterclockwise rotation of Arabia, are associated with slab roll-back along the Hellenic and Cyprus trenches.

According to Faccena et al. (2006), the initiation of the NAF and the escape of Anatolia to the west may also have been triggered by slab break-off at the Bitlis suture and its propagation to the west. The rollback of the Hellenic slab that started in the late Miocene also made contribution to the motion of Anatolia and its acceleration towards arc that is clearly documented by GPS velocities (Reilinger et al., 2006).

## 2.2 Previous Studies

Piromallo and Morelli (2003) performed seismic travel time tomography to determine the structure of the upper mantle P wave velocity through the Euro-Mediterranean area, down to 1000 km depth. They observed large-scale fast anomalies and they suggested that in the western central Europe, the mantle dynamics is dominated by blockage of subducted slabs at the 660 km discontinuity and ponding of seismically fast material in the transition zone; in contrast, in the eastern Mediterranean, fast velocity material sinks into the lower mantle (Figure 2.2), suggesting that the flow of the cold downwelling here is not blocked by the 660 km discontinuity. There was no evidence of the existence of tears in the subducted slab in their tomographic images.

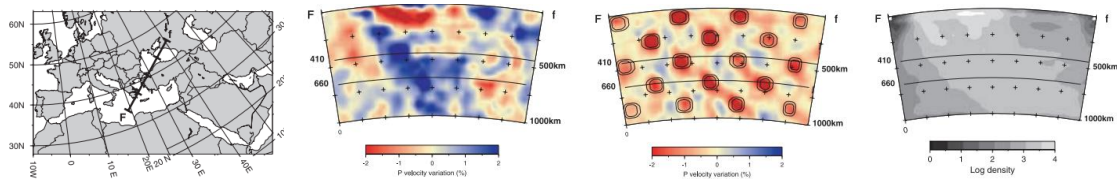


Figure 2.2. Ff cross sections belong to the study volume. The length of the cross section is  $\sim 20^\circ$ . 2<sup>nd</sup> figure indicates the models, 3<sup>rd</sup> figure indicates the recovery tests and at the 4<sup>th</sup> figure the ray density distribution is plotted. They observed the fast material belong to Aegean slab from the surface to the bottom frontier of their model. They also found a low velocity amplitude at the Aegean basin, north of the Hellenic trench (Piromallo and Morelli, 2003).

(Faccenna et al., 2003) have studied the region by combining geological data, paleotectonic reconstruction, plate motion, and tomographic analysis to investigate the structure of the subduction and backarc extension of the central Mediterranean and eastern. They identified a long slab-like feature that penetrates in the mid-mantle from their tomograms (Figure 2.3). They also noted the accumulation of cold material at the mid-mantle and the transition zone.

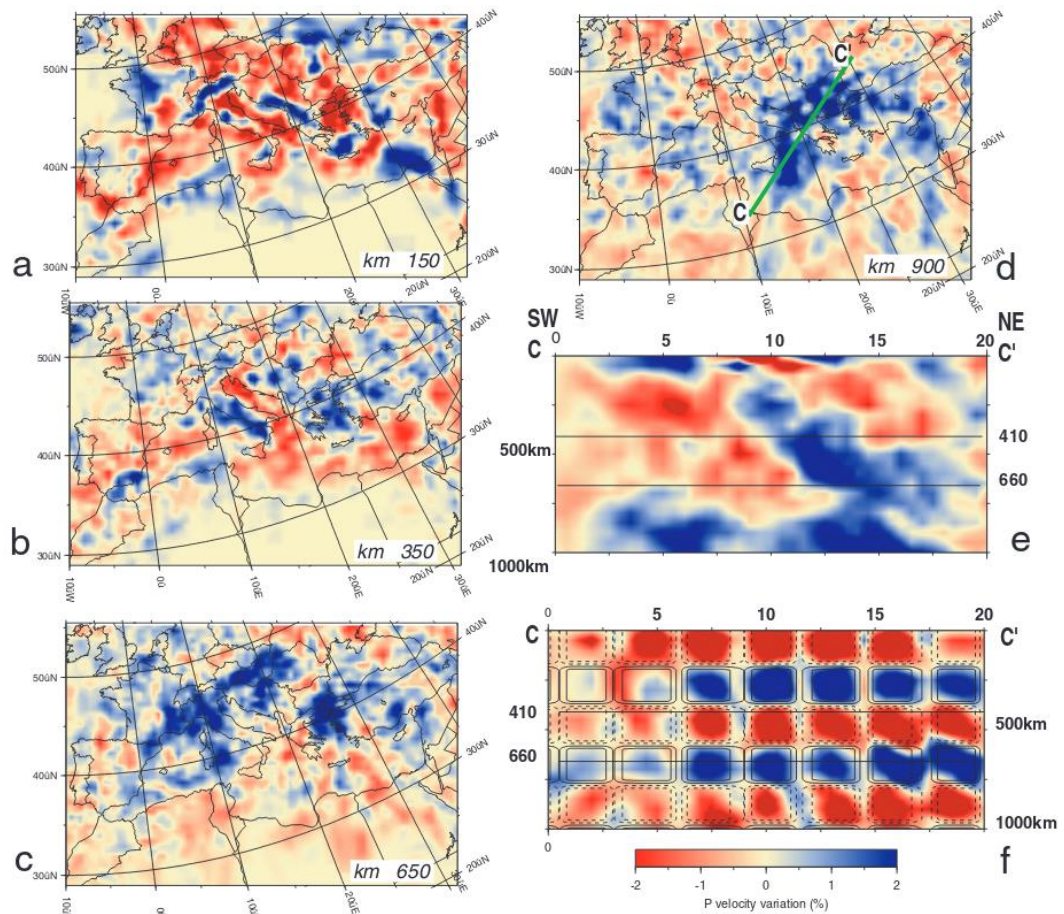


Figure 2.3. (a), (b), (c), (d) show the map views of tomographic results at 150, 350, 650 and 900 km and (e) cross-section CC' is taken from PM0.5. CC' indicates that the positive velocity anomalies come from the upper mantle continue to the mid-mantle. (f) panel indicates the box-car recovery test which is located the same location of the slice at CC' (Faccenna et al., 2003).

Faccenna et al., 2014 combined and discussed the result of different seismic tomography models (SAVANI [Auer et al., 2014] and (b) EU30 [Zhu et al., 2012] and P wave models (c) MITP08 [Li et al., 2008] and (d) PM0.5 [Piromallo and Morelli, 2003]). Figure 2.4 shows the map views at different depths of each model. Model c and d only use body waves, while a and b use surface waves as well. The tomographic models have different resolutions. At large scale we can see high wave speed of the East European Platform, Armorican Massif, east-Mediterranean Sea and Adriatic Plate and the low velocities of central and eastern Europe, western Mediterranean and Tyrrhenian basins, Pannonian Basin and Anatolian Plate at 70 km tomogram. At small scale, EU30 and PM0.5 models show a

good result at our study area. High velocity anomaly at southern Aegean and eastern Mediterranean indicate subducted lithosphere. At 150 km, same structures still exist at EU30 and PM0.5 models. All models have similar large-scale anomalies at 300 km. Deeper part from 300 km models show differences because of the data and vertical resolution. High velocity anomalies are located at the Aegean and WA at the entire model except EU30.

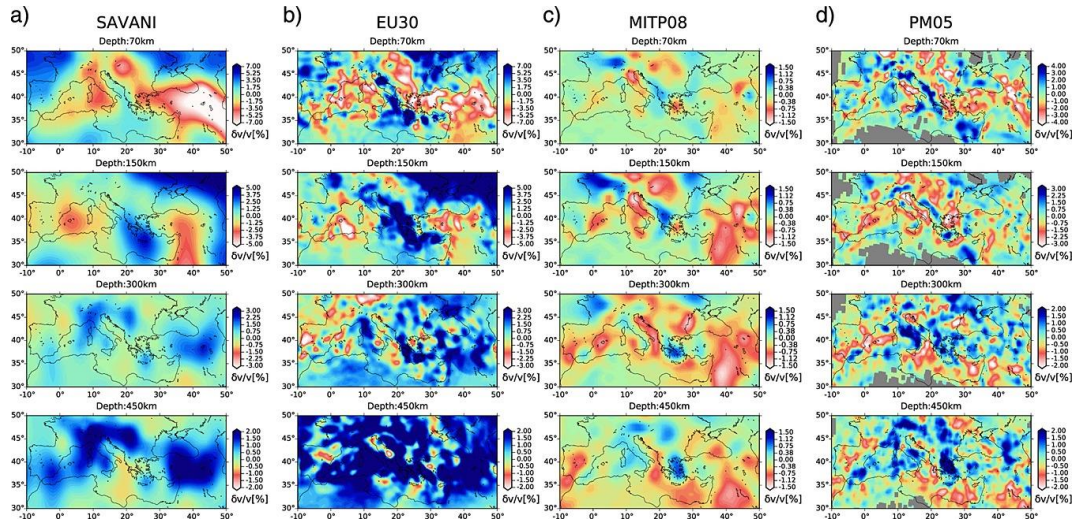


Figure 2.4. Comparison of four different tomographic models. Four horizontal layers plotted for the models; 70, 150, 300, and 450 km. (Facenna et al., 2014).

Figure 2.5 shows vertical cross sections. All models show the high velocity anomalies between  $20^{\circ}$ - $30^{\circ}$  along Aa profile. These anomalies indicate Hellenic and Calabrian arcs. Aegean slab anomaly is thicker and clearer than the other especially in EU30, MITP08 and PM05. Except above 200 km at MITP08, EU30, MITP08 and PM05 show a good correlation showing Aegean slab at Bb. As a result, the models are dominated by the high-velocity zones of the Aegean slab and low-velocity zones are usually concentrated in back-arcs.

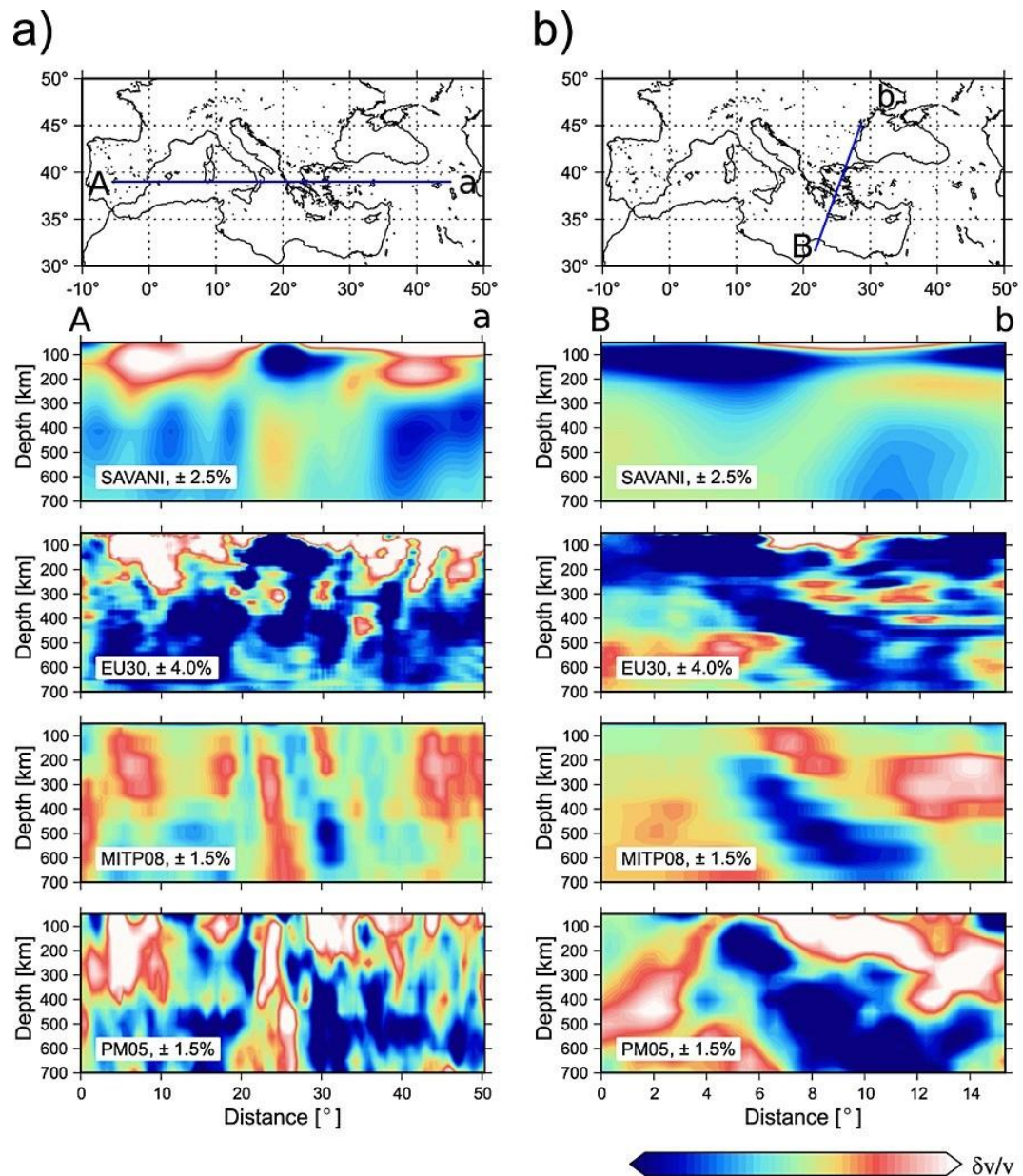


Figure 2.5. Cross sections of four tomographic models of Figure 2.4 (Facenna et al., 2014).

Biryol et al. (2011) performed P-wave teleseismic tomography for upper mantle structure beneath Anatolia. They observed segmented fast seismic anomalies beneath Anatolia that was interpreted as the subducted portion of the African lithosphere along the Cyprus and the Hellenic trenches. They identified a gap as wide as 300 km between subducted Aegean and the Cyprus slabs beneath Anatolia. Figure 2.6 shows the results of Biryol et al. (2011). Major slow perturbations are explained with hot upwelling

asthenosphere. They also defined the eastern termination of the subducting African lithosphere.

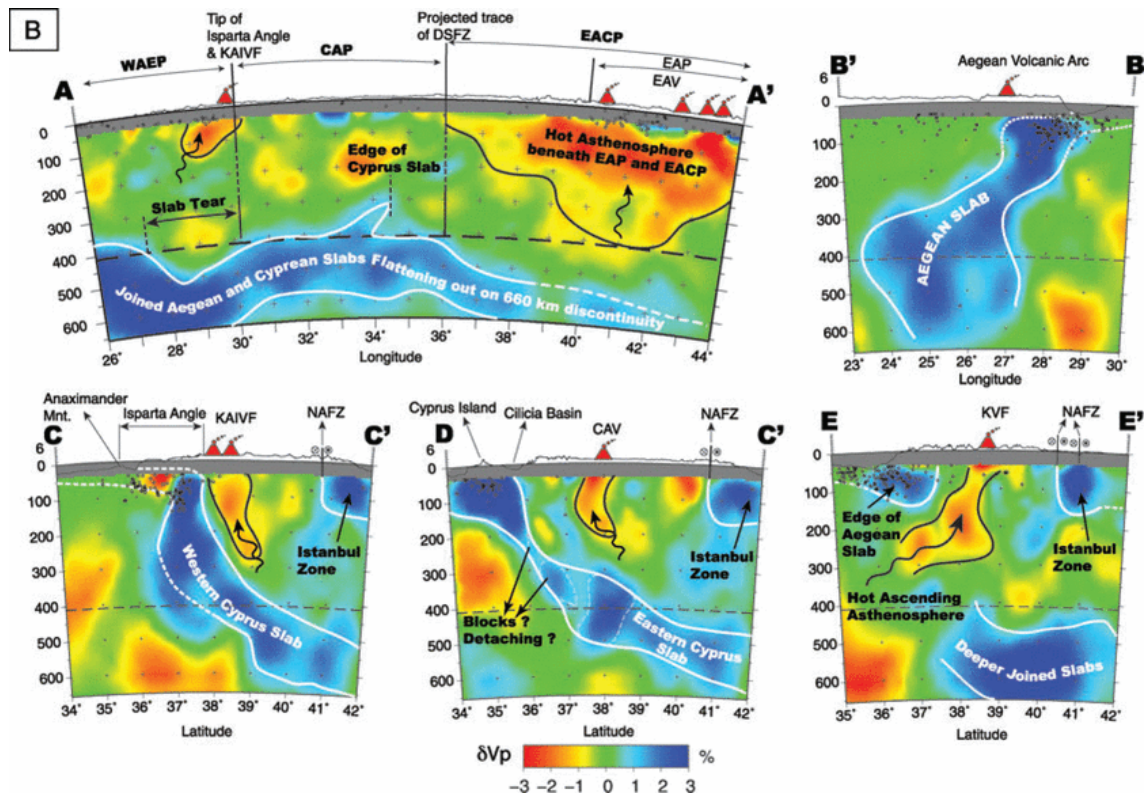


Figure 2.6. Interpretation of the five section across the study area. AA': 39°N; B'B': 40°N23°E-35°N30°E; CC': 34°N30°E-42°N32°E; DC': 34°N33°E-42°N32°E; EE': 28.5°E (See Biryol et al. (2011) for detailed location of the slices and explanations).

Most recent tomography study is performed to obtain an improved seismic velocity model of the Eastern Mediterranean mantle by Portner et al. 2018 (Figure 2.7). Their model confirmed that the Aegean slab extends to the lower mantle; and existence of slow velocity anomalies beneath Anatolia; and fast velocity anomalies located at the north of the Izmir-Ankara-Erzincan suture zone in the shallow mantle.

They reported that the slabs in the Eastern Mediterranean reach to the 660 km discontinuity; Aegean slab is relatively continuous while but Cyprus slab is highly segmented (tears and slab breaks) (Figure 2.8). They point out two main tears 1) between Aegean and Cyprus slabs 2) fragmentation on Cyprus slab in the east.

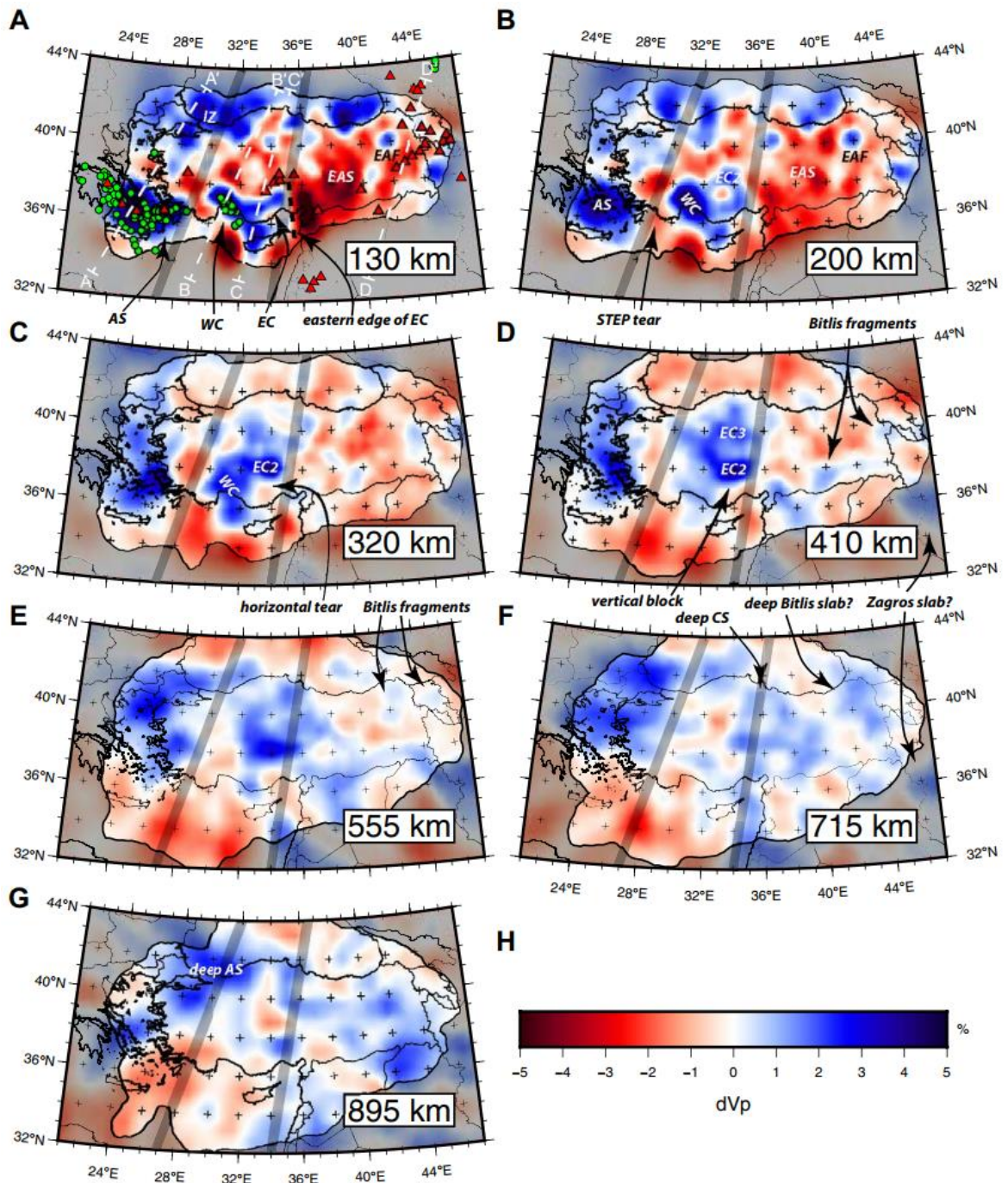


Figure 2.7. The results of the teleseismic tomographic by Portner et al. 2018. Shading area restricted by a solid black line show the 0.5 hit quality contour. Green circles are earthquake locations. Red triangles indicate volcanoes. See Portner et al. 2018 for the abbreviations and other details.

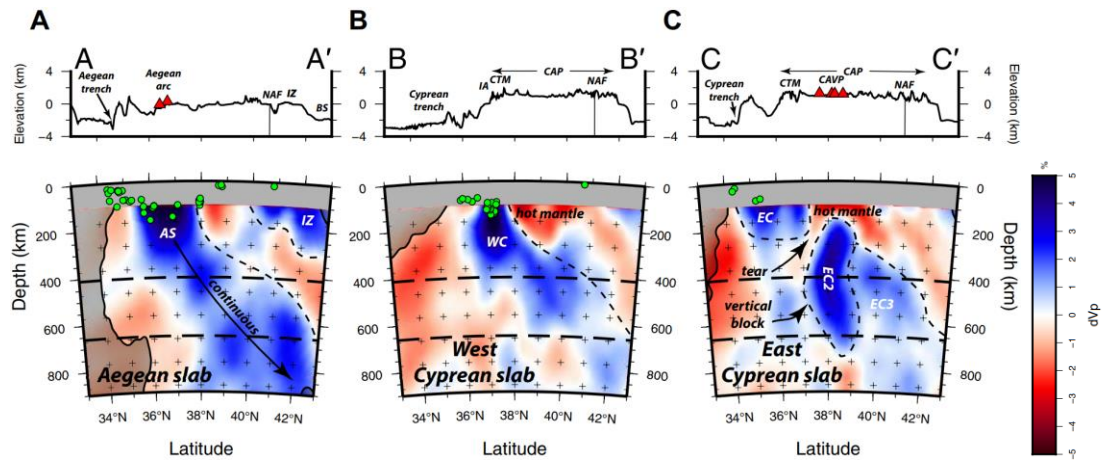


Figure 2.8. Cross sections through the tomography model by Portner et al. 2018. Locations of the slices are shown at Figure 2.7A with white dashed lines. Topography and tectonic features are labeled above the profiles. See Portner et al. 2018 for the abbreviations and other details.

### 2.3 Seismicity

The Aegean Sea, the surrounding Greek coasts and the western Turkey, along with the Hellenic Arc, are the most active seismic areas of the Mediterranean Basin and of the whole Alpine-Himalayan chain. The catalogues of seismicity are incomplete for low magnitude events ( $M < 2.5$ ), but the map permits to identify the active seismogenic zones at broad scales. Several earthquakes with magnitudes greater than 7 occurred during the instrumental period. The seismicity distribution shown in Figure 2.9 and the trend of the focal mechanisms in Figure 2.10 are related to the major tectonic features. Most earthquakes are confined in the upper crust. The seismicity clusters along the NAF, East Anatolian Fault (EAF) and east-west trending grabens in WA. The Cyprus arc has lower seismicity rate than the Hellenic arc. This is consistent with the convergence rate across the Hellenic Arc ( $\sim 33$  mm/yr.) being about two to three times faster than across the Cyprus Arc (McClusky et al. 2003; Wdowinski et al. 2006).

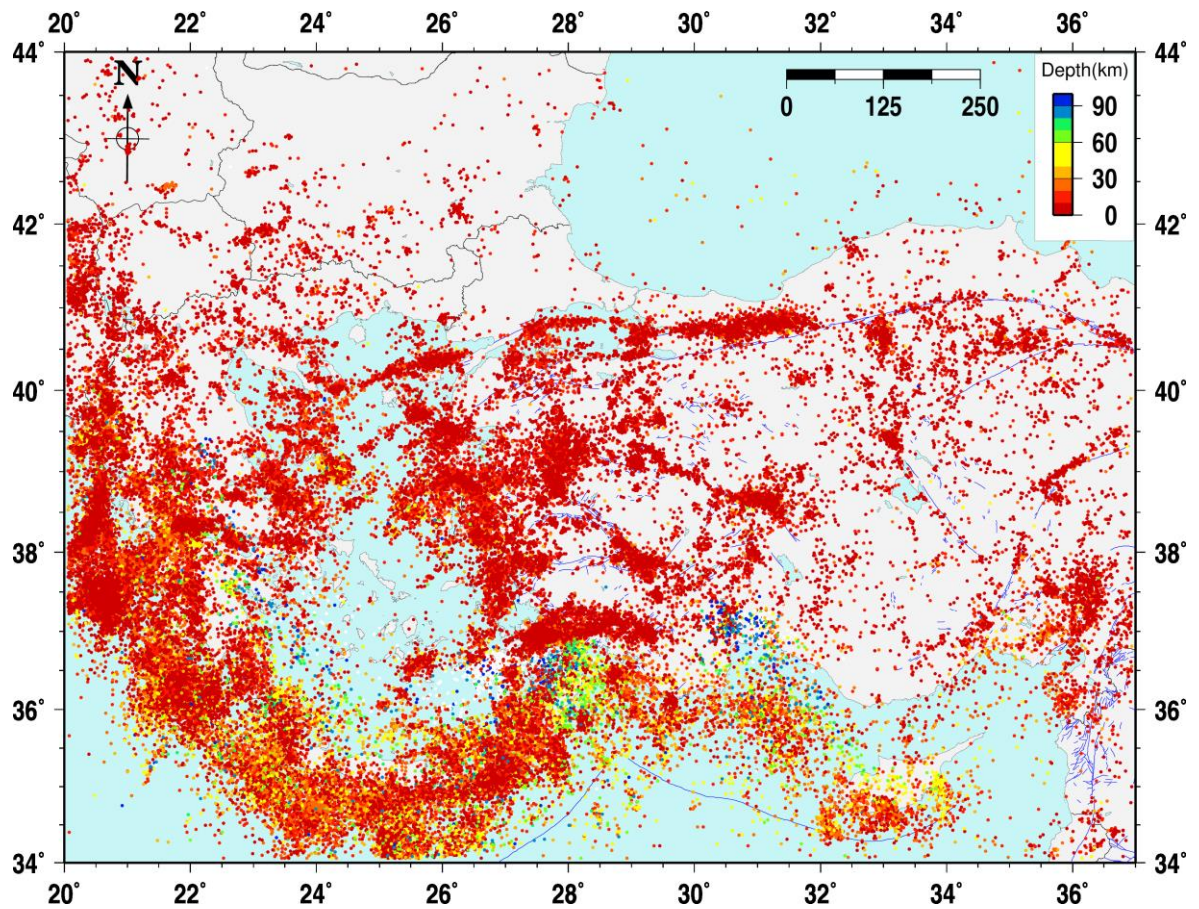


Figure 2.9. Seismicity of the eastern Mediterranean region for the period of 1999-2019 with magnitudes greater than or equal to 2.5 (EMSC Catalog).

The moment tensor solutions of earthquakes with magnitudes greater than 5.0 between 1955 and 2000 in the region are shown in Figure 2.10 modified from Jolivet et al., 2013. Strike slip mechanisms are not only observed along NAF but also on EAF, North Aegean Trough and south of North Aegean Trough (Jackson, 1994; Roumelioti et al., 2011) until NCDS in Aegean. Mostly normal faulting is observed on WA, Eastern and Northern Greece and Northern part of the Hellenic Trench. Reverse faulting is observed along Hellenic and Cyprus Trench and Western Greece with the crustal thickening due to HP-LT conditions (Jolivet et al., 2013), however in the back arc region mostly normal faulting is observed because of the crustal thinning due to accretionary processes (Jolivet et al., 2013). Deep earthquakes are mostly seen throughout the trench except within the subduction tears on the Hellenic and Cyprus trenches.

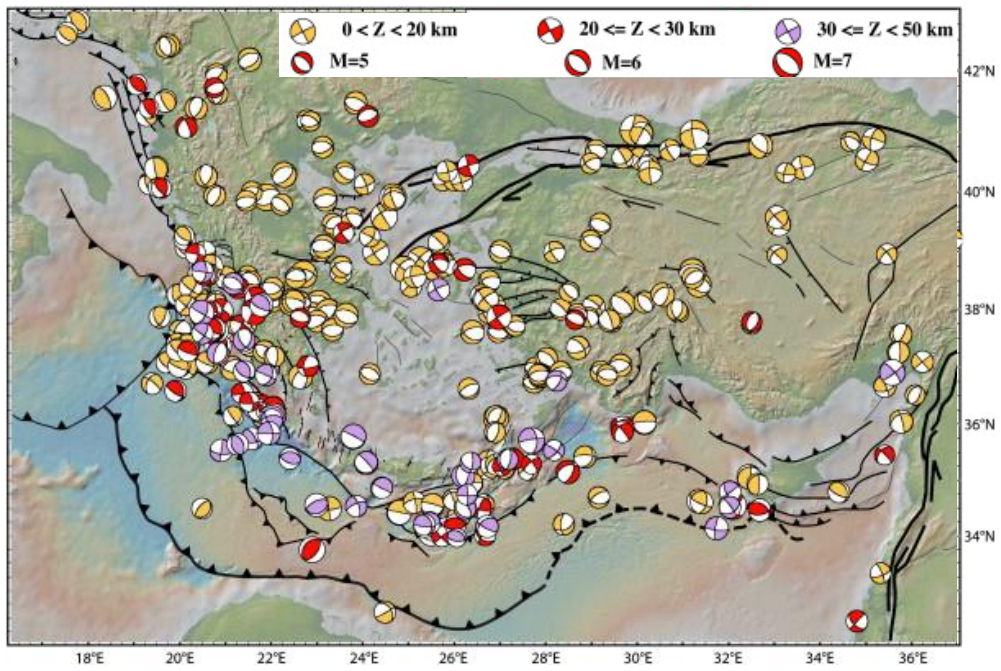


Figure 2.10. Focal mechanisms of earthquakes over the Aegean Anatolian region  
(Modified from Jolivet et al., 2013).

### 3. METHODOLOGY

We employed a teleseismic body wave tomography method to obtain 3D structure of the upper mantle. We used teleseismic earthquakes between distances  $30^\circ$  and  $98^\circ$  from the receivers. Many approaches exist to determine velocity perturbations beneath a receiver array. In this part, we describe the method used in this study.

#### 3.1 Model Parameterization

Tomography characterizes a linearized approximation of a formerly non-linear problem. The results of inversion are sensitive to the initial model, thus we assume in the linearization that the initial model is a close approximation to the true Earth model. The proper parameterization of the velocity model has also a large influence on the solution quality (Kissling et al., 2001). Model and inversion grid structures should be formed according to the station distribution (ray-paths). Additionally, grid spacing has to be appropriate to exemplify the heterogeneities of the model area. There are two options to create model, common regular and irregular parameterization.

Many researchers prefer regular parameterization because it is simple, easy formulate and generally do not complicate the forward and inverse solvers (Rawlinson et al., 2010). Figure 3.1a show one of most common parameterizations, cells or blocks have uniform seismic properties (velocity or slowness). This parameterization was used in many tomography studies such as teleseismic (Aki et al., 1977 and Saltzer and Humphreys, 1997), local earthquake (Aki and Lee, 1976 and Nakanishi, 1985), global (Grand et al., 1997 and Boschi and Dziewonski, 1999) and wide-angle (Zhu and Ebel, 1994 and Blundell, 1993).

An alternative parameterization scheme is to define seismic properties at the vertices of regular grid (Figure 3.1b). However, in this method, an interpolation function must be used. This parameterization can be constructed trilinear or cubic splines interpolant. Trilinear interpolation between rectangular grids was tested first Thurber, 1983. Then many researchers applied this method for earthquake tomography (Graeber and Asch, 1999) and teleseismic tomography (Steck et al., 1998). Cubic spline functions are used in many studies

such as wide-angle and teleseismic tomography (Farra and Madariaga (1988), Rawlinson et al. (2006b)).

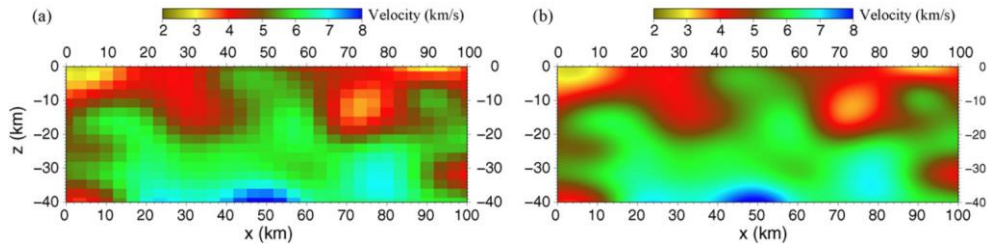


Figure 3.1. 2D velocity field defined using (a) constant velocity blocks; (b) cubic B-spline patches (Rawlinson et al., 2010).

After defining velocity parameterization, we need to construct interface parameterization. Two types of interface parameterization are used in tomography. First and the common one (Figure 3.2a) includes sub-horizontal layers overlying half-space (Rawlinson and Sambridge, 2003). If extra information on the interior of the model is known, more complicated interface parameterization (Figure 3.2b) can be constructed (e.g. Pereyra, 1996 and Bulant, 1999). With this method, any kind of geological structure can be modeled.

Station and event locations are geographically irregular except for the controlled source studies. Parameterization can be constructed irregularly (instead of uniform) to resolve irregular sampling in study volume. Chou and Booker (1979) is the first study on this type of parameterization.

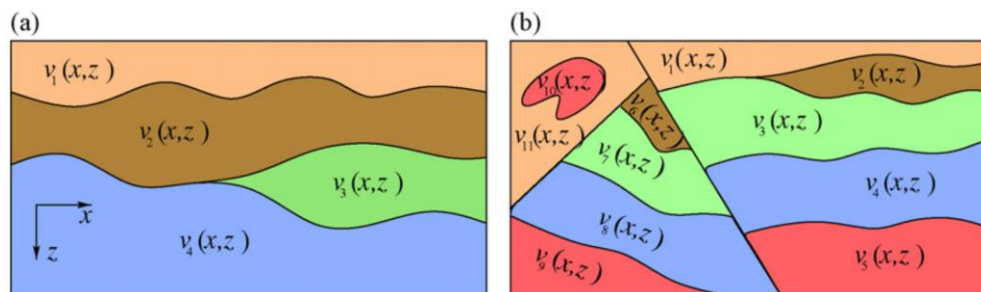


Figure 3.2. Two different models; continuous and discontinuous changes in seismic property (a) interfaces of the layers continuous horizontally and seismic structure  $w_i(x, z)$

changes smoothly; (b) interfaces of the layers set up irregularly and seismic structure  $w_i(x, z)$  changes smoothly (Rawlinson and Sambridge, 2003).

### 3.2 Forward Calculation

Earth can be described as sphere, which consists of layers, which have different properties such as velocity, density, temperature etc. These layers form specific discontinuities such as crust, mantle, and core. One of the practical problems in seismic tomography is to compute accurate and robust travel times.

Traveltime between source and receiver is given by an integral:

$$t = \int_S^R \mathbf{s} dl = \int_S^R \frac{1}{v(\vec{x})} dl \quad (3.1)$$

where  $\mathbf{s}$  is slowness,  $\vec{x}$  is the position vector,  $v$  is velocity,  $dl$  is the differential path length,  $S$  is source and  $R$  is receiver. Many techniques are developed to find the most accurate travel times (optimum ray trace) between two points, source and receiver. The descriptions of these methods are explained under two categories, ray-based methods (Shooting and Bending) and grid-based methods (Finite difference schemes and Fast Marching Algorithms).

#### 3.2.1 Ray-based Methods

Ray-tracing is a two-point boundary value problem. Each end points are known; the path and travel time information are unknown. In shooting method, this boundary value problem is solved iteratively with an initial value. One end-point (source point) selected as fixed point, and different paths are calculated with the initial ray direction to find correct end-point (receiver point) (Figure 3.3a). At each interface, Snell's law is applied and incident angle is calculated. Aim of all traveltime methods is the same: to get minimum travel time value between source and receiver.

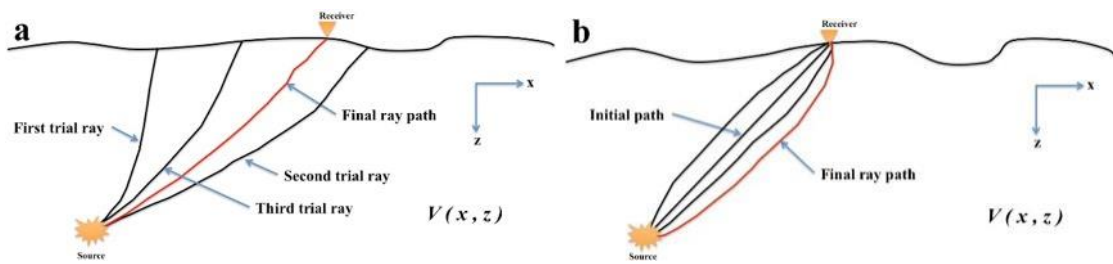


Figure 3.3. Representation of the two basic approaches to ray-tracing: (a) shooting and (b) bending. For shooting, trajectory of the initial ray at the source is perturbed until the receiver is reached. For bending, an initial path (not a ray-path) connecting the source and receiver is perturbed until a ray-path is reached (redrawn from Thurber, 1993).

In bending method, both end points are fixed and path is perturbed (Figure 3.3b). After a number of iterations, true ray path is selected according to Fermat's principles. This method was developed by Wesson (1971), Julian and Gubbins (1977) and Pereya et al. (1980). Julian and Gubbins (1977) used this method to solve a system of first order differential equations.

### 3.2.2 Grid-based Methods

Shooting and bending methods use ray-tracing algorithms to determine real path between source and receivers. However, some methods use wave front tracking procedures, which have some advantages (Rawlinson et al., 2010):

- Travel time values are calculated at all the points in study volume
- Methods are very stable in heterogeneous media
- If the sources are enough, methods can compute travel time and path efficiently

First use of finite difference schemes for solutions of Eikonal equation on the grid is proposed by Vidale (1988) and Vidale (1990). In finite difference schemes, traveltime gradient  $\nabla T$  is calculated for entire model on each grid. Therefore, after processing we need to determine ray path by following traveltime gradient. After Vidale (1988), many researchers worked with this method and add some improvements such as; improve stability and correcting for the non-causal nature of the expanding square (Rawlinson and Sambridge, 2003).

FMM, which is one of the Eikonal solvers, is developed by Sethian (1996a) and Sethian (1996b) and is presented in 3D version by Sethian and Popovici (1999). They applied this method to a geophysical problem first. At all the grid point in 2D or 3D spherical grid Eikonal equations are solved. If grid size and the order of the finite difference scheme are suitable for the study area, the accuracy of the result is satisfactory. Here a summary of the formulation of FMM from Rawlinson and Sambridge (2003) is presented.

FMM uses the first order upwind difference scheme:

$$\left[ \max(D_{ijk}^{-x}T, -D_{ijk}^{+x}T, 0)^2 + \max(D_{ijk}^{-y}T, -D_{ijk}^{+y}T, 0)^2 + \max(D_{ijk}^{-z}T, -D_{ijk}^{+z}T, 0)^2 \right]^{\frac{1}{2}} = S_{ijk} \quad (3.2)$$

where;

$$D^{+x}T = \frac{T(x + \delta x) - T(x)}{\delta x} \quad (3.3)$$

$$D^{-x}T = \frac{T(x) - T(x - \delta x)}{\delta x} \quad (3.4)$$

and  $S_{ijk}$  is slowness for  $(i, j, k)$  point. Because eq. 3.2 is quadratic equation, there are two solutions (roots). The larger solution is always true (Rawlinson and Sambridge, 2003). Sethian and Popovici (1999) use narrow band method (Figure 3.4) to compute traveltime values. Narrow band zone actually represents a propagating wave front. The movement of the wave front is from upwind to downwind direction. Traveltime values are already calculated correctly on alive points in the grid. Close points are being calculated and far points are untouched.

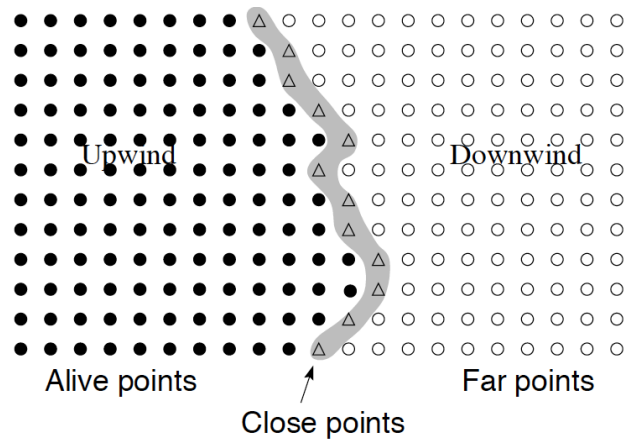


Figure 3.4. Principle of the narrow band method. See text for detail (Rawlinson and Sambridge, 2003).

Black dot in Figure 3.5a indicates source. Calculation of traveltimes starts from source to four neighbors by using eq. 3.2. The value of smallest traveltime of neighboring (grey) point is calculated again by using white circles around (Figure 3.5b). Now we have 2 black (alive) points. Then smallest traveltime of six grey points must be correct. This procedure goes like this (Figure 3.5c). The zone include grey points is named narrow band.

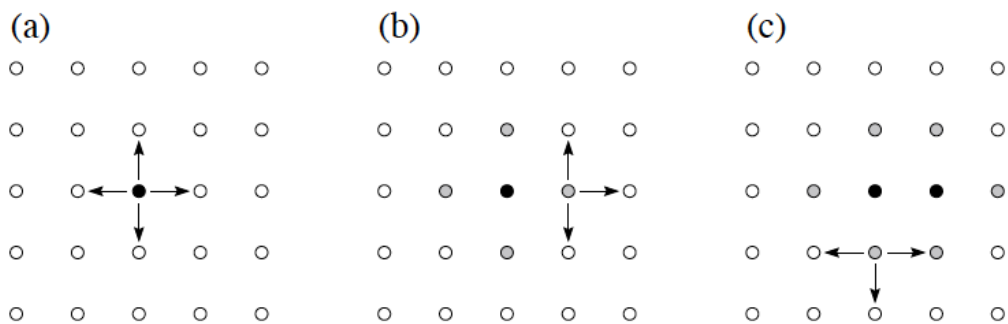


Figure 3.5. Principal of the FMM in 2-D. See text for detail (Rawlinson and Sambridge, 2003).

### 3.3 Inversion

In the previous chapter, the methods for computing accurate and robust travel times are discussed. Inversion techniques allow us to reconstruct a model from our observations.

Model consists of set of parameters. The input data is the observed travel times and the model parameters are velocity or slowness.

In this chapter, we mention inversion into three groups back projection, gradient methods and global optimization techniques.

### 3.3.1 Backprojection

The objective is to project the data, which is recorded at the station, along the ray path from receiver to source. At the end, we obtain model parameters belong to medium which ray passes along with this relationship:

$$d = g(m) \quad (3.5)$$

where  $d$  observations,  $m$  model parameters. In backprojection methods, model is designed with constant slowness (velocity) blocks. Therefore, Eq (3.5) can be linearized as:

$$d = Gm \quad (3.6)$$

by using the connection between slowness perturbations  $m$  and traveltime perturbations  $d$  (Rawlinson et al., 2010).  $G$  is the (Coefficient Matrix) ray length. Because each ray passes limited number of block,  $G$  has many zero elements. There are two common backprojection techniques to solve Eq (3.6), Algebraic Reconstruction Technique (ART) and Simultaneous Iterative Reconstruction Techniques (SIRT).

ART was used first in geophysical area by McMechan, 1983. In ART, the model is divided into  $m$  cells (row x column) and each cell is assigned an initial approximation of  $\delta s_j$  for each seismic ray and then computes all ray segments and residuals. After each calculation, model parameters are updated individually until residual condition is satisfied. Blundell (1993) reported that ART suffers from poor convergence properties. Conversely, SIRT takes average of all perturbations that pass in a cell. This technique can be used to overcome convergence problem of ART (Rawlinson et al., 2010).

### 3.3.2 Gradient Methods

We can define inverse problems as minimization of an objective function (OF) Eq (3.7). This OF may consist of a data residual term and regularization terms. (Rawlinson and Sambridge (2003))

$$S(\mathbf{m}) = \frac{1}{2} [\Psi(\mathbf{m}) + \epsilon\Phi(\mathbf{m}) + \eta\Omega(\mathbf{m})] \quad (3.7)$$

First part of Eq (3.7) is  $\Psi(\mathbf{m})$  the difference between the observed and predicted data. All the model parameters are not well constrained by the data alone. To decrease the non-uniqueness of the solution we need to include  $\Phi(\mathbf{m})$  regularization term to the OF. Regularization term provides to add additional constraints to the objective function. Constable et al., 1987 defined alternative method to regularization is the minimum structure solution. This approach tries to find an acceptable trade-off between satisfying the data and finding a model with the minimum amount of structural variation. Sambridge (1990) characterized a method of including this prerequisite in the OF,  $\Omega(\mathbf{m})$ .  $\epsilon$  indicates damping factor and  $\eta$  smoothing factor.  $\epsilon$  and  $\eta$  controls the trade-off between the how well the solution  $m_{\text{est}}$  satisfy the data, how closely  $m_{\text{est}}$  is to  $m_0$  and the smoothness of  $m_{\text{est}}$ . Rawlinson and Sambridge (2003) inspected the trade-off curves between model perturbation (or roughness) and data fit for the values of  $\epsilon$  (or  $\eta$ ) (Figure 3.6). Another method to find an appropriate value for damping and smoothing is to apply checkerboard tests.

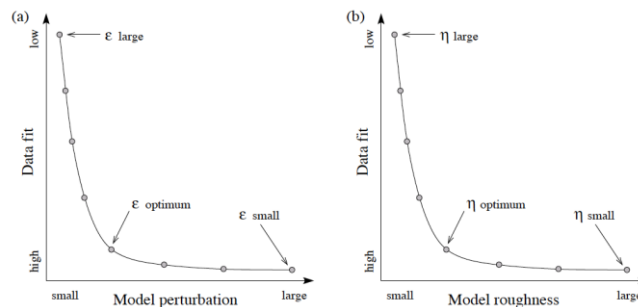


Figure 3.6. Trade-off curves to choose appropriate damping or smoothing parameters for an inversion. (a) Model perturbation for values of  $\epsilon$  and data fit. (b) Model roughness for values of  $\eta$  and data fit (Rawlinson and Sambridge, 2003).

All the gradient methods use derivatives of  $S(\mathbf{m})$  at a specified point in model space and shared an assumption that  $S(\mathbf{m})$  is adequately smooth to allow a local quadratic approximation about some current model:

$$S(\mathbf{m} + \delta\mathbf{m}) \approx S(\mathbf{m}) + \hat{\boldsymbol{\gamma}}\delta\mathbf{m} + \frac{1}{2}\delta\mathbf{m}^T\hat{\mathbf{H}}\delta\mathbf{m} \quad (3.8)$$

where  $\delta\mathbf{m}$  is a perturbation to the current model and  $\hat{\boldsymbol{\gamma}} = \partial S / \partial \mathbf{m}$  and  $\hat{\mathbf{H}} = \partial^2 S / \partial \mathbf{m}^2$  are the gradient vector and Hessian matrix respectively. If we evaluate partial derivatives for Eq (3.7):

$$\hat{\boldsymbol{\gamma}} = \mathbf{G}^T \mathbf{C}_d^{-1} [\mathbf{g}(\mathbf{m}) - \mathbf{d}_{obs}] + \epsilon \mathbf{C}_m^{-1} (\mathbf{m} - \mathbf{m}_0) + \eta \mathbf{D}^T \mathbf{D} \mathbf{m} \quad (3.9)$$

$$\hat{\mathbf{H}} = \mathbf{G}^T \mathbf{C}_d^{-1} \mathbf{G} + \nabla_m \mathbf{G}^T \mathbf{C}_d^{-1} [\mathbf{g}(\mathbf{m}) - \mathbf{d}_{obs}] + \epsilon \mathbf{C}_m^{-1} + \eta \mathbf{D}^T \mathbf{D} \quad (3.10)$$

where  $\mathbf{G} = \partial \mathbf{g} / \partial \mathbf{m}$  is the Fréchet matrix (FM) of partial derivatives. Because  $\mathbf{g}$  is generally non-linear, iterative approach must be used for minimization of Eq (3.7):

$$\mathbf{m}_{n+1} = \mathbf{m}_n + \delta\mathbf{m}_n \quad (3.11)$$

where  $\mathbf{m}_0$  is the initial model. We try to determine  $\delta\mathbf{m}$  by using gradient-based inversion methods.

First method is the classical one, Gauss-Newton (G-N) method. This method calculates model updates by finding minimum of tangent paraboloid to  $S(\mathbf{m})$  at  $\mathbf{m}_n$ , which produces,

$$\delta\mathbf{m}_n = -[\mathbf{G}_n^T \mathbf{C}_d^{-1} \mathbf{G}_n + \nabla_m \mathbf{G}_n^T \mathbf{C}_d^{-1} (\mathbf{g}(\mathbf{m}_n) - \mathbf{d}_{obs}) + \epsilon \mathbf{C}_m^{-1} + \eta \mathbf{D}^T \mathbf{D}]^{-1} x[\mathbf{G}_n^T \mathbf{C}_d^{-1} (\mathbf{g}(\mathbf{m}_n) - \mathbf{d}_{obs}) + \epsilon \mathbf{C}_m^{-1} (\mathbf{m}_n - \mathbf{m}_0) + \eta \mathbf{D}^T \mathbf{D} \mathbf{m}_n] \quad (3.12)$$

It is hard to calculate derivative of G. Therefore, it can be ignored and remainder will be the quasi-Newton (q-N) solution,

$$\begin{aligned} \delta \mathbf{m}_n = & -[\mathbf{G}_n^T \mathbf{C}_d^{-1} \mathbf{G}_n + \epsilon \mathbf{C}_m^{-1} + \eta \mathbf{D}^T \mathbf{D}]^{-1} [\mathbf{G}_n^T \mathbf{C}_d^{-1} (g(\mathbf{m}_n) - \mathbf{d}_{obs}) \\ & + \epsilon \mathbf{C}_m^{-1} (\mathbf{m}_n - \mathbf{m}_0) + \eta \mathbf{D}^T \mathbf{D} \mathbf{m}_n] \end{aligned} \quad (3.13)$$

For G-N and q-N methods, It must be solved a system consists of M linear equations, because there are M unknowns. If  $\mathbf{d} = g(\mathbf{m})$  is linearizable Eq (3.6) turns into:

$$\mathbf{d}_{obs} \approx g(\mathbf{m}_0) + G(\mathbf{m} - \mathbf{m}_0) \quad (3.14)$$

Newton and q-N are the same if Eq (3.14) is exactly linear.  $\delta \mathbf{m}_n$  in Eq (3.13) is called Damped Least Squares (when  $\eta = 0$ ) and this method is used to solve the inverse problems (e.g. Aki et al., 1977; Rawlinson et al., 2006b).

The second (1D) method is the steepest descent (SD) method. The aim of this method is to minimize OF with iteration. The OF could be minimized along local directions of SD if our search is corrected. This method is very simple but has poor convergence properties (Rawlinson and Sambridge (2003)).

Third method is the conjugate gradient (CG) method. CG method also performs a 1D minimization process along search direction same as SD method. However, in CG method, at each iteration, new search direction that is conjugate to all previous ones is used. After  $n^{\text{th}}$  iteration, we have n direction and n dimensional subspace. Tarantola (1987) defined CG:

$$\boldsymbol{\phi}_n = \boldsymbol{\gamma}_n + \alpha_n \boldsymbol{\phi}_{n-1} \quad (3.15)$$

$$\delta \mathbf{m}_n = -\mu_n \boldsymbol{\phi}_n \quad (3.16)$$

where  $\boldsymbol{\phi}_n$  is a set of conjugate directions and  $\boldsymbol{\phi}_0 = \boldsymbol{\gamma}_0$ .

Both SD and CG methods are the form of subspace methods and work along a line. Nevertheless, subspace inversion method (SiM) can be performed in which the minimization is applied simultaneously on a few search directions (Sambridge, 1990; Rawlinson et al., 2006b). SiM projects the full-linearized inverse problem onto a much smaller n-dimensional model space (Rawlinson, 2008). Therefore, the size of the subspace dimension is also an

important parameter for inversion. If we assume the subspace dimension as 1 then the solution is equivalent to that obtained by the steepest descent method (Section 3.3.2). Increasing  $n$  also means that the calculation time will increase. Because at model subspace, the set of vectors, which span the  $n$ -dimensional subspace are computed based on the gradient vector and Hessian matrix. According to our tests, it is not necessary to set greater 10 for  $n$ .

In SiM we limit the minimization of quadratic approximation of  $S(\mathbf{m})$  to our model space. Because of this, we get a perturbation  $\delta\mathbf{m}$  in our space which spanned by a set of  $p$   $M$ -dimensional basis vector:

$$\delta\mathbf{m} = \sum_{j=1}^p \mu_j \mathbf{a}^j = \mathbf{A}\boldsymbol{\mu} \quad (3.17)$$

where  $\mathbf{A} = [\mathbf{a}^j]$  is the  $M \times p$  projection matrix. If we substitute eq. 3.17 into eq. 3.8, then we get  $\boldsymbol{\mu}$ :

$$\boldsymbol{\mu} = -[\mathbf{A}^T \hat{\mathbf{H}} \mathbf{A}]^{-1} \mathbf{A}^T \hat{\boldsymbol{\gamma}} \quad (3.18)$$

No we can substitute eq. 3.18 into eq. 3.17 and perturbation is given by:

$$\delta\mathbf{m} = -\mathbf{A}[\mathbf{A}^T (\mathbf{G}^T \mathbf{C}_d^{-1} \mathbf{G} + \epsilon \mathbf{C}_m^{-1} + \eta \mathbf{D}^T \mathbf{D}) \mathbf{A}]^{-1} \mathbf{A}^T \hat{\boldsymbol{\gamma}} \quad (3.19)$$

where  $\hat{\boldsymbol{\gamma}}$  is the gradient vector. We are looking for the basis vectors span the  $M$ -dimensional subspace. We start from  $\mathbf{a}^1 = \boldsymbol{\gamma}$ , and use singular value decomposition (SVD) to avoid linear dependence between different search directions  $\mathbf{a}^j$ . SVD is used to identify an orthonormal basis (Press et al. 1992). Because if we have large dimension ( $p$ ), all the  $\mathbf{a}^j$  may not completely span to all  $p$ -dimension. SVD can easily identify unnecessary basis to remove. If  $\mathbf{A}$  is calculated and orthonormalized, the perturbation can be calculated easily by inverting small  $p \times p$  matrix. The SiM is more stable and efficient for large inverse problems (Rawlinson et al., 2006b).

For all methods described in this section, FM -  $\mathbf{G} = \partial \mathbf{g} / \partial \mathbf{m}$  must be calculated. FM describes the amount of change of traveltimes regarding model parameters (Rawlinson et al., 2010). FM is the special condition of derivatives of  $\mathbf{g}$ ; describes the derivatives of  $\mathbf{g}$  only for a continuous model (Shaw and Orcutt, 1985).

## 4. TELESEISMIC TRAVELTIME TOMOGRAPHY

### 4.1 Data

We selected 3-component recordings of broadband seismic stations in Turkey and surrounding regions (Figure 4.1). The database contains records from 417 stations of permanent and temporary arrays operated between 2004 and 2015. The stations were installed by various agencies and through different international projects. The temporary deployments provided at least one year of continuous data while data from permanent stations are available for longer durations (2-10 years). These networks are the following: KOERI (2004-2015), AFAD (2004-2015), NOA (2004-2015); NAF (2006-2008); SIMBAAD (2007-2009). (See Figure 4.1)

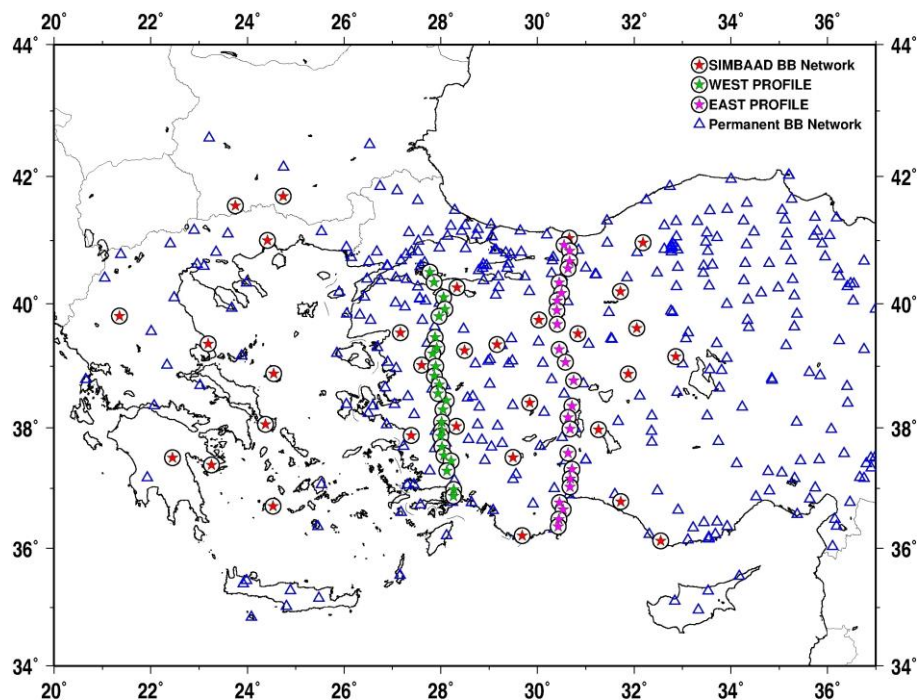


Figure 4.1. Station distribution used in this study. Blue triangles indicate Turkey, Greece and Cyprus permanent broadband stations, Red, Green and Pink stars indicate SIMBAAD broadband temporary stations. Green stars indicate west profile and pink stars indicate east profile.

#### 4.1.1 Event Distribution and Data Preparation

In this study, we used 798 teleseismic earthquakes with magnitudes greater than 5.5 and epicentral distances between  $30^\circ$  and  $98^\circ$  (Figure 4.2). Event locations were taken from the USGS event catalogue. The event distribution is nonuniform; majority is located between  $0^\circ$  and  $100^\circ$  azimuths.

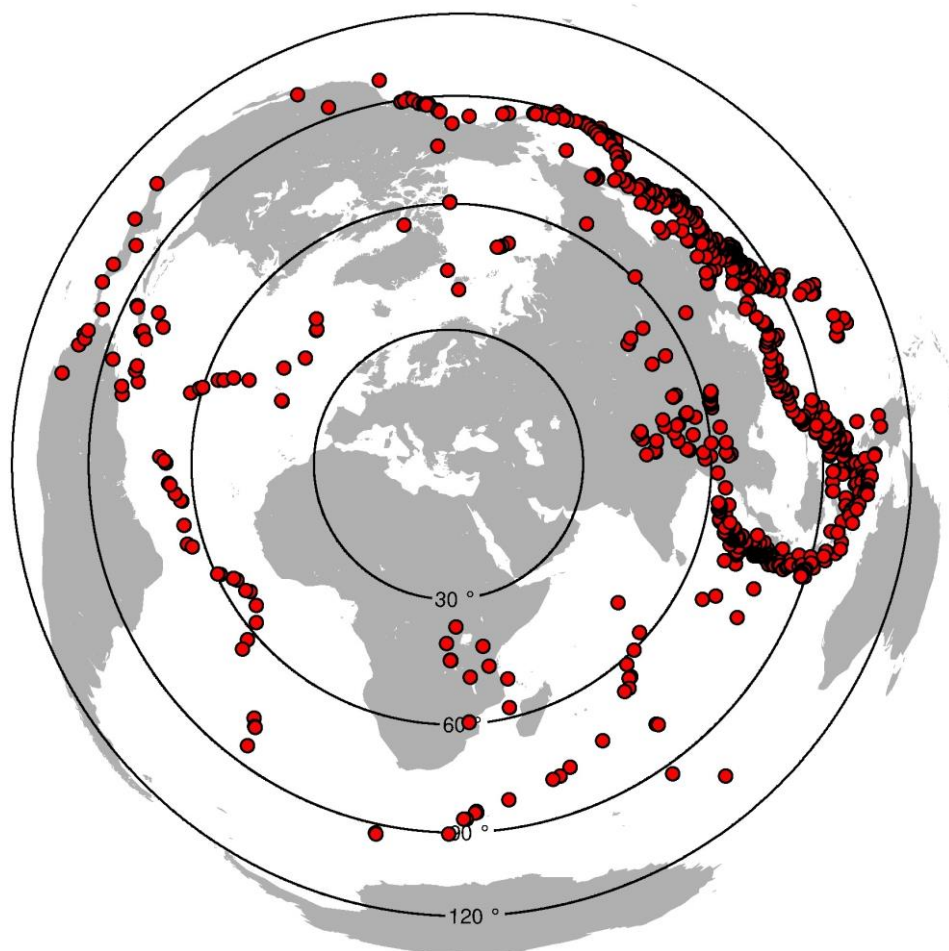


Figure 4.2. Distribution of the 798 teleseismic events (red circles) used in the tomographic inversion. Straight black circles indicate  $30^\circ$ ,  $60^\circ$ ,  $90^\circ$  and  $120^\circ$  the great circle distance from the study area.

In teleseismic tomography, the accuracy of arrival times is important. Because, tomographic methods are very sensitive to arrival time errors. The accuracy of picking errors

depends on the signal to noise ratio, which varies with the source location, magnitude and station quality.

Combining data from different sources presents a major problem during the preprocessing step. First, we merged the data from different sources. The data were converted to a uniform format, and waveforms with good signal to noise ratio were selected. Then all the waveforms were cut with a duration of 600 seconds and sampling intervals were fixed to 0.01 second. We removed trend and mean from the signals.

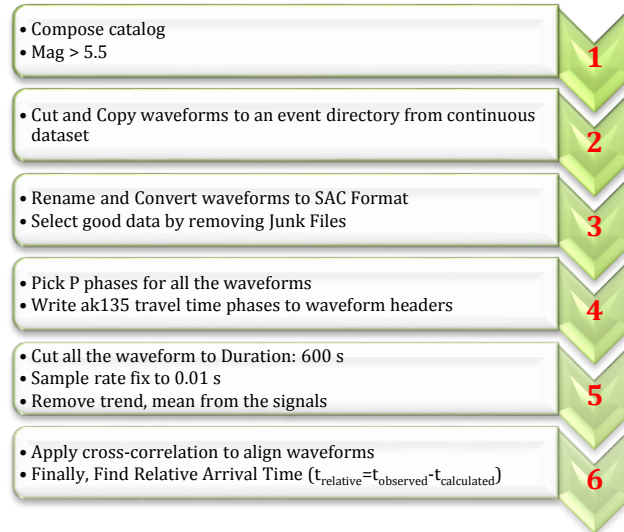


Figure 4.3 Data preparation steps.

We calculated the arrival times of direct P phases using the ak135 travel time model. Initially, the waveform, which has best signal/noise ratio, is chosen as reference station for cross-correlation. We then used correlation method to align waveforms. Then we picked all the waveforms relative to the reference trace. We manually checked to avoid any cycle skipping (Evans and Achauer, 1993).

Finally, the relative arrival time residuals for each waveform were calculated by subtracting computed arrival times from observed picks. Arrival (Travel) Time Residuals, which for source  $j$  and receiver  $i = 1, \dots, I_j$  are

$$r_{ij} = t_{Obs,ij} - t_{Calc,ij} \quad (4.1)$$

where  $t_{Obs,ij}$  is the observed travel time and  $t_{Calc,ij}$  is the travel time calculated for ak135 Earth model. Upper part of Figure 4.4 shows the waveforms alignments for 4 events before and after correlation in wiggle and image format. Lower part of Figure 4.4 shows the relative arrival time residual maps for the same events. Positive residuals suggest higher velocities; negative station terms suggest lower velocities with respect to ak135. The time residuals represent the integral of the travel time residuals from ak135 model from source to receivers. Positive time residuals are observed in the regions of Hellenic and Cyprus plates.

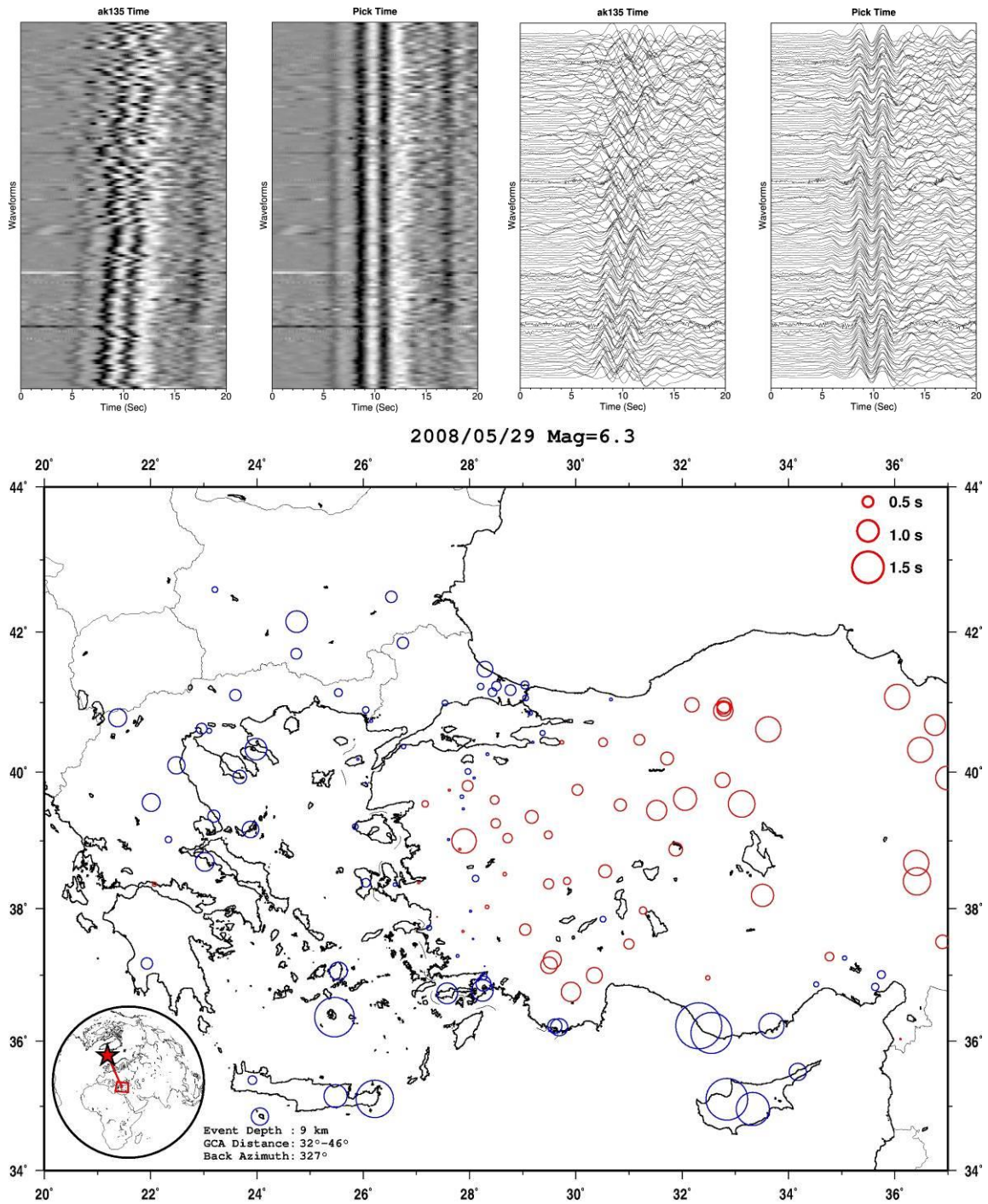


Figure 4.4. Examples using various events from different locations: The top figure shows the map of station residuals for each event. Residuals (in seconds) are calculated the relative to the picked arrival times after alignment. The title of each map shows the details of the event. Red circles indicate negative arrival time residuals and blue circles positive. Inset world map show the location of the study area and epicenter of the event. Event depth, nearest and far Great circle arc distances between event and stations, back-azimuth

of event to the center of the study area are also shown on the inset map. The legend of the size of the residuals can be found at the upper right corner of the map.

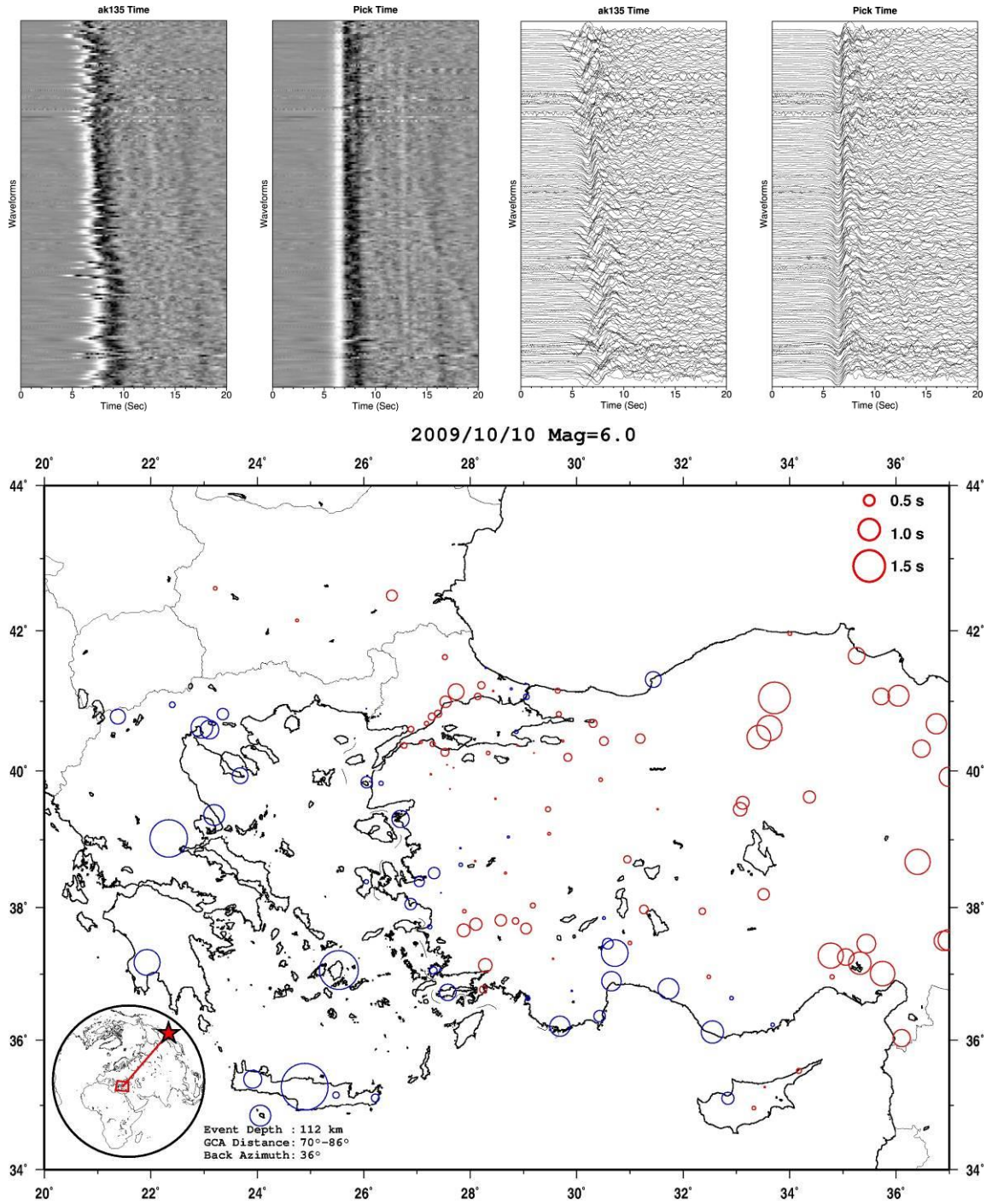


Figure 4.4. cont.

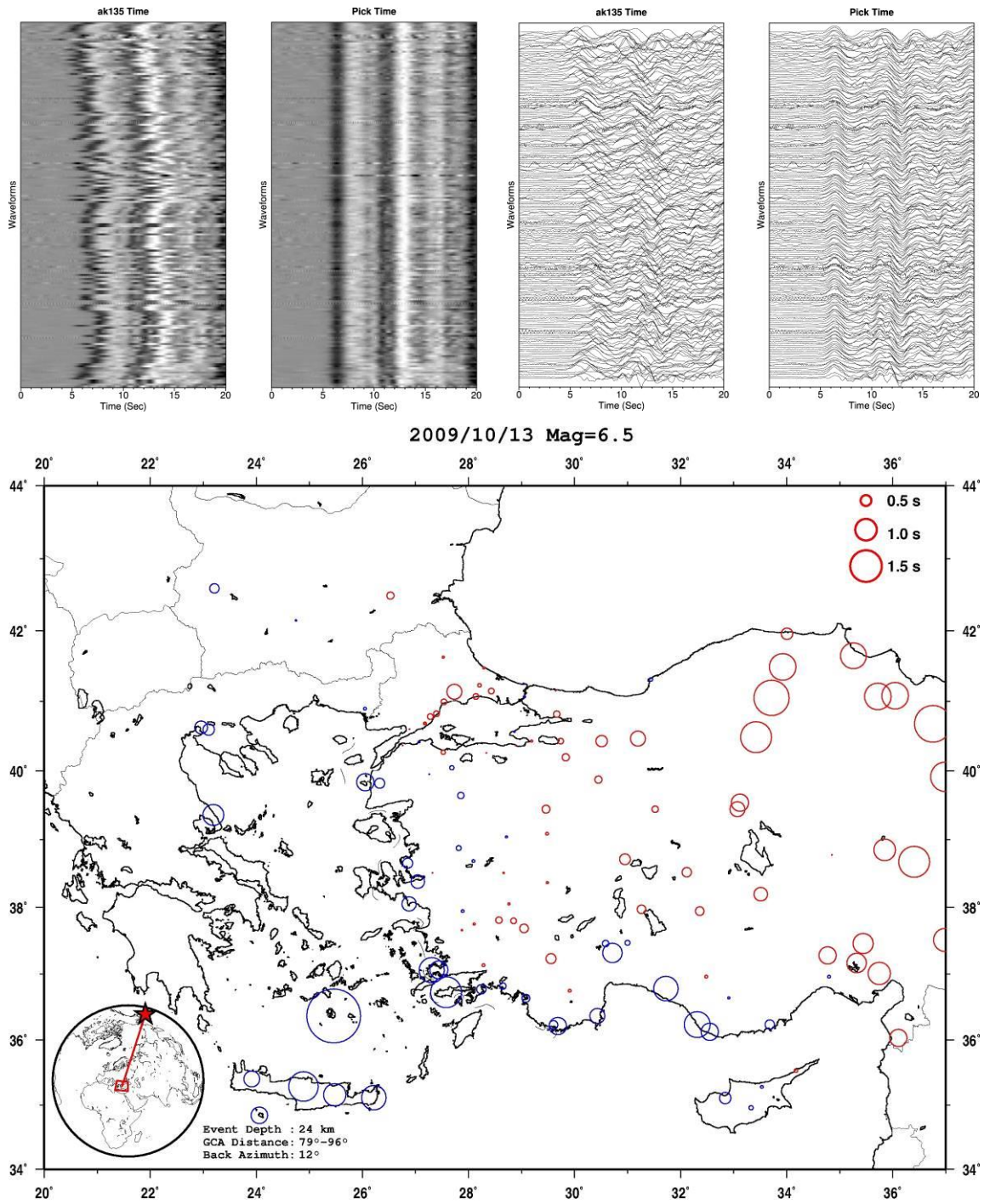


Figure 4.4. cont.

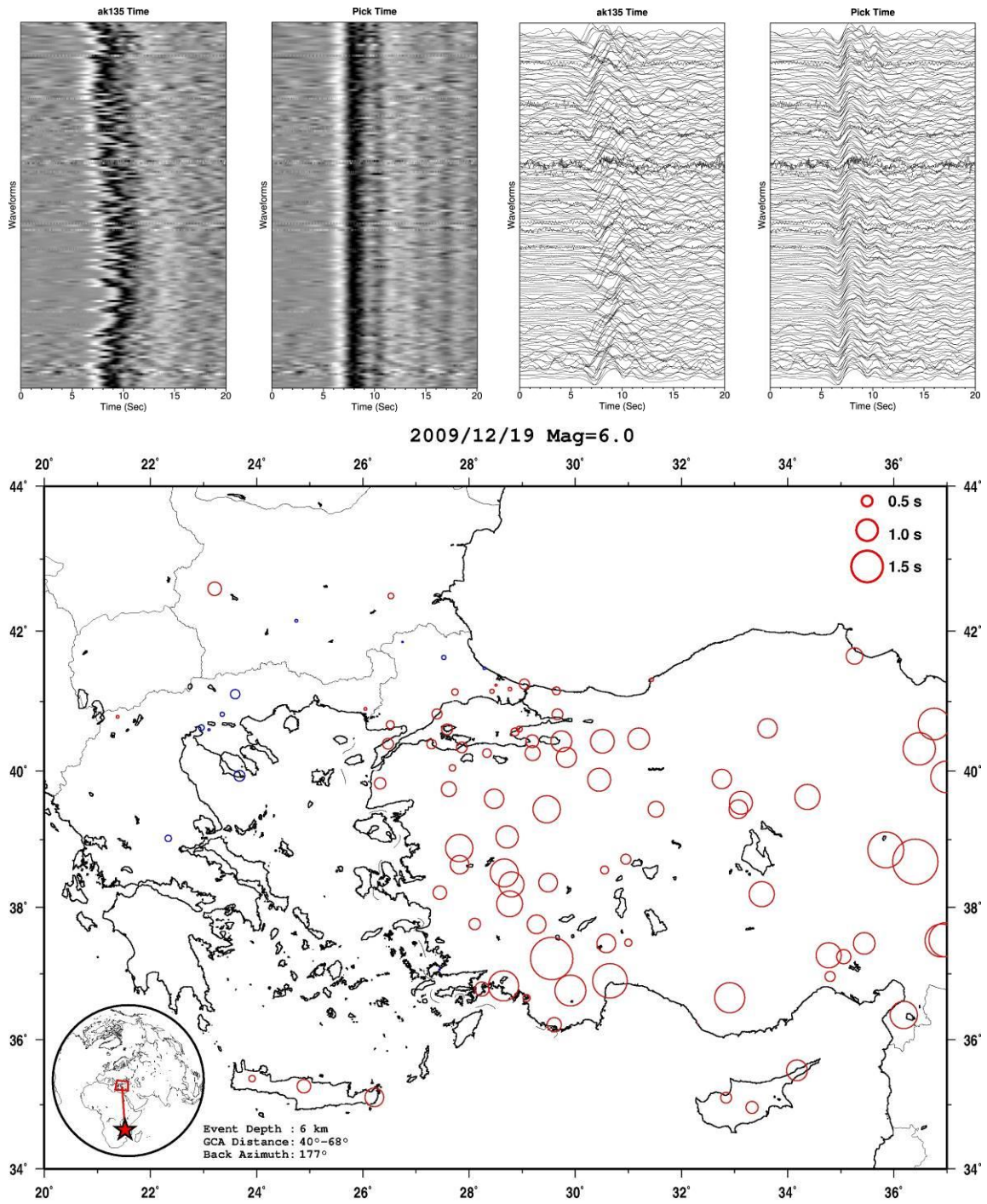


Figure 4.4. cont.

Finally, a total of 64,574 clear relative arrival time values are selected for further analysis.

#### 4.1.2 Statistics of the Catalog

In this section, we present statistics of the travel time residuals from the stations presented in Figure 4.1. Figure 4.5 shows the number of observations at each station. The distribution is not uniform as the operation times are different. The minimum number of observations is 35. In Figure 4.6 the RMS of travel time are presented. The large RMS values may be the result of velocity structure varying as a result of source azimuth. GPS timing errors of the stations also contributes to large RMS errors. We tried to eliminate the timing errors based on the large RMS values. The standard deviations shown in Figure 4.7 are relatively uniform throughout the region.

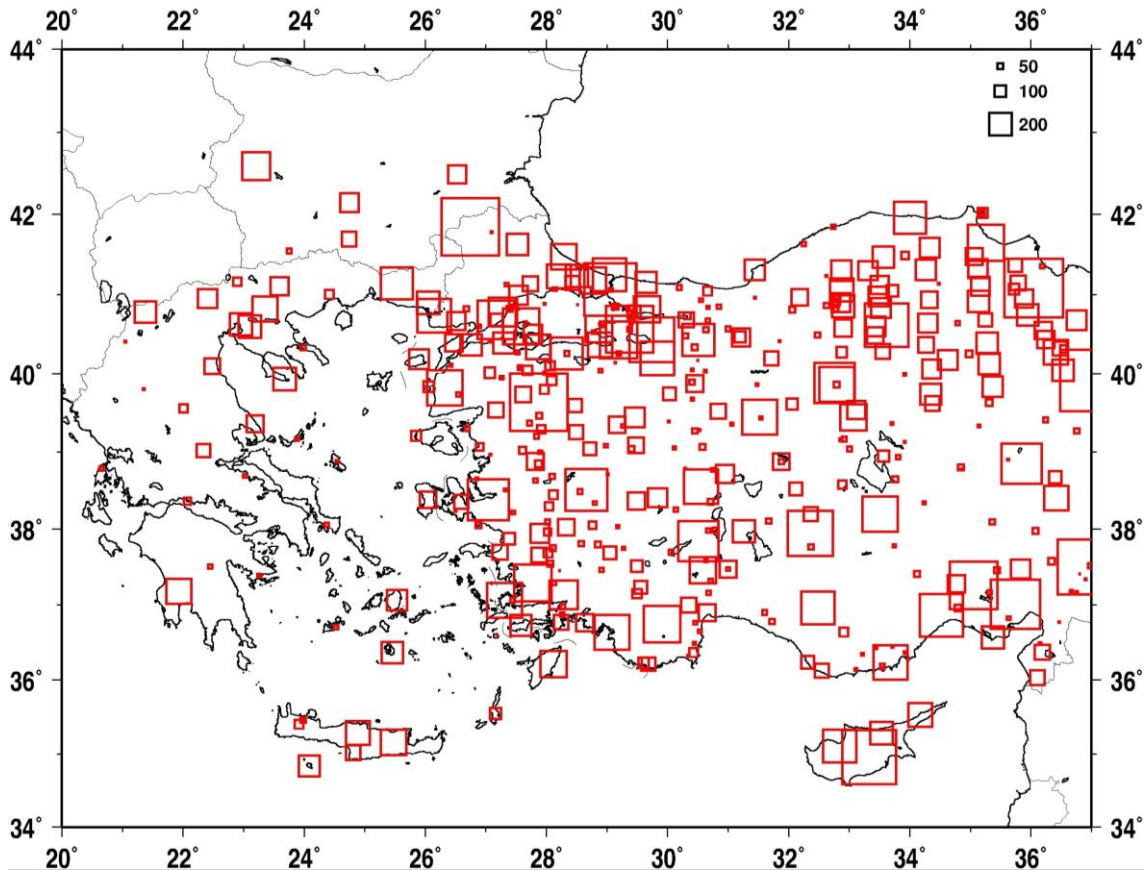


Figure 4.5. Number of observation of each station. The red squares show the magnitude of the number of observations.

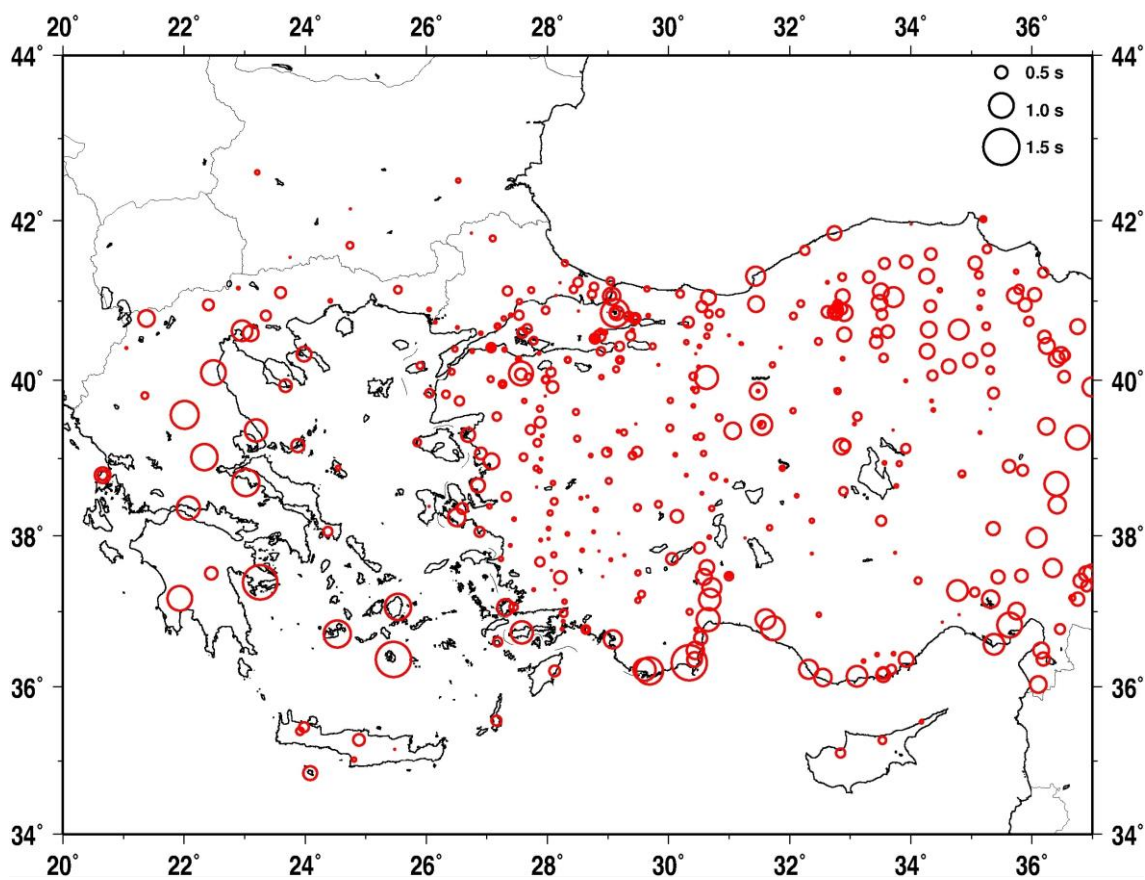


Figure 4.6. RMS of travel time residuals calculated from ak135. The size of the circle is proportional to the magnitude of the RMS in seconds.

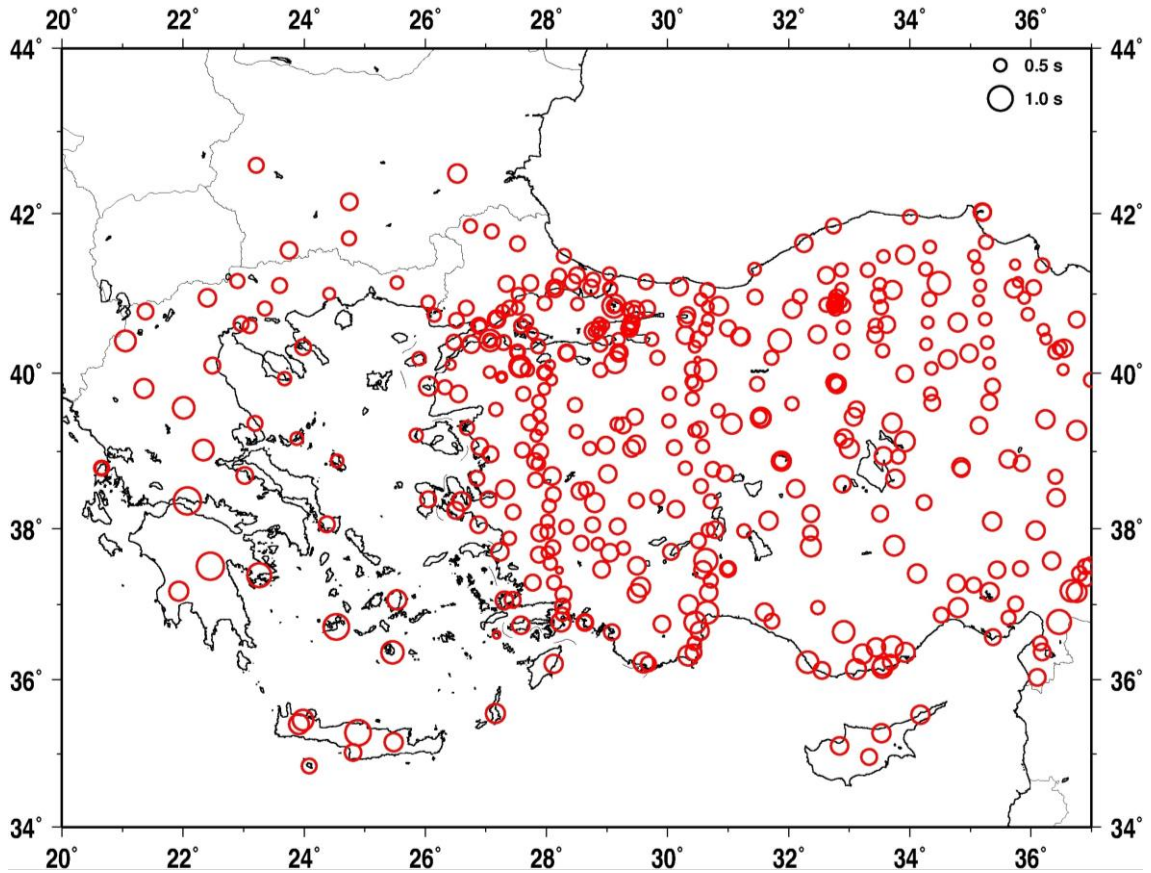


Figure 4.7. Standard deviation of travel time residuals calculated from ak135. The circles are scaled with the magnitude of the standard deviation in seconds.

### 4.1.3 Crustal Correction

The effect of the travel time perturbations caused by the crustal structure can be important in the telseismic tomography when the variations on the crustal thickness and velocities are large. Ak135 model assumes a 2 layered velocity model for the crust (Figure 4.8). Crustal correction is computed using the crustal model of Karabulut et al., (2019) and an average velocity of 6.4 km/s. For each event and each station crustal traveltimes were calculated from station to the base of the crust and write header of each waveform. Source correction terms are also determined during the inversion.

## 4.2 Model Parameterization and Ray Tracing

We construct a curved 3-D volume (Saltzer & Humphreys 1997; Frederiksen et al. 1998) with a 3-D grid of velocity nodes in spherical coordinates. Each node has an arbitrary depth dependent background values. These velocity values (Figure 4.8) belongs to depth are taken from the ak135 model. After each node has actual velocity with depth, smoothing process is applied by using cubic B-spline parameterization to stipulate the continuous velocity field. If the input 1-D model is not properly involved by the velocity grid, the code automatically generates a buffer layer of boundary nodes around the specified velocity model to facilitate the use of cubic B-splines. Based on the station spacing in the region, we decided that the grid spacing is  $0.75^\circ$  in the N-S direction and  $1.00^\circ$  E-W direction. We used 20 nodes in the N-S direction while 22 nodes in the EW direction. We used 50 km depth intervals and 16 nodes in depth reaching to a maximum depth of 800km.

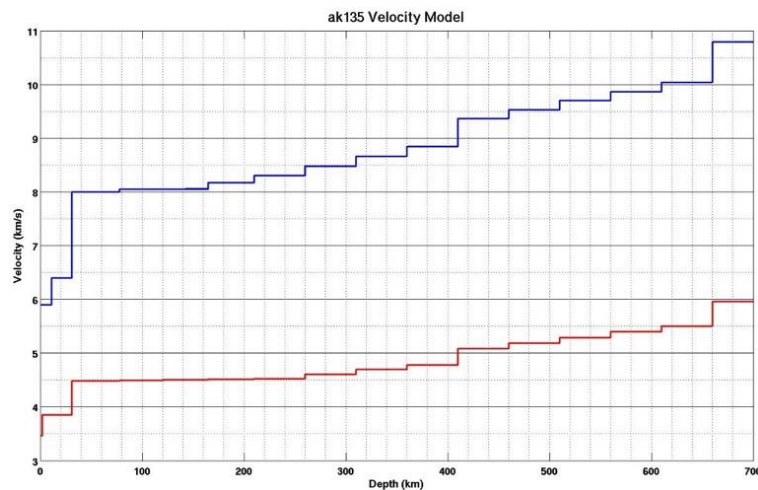


Figure 4.8. Ak135 velocity model used for constructing initial model. Blue line indicates P-wave velocity and red line indicates S-wave velocity regarding depth.

As the structure outside of the model volume does not affect relative arrival-time residual patterns significantly (Rawlinson et al., 2006a), we calculated travel times from the source to lower boundary of the model for each source according to the ak135 global reference model using  $t - p$  approach. FMM is used to calculate traveltimes from the base of the model to the receivers.

### 4.3 Selecting Smoothing and Damping Parameter

Regularization Constraints is solved using the SiM (Kennett et al. 1988), and we include both damping and smoothing regularization to address the problem of solution non-uniqueness. The forward travel-time prediction and inversion steps are applied iteratively to account for the non-linearity of the tomographic inverse problem. All calculations are carried out by FMTT (Fast Marching Teleseismic Tomography) Code (Rawlinson et al., 2006a).

Inversion part is carried out using six iterations of a 10-D subspace inversion routine with damping  $\varepsilon = 5.0$  and smoothing  $\eta = 10.0$ . Although damping and smoothing parameters are also adjusted from checkerboard tests with the same sources and receivers geometry, we construct trade-off curves. A various damping and smoothing parameters were tested and plot trade-off curves to estimate optimum damping and smoothing parameters. First we set the damping to a fixed value  $\varepsilon = 5.0$  and varying smoothing values. Figure 4.9a shows the trade-off curve between the residual data variance and roughness of the solution model. We select  $\eta = 10.0$  as the best value for minimization the data misfit and model roughness. For the second step, we set the smoothing to a fixed value  $\eta = 10.0$  and varying damping values. Trade-off curve suggested that  $\varepsilon = 5.0$  is the best value for minimization the data misfit and model variance shown in Figure 4.9b.

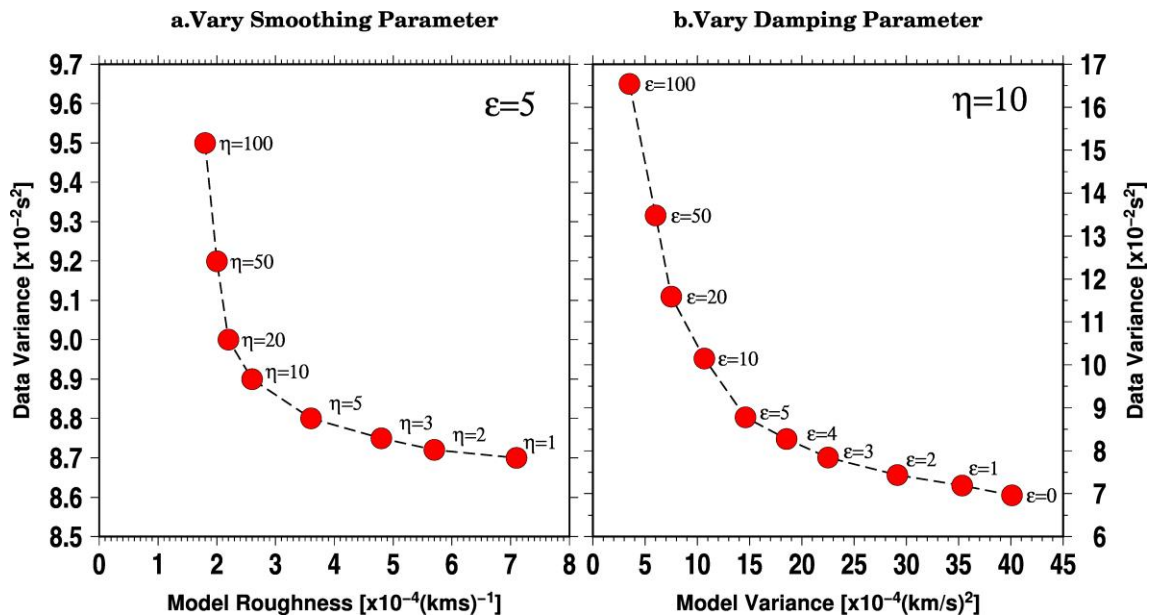


Figure 4.9. Trade-off curves used to estimate optimum smoothing and damping parameters. (a) Damping parameter fixed at  $\varepsilon = 5.0$  and smoothing parameter is changing.

In this case,  $\eta = 10.0$  is chosen from the curve. (b) Smoothing parameter fixed at  $\eta = 10.0$  and damping parameter is changing. The value  $\epsilon = 5.0$  is chosen as optimum.

After inversion, the final solution model reduces the data variance by 84% from  $0.51123 \text{ s}^2$  to  $0.08093 \text{ s}^2$ , which corresponds to an RMS reduction from 715.00 ms to 284.48 ms. Histograms that show the distribution of all relative arrival time residuals for the initial and final models are shown in Figure 4.10a and Figure 4.10b respectively.

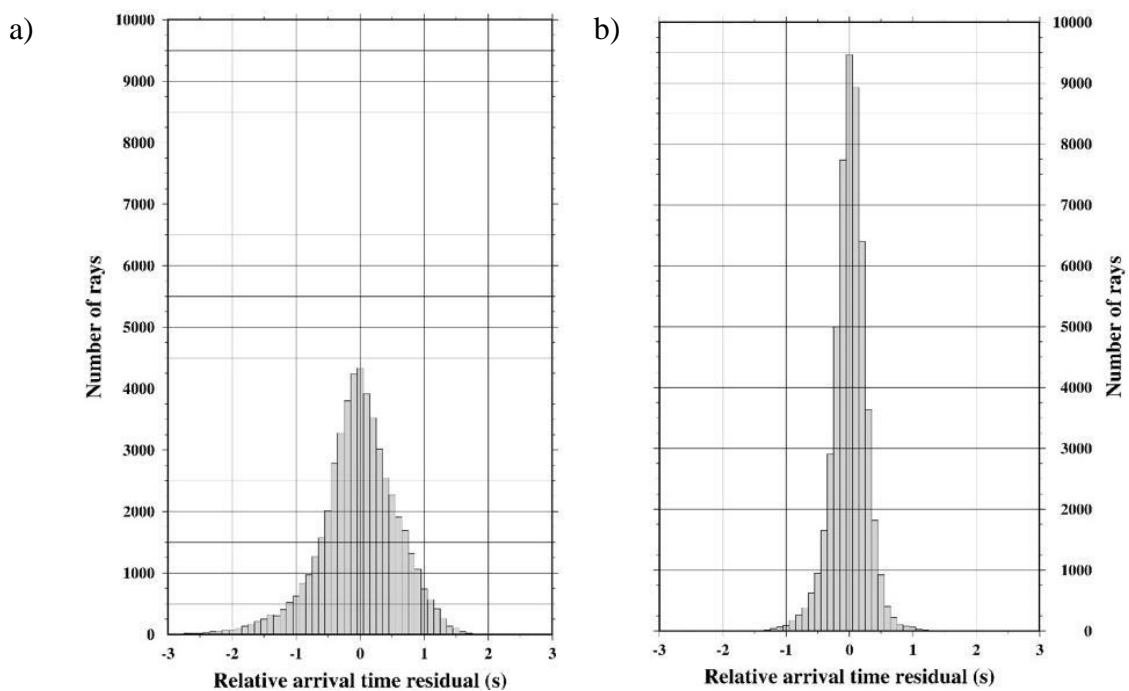


Figure 4.10 Frequency histograms showing fit to observed arrival time residual data of (a) Initial model and (b) final model.

#### 4.4 Resolution Test and Data Coverage

The reliability of the tomographic images should be tested before interpretation. First, we performed “checkerboard test” (Hearn and Clayton, 1986; Rawlinson and Sambridge, 2003) to check the resolving ability of the inversion for the given source and receiver geometry. We build initial models as box-car heterogeneities of opposite sign ( $\pm 50\%$ ), approximately 170 km in horizontal and 100 km vertical direction. The travel times for the checkerboard model are computed by applying FMM. Cubic B-spline functions (Rawlinson

et al., 2006a) are used to create a smoothly varying velocity continuum, which is controlled by a regular velocity grid with a node spacing of approximately 50 km vertical and ~80 km horizontal.

The tomographic images are sensitive to the azimuthal coverage of ray paths. We observe non-uniform ray path coverage due to the azimuthal distribution of the sources (Figure 4.2). As a result, smearing of anomalies can be seen in the horizontal, EW and NS slices. Despite these effects, the input model is well resolved (Figure 4.11), in sign, size and shapes of the anomalies and the edges of the box-car are detected in the best resolved part. However, the amplitudes of the perturbations are lower than the true values. The quality of the tomographic images reduces dramatically at the edge of our model due to sparse sampling. However, at center of the model the resolution is fairly good.

Vertical cross sections (Figure 4.11) show that resolved anomalies is amplified in size vertically but models are resolved well in sign. Because, smearing effect can be seen much more in the vertical direction than horizontal direction. Cross sections indicate that input model is well resolved up to 700 km depth. The upper mantle structure of the input model is well resolved than the deeper part as the number of ray crossing in the upper mantle is greater than the deeper parts.

Rawlinson et al., (2006b) indicated that there might be a problem of applying checkerboard tests to teleseismic data. Some anomalies may be smeared along predominant ray trajectories and they tend to merge with diagonally adjacent anomalies of the same sign. Therefore, an alternative test is carried out to recover short length scale anomalies, which are distributed throughout the model volume (Rawlinson and Sambridge, 2003). Four different spikes are located in input model at 150 km (Lat=38°N, Lon=23°E), 300 km (Lat=38°N, Lon=27°E), 450 km (Lat=38°N, Lon=31°E) and 600 km (Lat=38°N, Lon=35°E) with the amplitude of 0.5, -0.5, 0.5, -0.5 respectively. The input model is well resolved in the inversion (Figure 4.12), both in shape, size and sign of the anomaly horizontally. However vertical cross sections show the same amplification like in the checkerboard test.

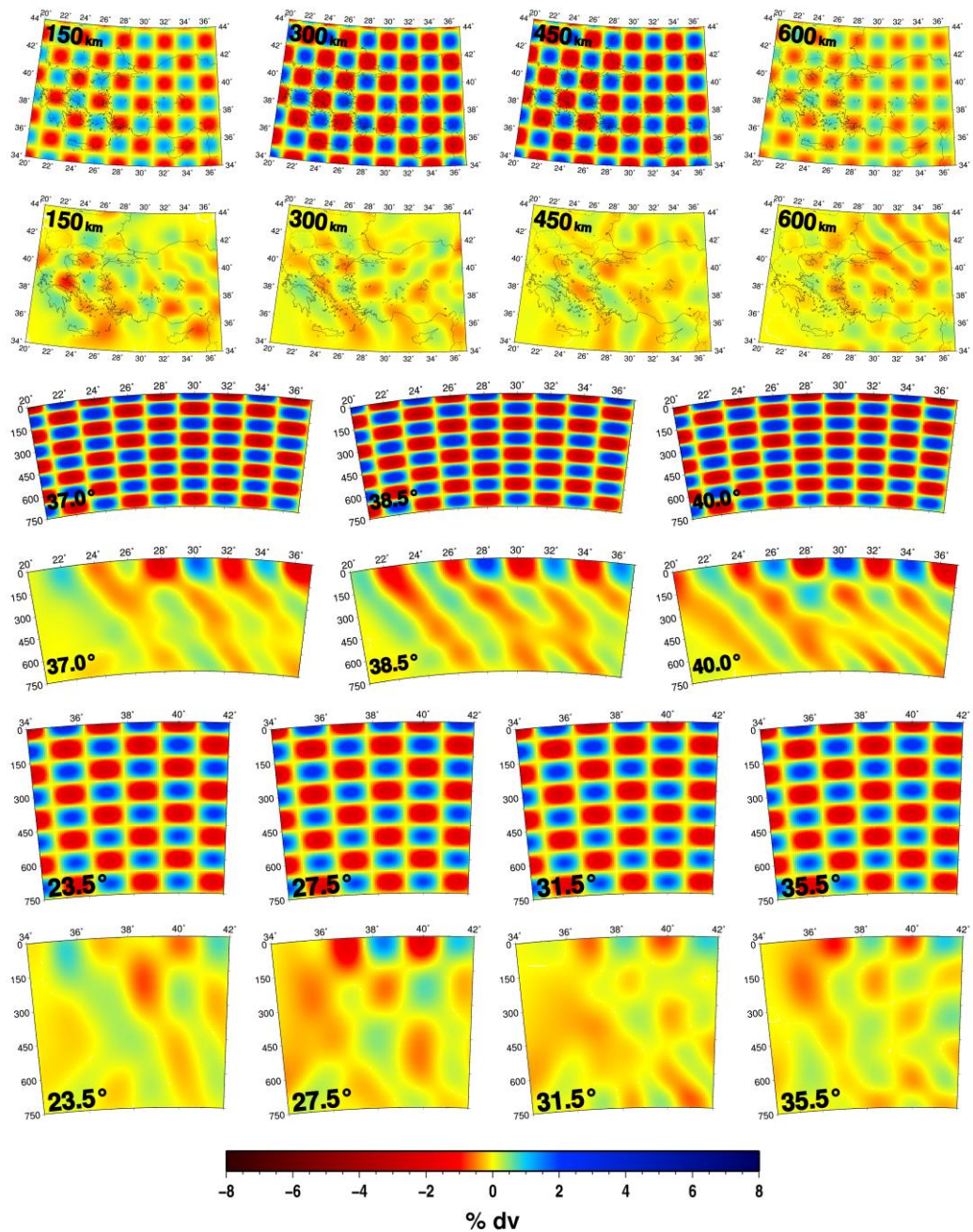


Figure 4.11. Synthetic checkerboard resolution test results. The 1<sup>st</sup> and 2<sup>nd</sup> row show horizontal slices taken through the input model at 150, 300, 450, 600 km depth and the recovered pattern of anomalies for the same depth. The 3<sup>rd</sup> and 4<sup>th</sup> rows show EW Cross-sections taken through the input at 37.0°N, 38.5°N and 40.0°N and the recovered pattern of anomalies for the same latitude with input model. The 5<sup>th</sup> and 6<sup>th</sup> rows show that NS Cross-sections taken through the input at 23.5°E, 27.5°E, 31.5°E, 35.5°E and the recovered pattern of anomalies for the same longitude with input model.

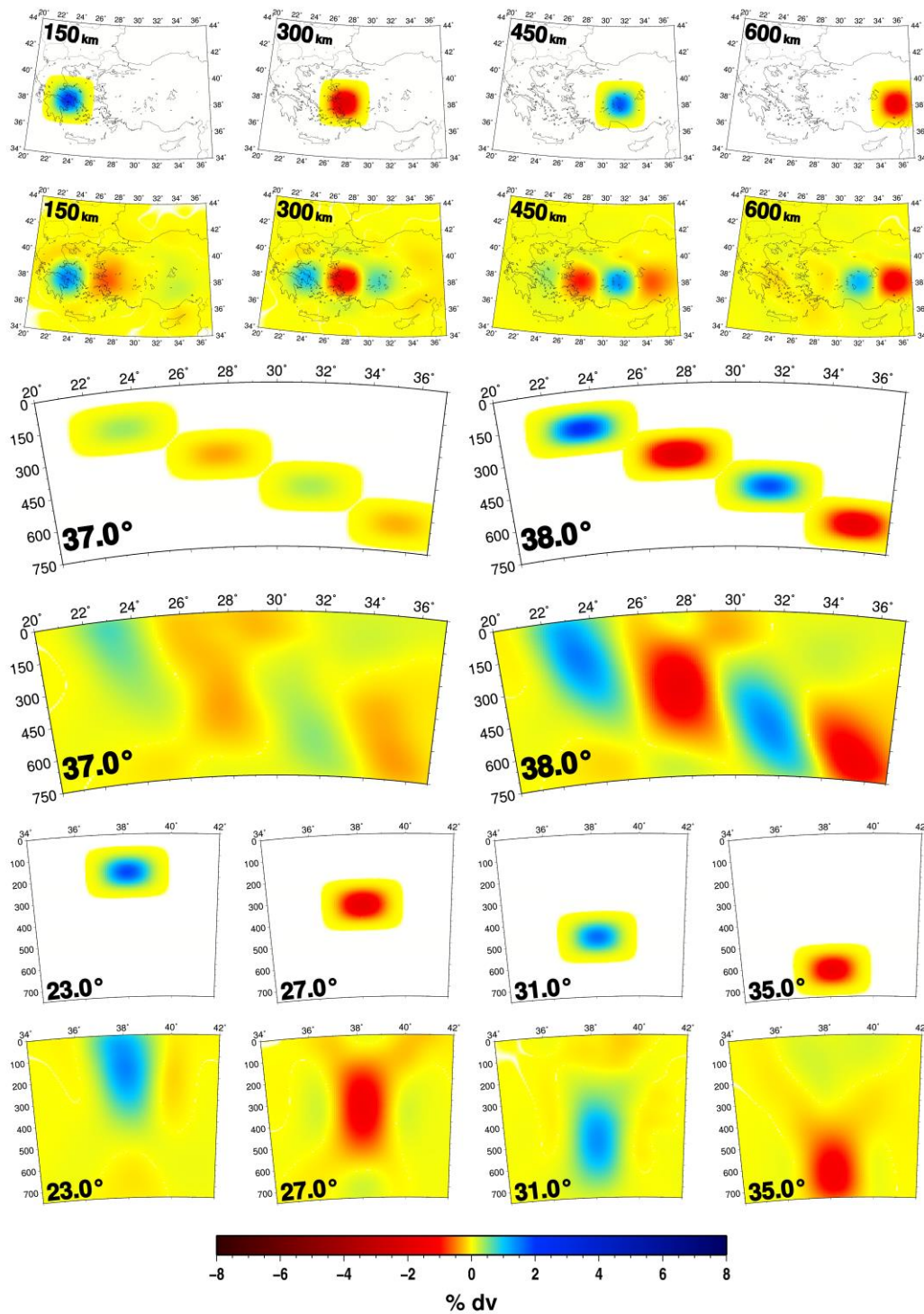


Figure 4.12 Synthetic spike resolution test results. The 1<sup>st</sup> and 2<sup>nd</sup> rows show horizontal slices taken through the input model and recovered pattern of anomalies at 150, 300, 450 and 600 km depth. The 3<sup>rd</sup> and 4<sup>th</sup> rows show Cross-sections through the input model and recovered pattern of anomalies at 37.0°N and 38.0°N. 5<sup>th</sup> and 6<sup>th</sup> rows show Cross-sections

through the input model and recovered pattern of anomalies at 23.0°E, 27.0°E, 31.0°E and 35.0°E.

## 4.5 Results

In this section, results of the Tomography are presented on Figure 4.13, Figure 4.14 and Figure 4.15, which show a series of horizontal and vertical cross-sections. The quality of the tomographic images reduces dramatically at the edge of our model due to sparse sampling. However, at center of the model the resolution is fairly good. Therefore, the fast anomaly associated with the corner side of Hellenic and Cyprus trenches is poorly resolved compared to interior of the study area. However, station spacing is good enough to ensure proper resolution of the major tectonic zones and structures (e.g. Aegean Slab).

At shallow depths, negative velocity perturbations are dominated in the northwest, southeast and center of the study area, and positive perturbations in the southwest and northeast (Figure 4.13\_50km-150km), which are broadly consistent with the arrival time residuals observed in Figure 4.4. The subducting Aegean slab first appears on the 50 km on the horizontal slice as a high velocity anomaly. High-velocity anomalies are concentrated towards the center as depth increases. At shallow depths general strike of the high velocity anomaly is NW-SE on the Hellenic Trench and E-W on the Cyprus trench. These two regions are separated by an N-S trending low velocity zone (Figure 4.13\_150km-650km) between 28°E-30°E longitudes. After 300 km, this zone becomes NE-SW oriented. Relatively fast anomalies can be observed at the north of the NAFZ between 28°E-37°E longitudes (Figure 4.13\_50km-100km). At CA, slow velocity perturbations reach to 150 km. After 150 km in the greater part of Anatolia is under the influence of fast velocity perturbation with trending NW-SE. After 400 km, segmented structure can be seen on the anomalies especially at Cyprus slab.

The EW cross-sections (Figure 4.14) also reflect the presence of high velocity perturbations in the southwest sector of the model. Fast velocity anomalies enlarge to the deeper part towards to the north. In Figure 4.14 north of 35.0°N, low velocity zone can be seen between Aegean and Cyprus slabs. Cyprus slab appears as segmented structures on 36.0°N-39.5°N. As shown in the horizontal sections, northward direction (39.0°N-39.5°N),

faster anomalies at the CA are concentrated in the range of 450-750 km. Visible evidence of structural smearing along dominant ray path orientations can be observed in particular.

It is easier to follow dipping slabs on the NS (Figure 4.15) cross-sections. Aegean slab can be seen clearly between 22.5°E to 27.5°E. After 28.0°E, slab does not have a continuity until 30.0°E. This part is filled with the low velocity zone between Aegean and Cyprus slab. Between 29.5°E and 35.0°E East and Western Cyprus slab can be seen. After 33.5° E, surface trace of the slab cannot be seen. As we move to the eastern part, anomalies with higher velocity accumulates towards deeper part. Relatively fast anomalies produced at the NAFZ are observed on many NS figures at shallow depth.

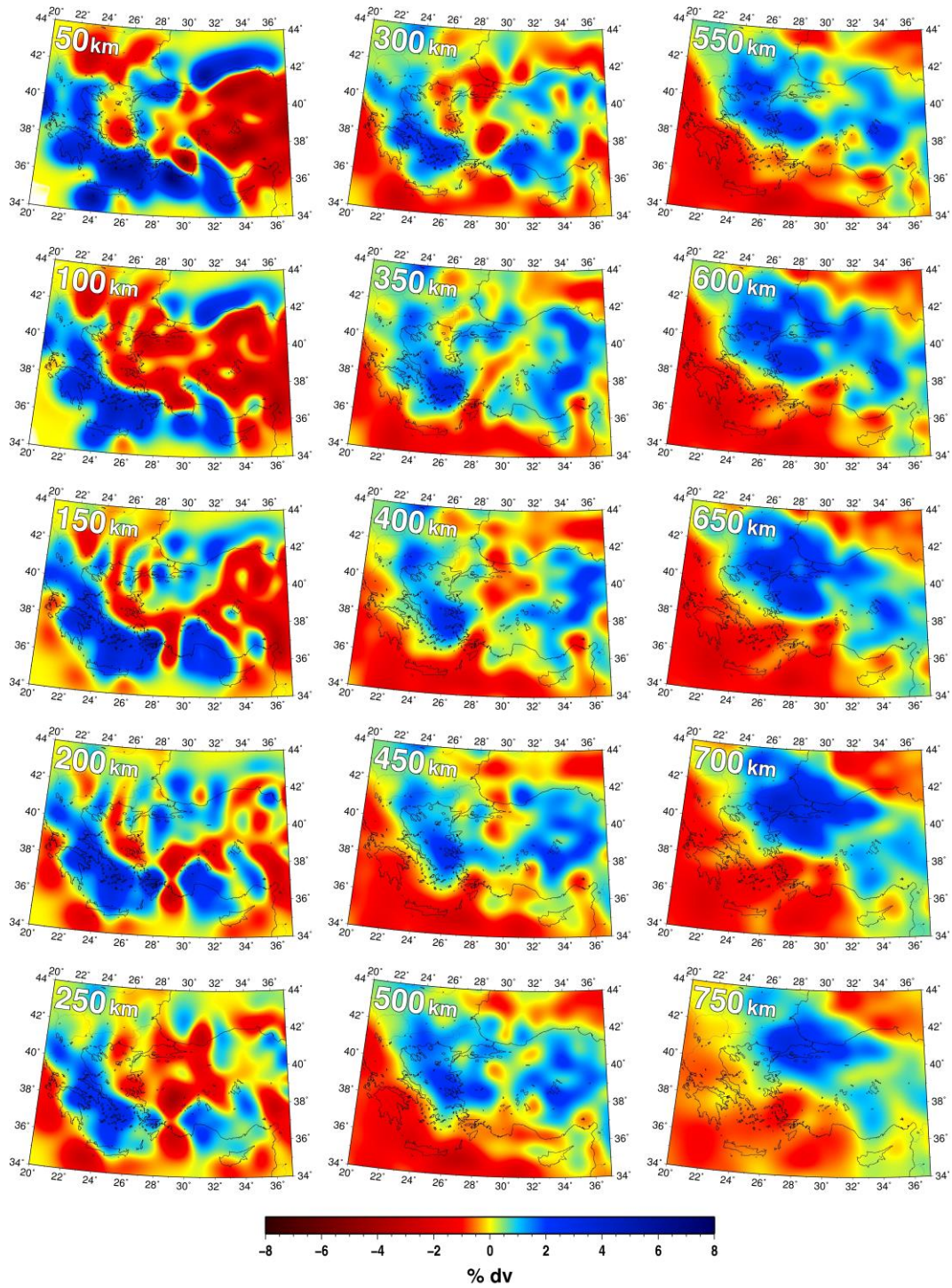


Figure 4.13 Horizontal sections through the three-dimensional final model from 50 km to 750 km with 50 km intervals as P-wave velocity perturbations from a reference one-dimensional model.

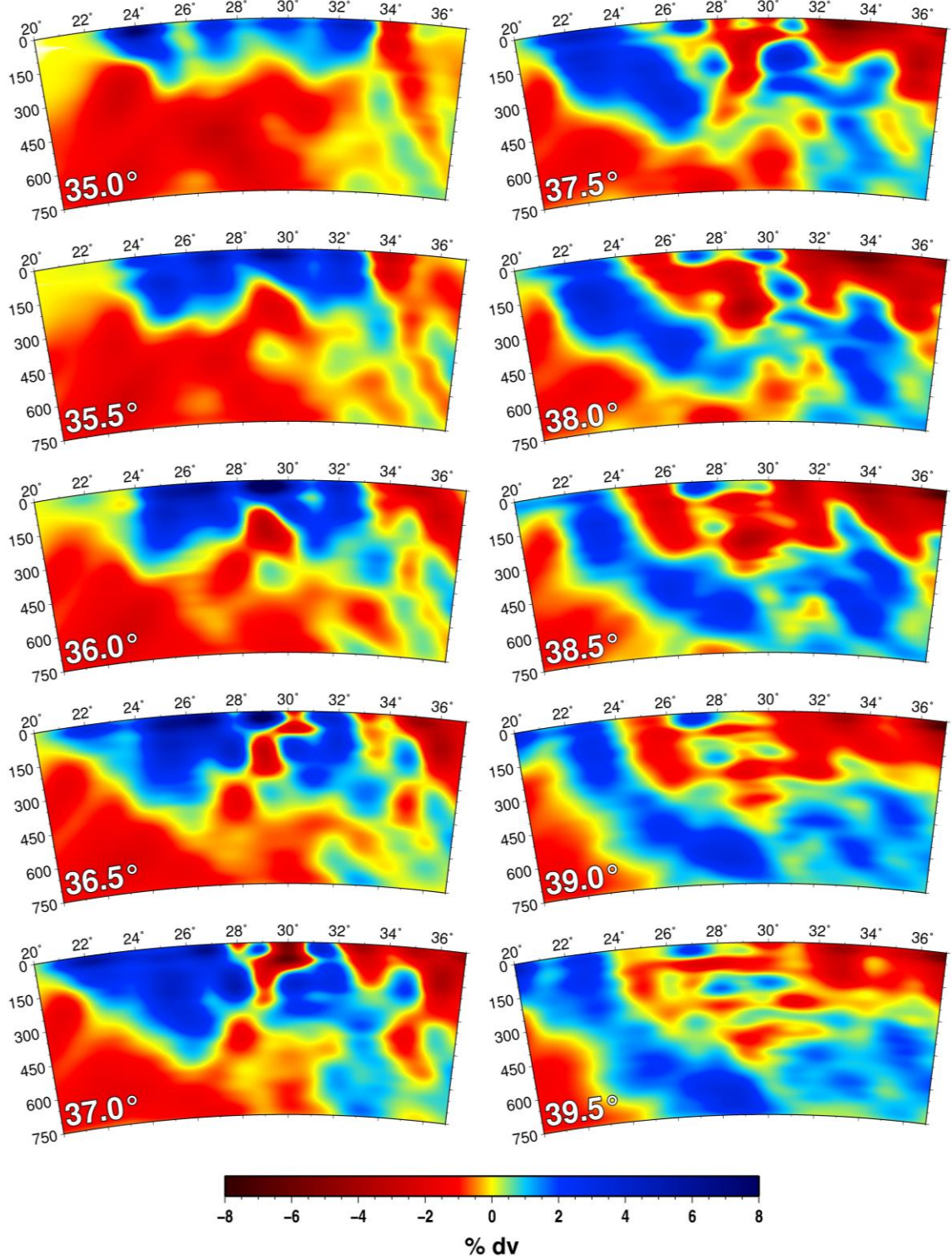


Figure 4.14. Cross-sections through the three-dimensional solution model at  $0.5^\circ$  intervals from  $35.0^\circ\text{N}$  to  $39.5^\circ\text{N}$  in East-West direction.

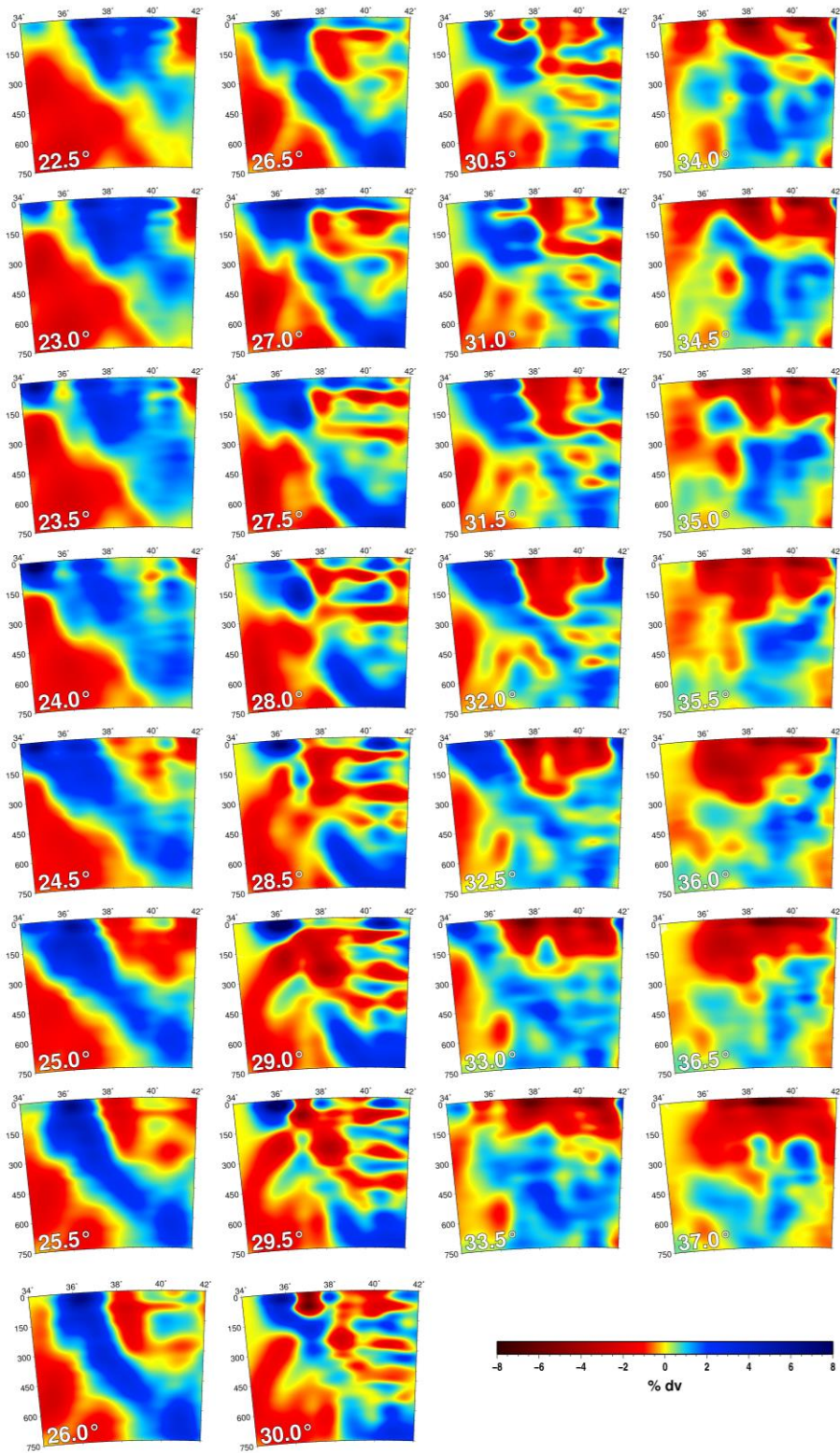


Figure 4.15. Cross-sections through the three-dimensional solution model at  $0.5^\circ$  intervals from  $22.5^\circ\text{E}$  to  $37^\circ\text{E}$  in North-South direction.

## 4.6 Discussion

In this section, we discussed our results with the previous studies. Figure 4.16 shows the map of study area with tectonic provinces and major structural features. Green dashed lines show the location of the nine cross section tomograms, which are shown in Figure 4.17 and Figure 4.18. The most noticeable structures in our model are the fast anomalies located beneath Hellenic and Cyprus trenches. These anomalies belong to the subducting slab of African oceanic lithosphere (Figure 4.17, A1-A1', A2-A2' and Figure 4.18, B-B', C-C', D-D', E-E', F-F', G-G'). The fast anomalies associated by the Aegean slab have also been detected by Spakman et al. (1988), Bijwaard et al. (1998), Piromallo & Morelli (2003), Biryol et al. (2011) and Portner et al. (2018) (Figure 4.17, A1-A1', A2-A2', Figure 4.18, B-B', C-C', D-D'). Cyprus Slab which was detected by Faccenna et al. 2006, Biryol et al. (2011) and Portner et al. (2018), is clearly observed after 29.5E longitude cross sections (Figure 4.18, E-E', F-F', G-G').

According to Salaün et al., 2012, Aegean slab dips with typical subduction angle. Eastern part of Aegean slab near tear dips northwestward with an angle of  $\sim 45^\circ$ . Western part of the Aegean slab dips northeastward with an angle of  $\sim 50^\circ$ . The Aegean slab generally shows a concave structure. According to our tomograms Cyprus slab dips  $\sim 45^\circ$  in western part (Figure 4.18, E-E') and eastern part of Cyprus Slab dips  $\sim 55^\circ$  (Figure 4.18, F-F'). At depths greater than  $\sim 300$  km both slabs merges and stays horizontal (Spakman 1985; Bijwaard et al. 1998; Piromallo & Morelli 2003; Biryol et al. 2011). This means the materials from the slabs accumulate between a few hundred km depths. The reason for this accumulation is the 660 km mantle transition zone and the material tends to penetrate to deeper part of the lower mantle (Faccenna et al., 2003). The fast velocity anomaly caused by the Aegean and the Cyprus slabs show a good harmonious relation with the Wadati-Benioff zone which reaches 200 km for Aegean slab (Figure 4.18, C-C'), 150 km for the western part of the Cyprus slab (Figure 4.18, E-E') and 100 km for the eastern part Cyprus slab (Figure 4.18, F-F')

Some studies have suggested that the Hellenic and Cyprus trenches are separated from each other on the south of Anaximander Mountains (ten Veen et al. 2004; Aksu et al. 2009). Biryol et al. 2011 and recent study Portner et al. 2018 confirmed that the termination of the

Cyprus Slab is at Isparta Angle in the west and along 34°–35° longitude in the east. The location of the west tip of the Cyprus Trench is confirmed by our study (Figure 4.15-29.0°E, 30.5°E) , but we also found that eastern termination of the Cyprus Trench started from 33.5°E at shallower depth (Figure 4.14-36.5°N, Figure 4.15-33.5°E). We observe shallow low velocity zone between 36.5°N-37.5°N (Figure 4.15-30.0°E, 30.5°E) but unlike Biryol et al. 2011, high velocity African lithosphere can be seen easily on the south of this region. We observe low velocity zone below Isparta angle where the crust is the thickest (Karabulut et al., 2019). According to Barka & Reilinger 1997 Isparta Angle zone may be an obstacle to the westward motion of Anatolia because at Isparta angle zone the velocity of the westward motion of the Anatolia is slower than the other part of the Anatolia. This kind of slow motion influenced by the obstruction and resulted with the slab steepening and detachment (Wortel & Spakman, 2000). A tear between the Aegean slab and Cyprus slab is observed on the east of Creete along the Pliny and Strabo Transform Faults (Figure 4.17, A1-A1', A2-A2'). Govers & Wortel (2005) described this kind of faults at the termination of the trenches as Subduction Transform Edge Propagator (STEP). Their explanation of the formation of the STEP zones is the differences of the velocity of trench retreats. Because the retreat of the Hellenic Trench is (~30 mm/year) faster than the movement rate of the Cyprus trench (~10 mm/year) (McClusky et al. 2003; Wdowinski et al. 2006).

A large tear (Pliny-Strabo Tear) is located between Aegean and Cyprus slabs, between 28.0°E-30.0°E longitudes (Figure 4.13\_125km-650km, Figure 4.17, A1-A1', A2-A2'). The N-S trending slow velocity anomalies extend up to 600 km in some region (Figure 4.17, A2-A2'). Many researchers studied this region as Isparta angle with a N-S trending tear (Wortel & Spakman 1992; Barka & Reilinger 1997; Dilek & Altunkaynak 2009; Dilek & Sandvol 2009; Biryol et al. 2011; Portner et al. 2018). Rising asthenosphere beneath the tear produces a slow anomaly over tear and may be the source of the forming Kirka-Afyon-Isparta (KAIVF) and Kula Volcanic Fields (KVF) (Figure 4.17, A1-A1', A2-A2', Figure 4.18, D-D', E-E'). The KVF and KAIVF are formed by the Pliocene–Pleistocene alkaline volcanism (Richardson-Bunbury 1996). This kind of volcanism can be obtained under the circumstances of existence rapid upwelling of asthenosphere (Gülen 1990 and Tokçaer et al. 2005). The volcanoes in KAIVF show a structure aging to the north Pliocene (~4 Ma) to Middle-late Miocene (~17 Ma) (Savaşçın & Oyman 1998; Dilek & Altunkaynak 2009). According to Dilek and Altunkaynak 2009, these phenomena can be explained by the

propagation of the tear between the Cyprus and the Aegean slabs. Because the oldest volcano is the northern one, rapid movement of the Hellenic Trench retreat might play an important role on this migration.

The other smaller tear (Antalya Bay Tear) is located along the Paphos transform fault between western and eastern part of Cyprus slab, after 400 km depth between  $31.5^{\circ}\text{E}$  and  $32.5^{\circ}\text{E}$  (Figure 4.13 400km, 450km, Figure 4.17, A2-A2'). For the formation of the quaternary Central Anatolia Volcanic Zone (CAVZ) some studies (e.g. Dilek & Sandvol 2009) argue that the existence of the detachment at the shallow dipping Cyprus slab, but our images revealed that there is no detachment on the slab (Figure 4.18 E-E', F-F', G-G'). Although Kuşçu & Geneli 2010 reported that CAVZ and the composition of the associated volcanism indicate a clear subduction component, Biryol et al. 2011 claimed that the eastern sector of the Cyprus slab is too deep ( $\sim 250$  km) beneath the CAVZ to explain the young volcanism there. Our results may verify this claim (Figure 4.18, F-F', G-G'). There are two views for this area. First view is, the dip of the slab was shallower during Eocene–Early Miocene time (Savaşçın & Oyman 1998), and the volcanic material came from the shallower slab. Second view defends that the source of the materials at the CAVZ is the asthenosphere itself (Aydın 2008). It is easy to see a thick hot material with low velocity anomaly under CAVZ (Figure 4.18, F-F', G-G'). In addition, Nolet (2009) argued that because the complexity of the mechanism at eastern Cyprus slab, multiple detachment may be occurred. In Figure 4.18, F-F' we observe these “Blocky” (Biryol et al. 2011) structures but we propose these blocky structures are not detached each other completely.

It may be reasonable to partition Anatolia according to tectonic features. Western Anatolia Extensional Province (WAEP), Central Anatolia Province (CAP), North Anatolian Province (NAP) and The East Anatolian Contractional Province (EACP) are the main regions. WAEP and CAP split at the northern part of the Isparta angle (Barka & Reilinger 1997; Bozkurt 2001). WAEP is under influence of Extensional regime, which is the result of the weaker crust (Dilek & Altunkaynak, 2009). Weaker crust correlates with our results that slow velocity anomaly from tear under WAEP (Figure 4.17, A1-A1', A2-A2') and high heat flow from the study of İlkışık 1995. We cannot see a good correlation with the eastern side of the tear and the boundary between WAEP and CAP at  $39^{\circ}$  N, but the largest portion of the tear is located under WACP (Figure 4.17, A1-A1', A2-A2'). We can see the western

end of the EACP in the Figure 4.18, H-H', but the slow anomaly of the EACP correlates with the slow anomaly in the CAP, Figure 4.18, G-G'. This region is between 35°E-37°E and DSFZ is located right in this interval Figure 4.17, A1-A1', A2-A2'.

Slow velocity anomaly can be seen between 100 km and 600 km depth on the figure Figure 4.17, A2-A2' and Figure 4.18, G-G'. This region is located between the Cyprus and Dead Sea fault zone. However, it is hard to refer this region as tear, because it is at the end of the Cyprus slab. We need further investigation of this region. In Figure 4.18, G-G' and H-H', we cannot see fast velocity anomaly belong to Cyprus slab at shallower part. However, the rest of the slab can be observed after 250 km depth with fragmented structure.

We found fast velocity anomaly in Istanbul Zone (IZ) at the northern part of our study area in Figure 4.18, D-D', E-E'. Bozkurt 2001 described this region, which is characterized by strongly deformed, imbricated Precambrian to Late Paleozoic basement of the so-called Eastern and Western Pontides. Thus, thicker and older lithosphere of the northern Anatolian province causes this fast anomaly (Biryol et al. 2011). We observe sharp difference between north and south part of the NAFZ in Figure 4.18, E-E' for a lithospheric scale but in D-D', we cannot see a sharp difference in velocity contrast and we see a tongue-like slow velocity contrast in fast region. Anomaly of IZ shows different size and shape on the different slices but average velocity perturbation for the IZ is 4% and it extends up to 150 km vertically.

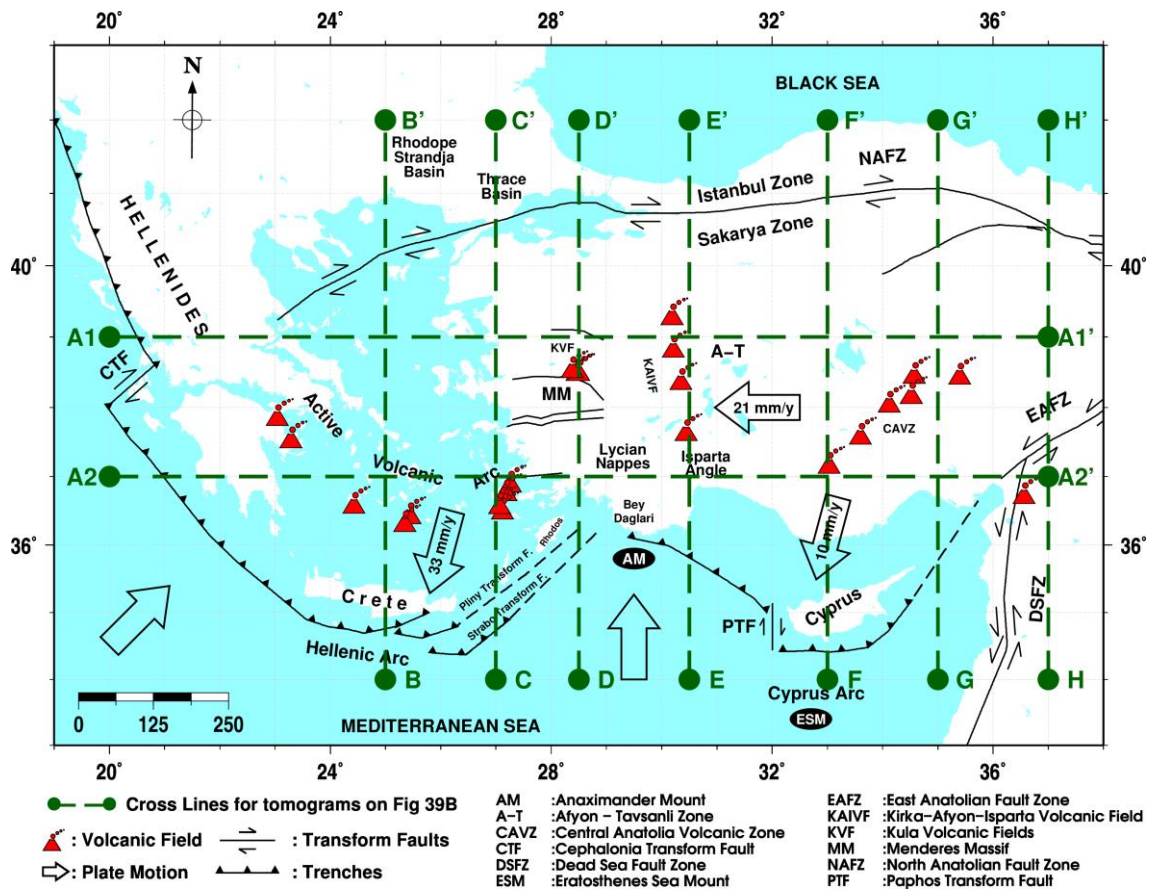


Figure 4.16 Map of study area including tectonic provinces, major structural features. Green dashed lines show the location of the cross sections tomograms shown in Figure 4.17 and Figure 4.18.

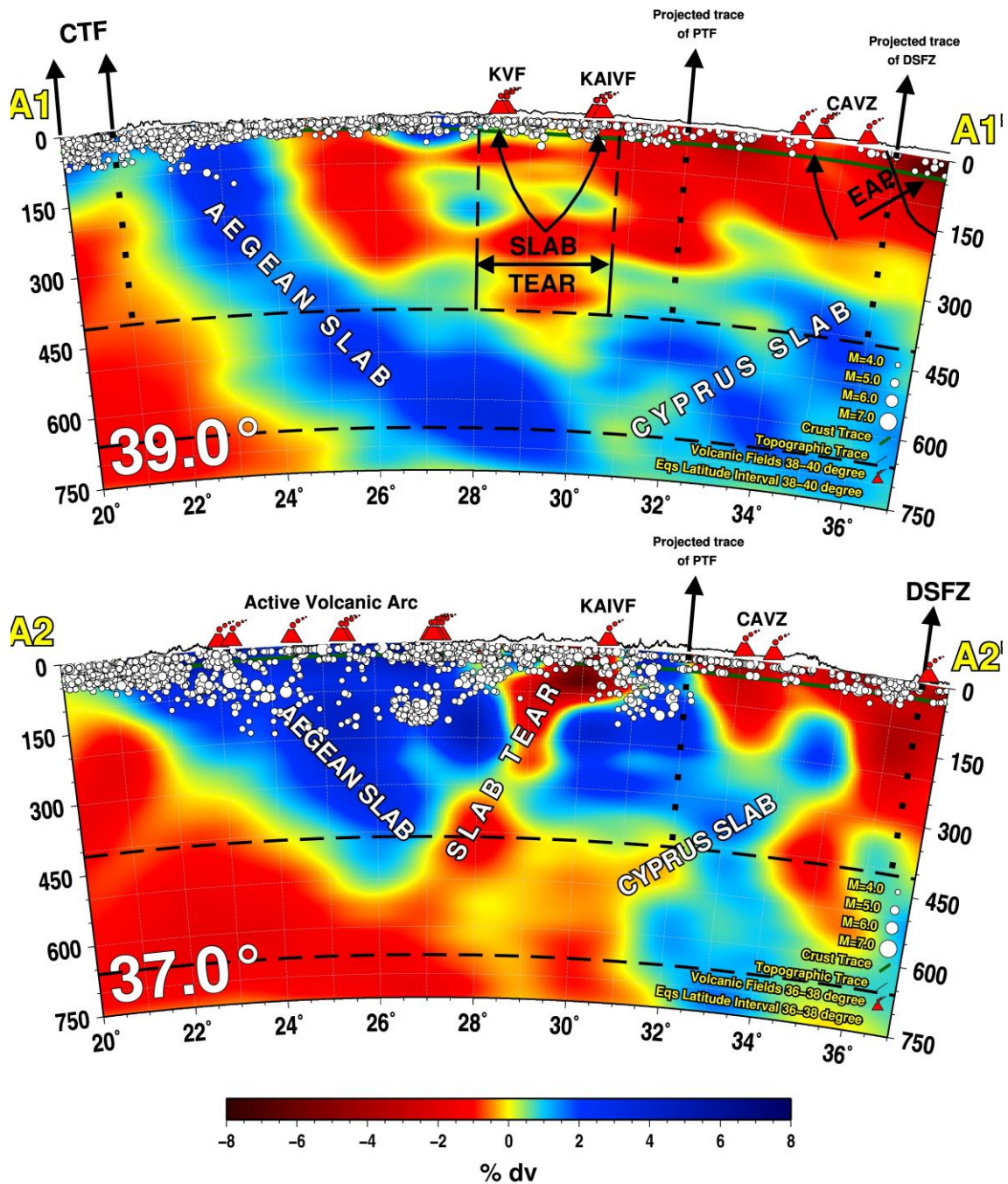


Figure 4.17 Cross sections taken through the A1-A1' (39.0°N) and A2-A2' (37.0°N) profiles. Small white circles are the earthquake hypocenters ( $M_w \geq 4.0$ ) for the period 1973-2017 taken from USGS. Topographic profiles are plotted at the top of the images with the 10x exaggeration. Green line indicates bottom line of the crust. Black dashed horizontal lines indicate 410 km and 660 km discontinuities. Red colors indicated slow velocities and blue color indicates fast velocities.

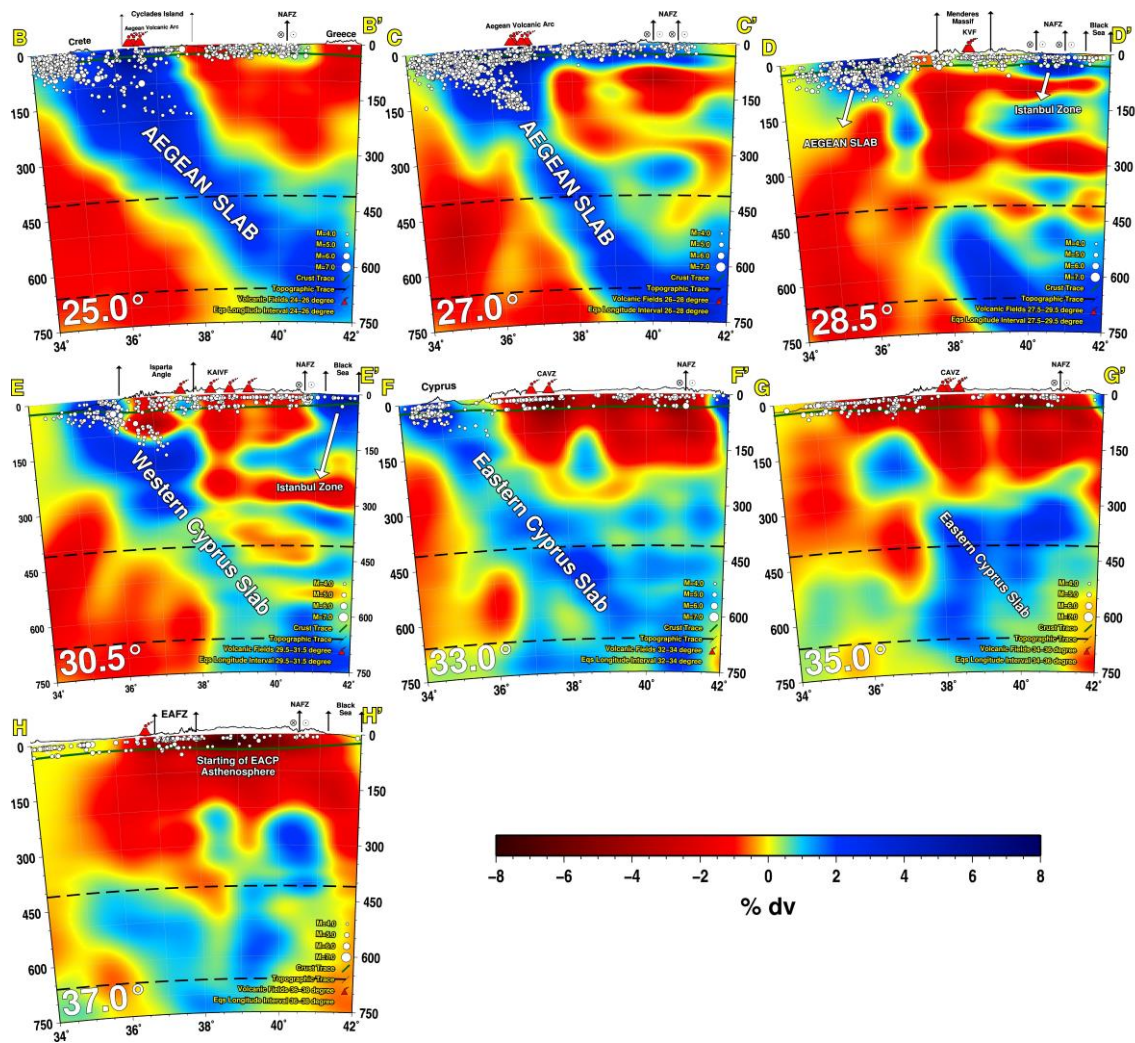


Figure 4.18 Cross sections taken through the B-B' (25.0°E), C-C' (27.0°E), D-D' (28.5°E), E-E' (30.5°E), F-F' (33.0°E), G-G' (35.0°E), and H-H' (37.0°E) profiles. See Figure 4.17 for details.

## 5. CONCLUSIONS

Mantle structure of our study area has been studied in different aspects by many researchers for more than 30 years. We perform high-resolution P-wave travel time tomography for the Aegean-Anatolian region. We combine different dataset from different networks and projects. The main large and small-scale structures were identified by our study.

This study was motivated by the goal of further enhancing the resolution of the tomographic image in the study area. The strength of this study is the huge dataset over a long time interval. The most important contribution of this study is the high-resolution images of the study area. Our images reach to 700 km. In addition, crustal correction is applied to our travel times with the new crustal thickness data (Karabulut et al., 2019).

The most important result from the tomography is the structure of the African lithosphere, which submerge under Aegean and Anatolian region. The African lithosphere, which lies beneath the Aegean and Anatolia, has emerged as a fragmented structure. These structures are the Aegean and Cyprus slabs which separated each other by the Pliny-Strabo Tear in the line Isparta Angle. Cyprus slab split into two parts at the Paphos Transform Fault Zone by the Antalya Bay Tear. The regions of tears are full with slow velocity materials, which may feed major volcanic fields (KVF, KAIVF and CAVZ). The apex of the tear zones lies within the Isparta Angle. The velocity contrast between north and south portion of the NAFZ can be observed clearly especially on Marmara region at first 150 km.

The dipping angles for the slabs (Aegean, Cyprus) are different each other. This difference, the tears and the Isparta angle may be resulted from the differences in retreat velocity at Hellenic and Cyprus trenches. Both slabs merge at the 660 discontinuity. Aegean slab passes mantle transition zone without deforming, however according to our results Cyprus slab shows a deformed structure after mantle transition zone.

## REFERENCES

Achauer, U., “A study of Kenya rift using delay time tomography analysis and gravity modelling”, *Tectonophysics*, 209, pp. 197–207, 1992

Aki, K., A. Christoffersson, and E. S. Husbeye, “Determination of the three-dimensional seismic structure”, *J. Geophys. Res.*, 82(2), pp. 277-296, 1977.

Aki, K., and W. H. K. Lee, “Determination of the three-dimensional velocity anomalies under a seismic array using first P arrival times from local earthquakes 1. A homogeneous initial model”, *J. Geophys. Res.*, 81, pp. 4381–4399, 1976.

Aksu, A. E., J. Hall, and C. Yaltrak, “Miocene-Recent evolution of Anaximander Mountains and Finike Basin at the junction of Hellenic and Cyprus Arcs, eastern Mediterranean”, *Mar. Geol.*, 258, pp. 24–47, 2009.

Aktug, B., J.M. Nocquet, A. Cingöz, B. Parsons, Y. Erkan, P. England, O. Lenk, M.A. Gürdal, A. Kilicoglu, H. Akdeniz, and A. Tekgül, “Deformation of western Turkey from a combination of permanent and campaign GPS data: limits to block-like behavior”, *Journal of Geophysical Research*, 114, B10404, 2009.

Armijo, R., F. Flerit, G. King, and B. Meyer, “Linear elastic fracture mechanics explains the past and present evolution of the Aegean”, *Earth and Planetary Science Letters*, 217, pp. 85–95, 2003.

Armijo, R., H. Lyon-Caen, and D. Papanikolaou, “East–west extension and Holocene normal fault scarps in the Hellenic arc”, *Geology*, 20, pp. 491–494, 1992.

Armijo, R., B. Meyer, A. Hubert, and A. Barka, “Westward propagation of the north Anatolian into the northern Aegean: timing and kinematics”, *Geology*, 27 (3), pp. 267–270, 1999.

Armijo, R., B. Meyer, G. C. P. King, A. Rigo, and D. Papanastassiou, "Quaternary evolution of the Corinth Rift and its implications for the Late Cenozoic evolution of the Aegean", *Geophysical Journal International*, 126, pp. 11–53, 1996.

Auer, L., L. Boschi, T. W. Becker, T. Nissen-Meyer, and D. Giardini, "Savani: A variable-resolution whole-mantle model of anisotropic shear-velocity variations based on multiple datasets", *J. Geophys. Res. Solid Earth*, 119, pp. 3006-3034, 2014.

Aydin, F., "Contrasting complexities in the evolution of calc-alkaline and alkaline melts of the Nigde volcanic rocks, Turkey: textural, mineral chemical and geochemical evidence", *Eur. J. Mineralogy*, 20(1), pp. 101–118, 2008

Barka, A. A., and R. Reilinger, "Active tectonics of the Mediterranean region: deduced from GPS, neotectonic and seismicity data", *Annali di Geofisica*, 40(3), pp. 587–610, 1997.

Barka, A. A., and K. Kadinsky-Cade, "Strike-slip fault geometry in Turkey and its influence on earthquake activity", *Tectonics*, 7(3), 663-684, 1988.

Becel, A., M. Laigle, B. de Voogd, A. Hirn, T. Taymaz, A. Galve, H. Shimamura, Y. Murai, J. C. Lépine, M. Sapin, and S. Ozalaybey, "Moho, crustal Architecture and deep deformation under the North Marmara Trough, from the SEISMARMARA Leg 1 offshore-onshore reflection-refraction survey", *Tectonophysics*, 467, pp. 1–21, 2009.

Bijwaard H., W. Spakman, and R. Engdahl, "Closing the gap between regional and global travel time tomography", *J. geophys. Res.*, 103(B12), pp. 30055–30078, 1998.

Biryol, C. B., S. L. Beck, G. Zandt, and A. A. Özacar, "Segmented African lithosphere beneath the Anatolian region inferred from teleseismic P-wave tomography", *Geophys. J. Int.*, 184, pp. 1037-1057, 2011.

Blundell, C. A., Resolution analysis of seismic P-wave velocity estimates using reflection tomographic inversion, Ph.D. Thesis, Monash University, 1993.

Boray, A., F. Saroglu, and O. Emre, “Isparta bolumunun Kuzey Kesminde D-B Daralma icin bazi veriler”, *Jeoloji Mühendisligi*, 23, pp. 9–20, 1985.

Boschi, L., and A. M. Dziewonski, “‘High’ and ‘low’ resolution images of the Earth's mantle-implications of different approaches to tomographic modeling”, *J. Geophys. Res.*, 104, pp. 25567-25594, 1999.

Bozkurt E., “Neotectonics of Turkey-a synthesis”, *Geodin. Acta*, 14, pp. 3–30, 2001.

Bozkurt, E., and R. Oberhänsli, “Menderes Massif (Western Turkey): structural, metamorphic and magmatic evolution - a synthesis”. *International Journal of Earth Sciences* 89, pp. 679–708, 2001.

Bozkurt, E., and H. Sözbilir, “Tectonic evolution of the Gediz Graben: field evidence for an episodic, two-stage extension in western Turkey”, *Geological Magazine*, 141, pp. 63–79, 2004.

Brun, J.P., and C. Faccenna, “Exhumation of high-pressure rocks driven by slab rollback”, *Earth and Planetary Sciences Letters*, 272, pp. 1–7, 2008.

Bulant, P., “Two-point ray-tracing and controlled initial-value ray-tracing in 3-D heterogeneous block structures”, *J. Seismic Explor.*, 8, pp. 57–75, 1999.

Cetinkaplan, M., O. Candan, R. Oberhänsli, and R. Bousquet, “Pressure–temperature evolution of lawsonite eclogite in Sivrihisar; Tavşanlı Zone–Turkey”, *Lithos*, 104 (1–4), pp. 12–32, 2008.

Chou, C. W., and J. R. Booker, “A Backus–Gilbert approach to inversion of travel time data for three-dimensional velocity structure”, *Geophys. J. Royal Astr. Soc.*, 59, pp. 325–344, 1979.

Constable, S. C., R. L. Parker, and C. G. Constable, "Occam's inversion a practical algorithm for generating smooth models from EM sounding data". *Geophysics*, 52 (3), pp. 289-300, 1987.

Cosentino, D., T. F. Schildgen, P. Cipollari, C. Faranda, E. Gliozzi, N. Hudackova, S. Lucifora, and M. R. Strecker, "Late Miocene surface uplift of the southern margin of the Central Anatolian Plateau, Central Taurides, Turkey", *Geological Society of America Bulletin*, 124(1-2), pp. 133-145, 2012.

Dewey, J. F. and A. M. C. Şengör, "Aegean and surrounding regions: Complex multiplate and continuum tectonics in a convergent zone", *Geological Soc. of Am. Bull.*, 90, pp. 84-92, 1979.

Dilek Y., and E. Sandvol, "Seismic structure, crustal architecture and tectonic evolution of the Anatolian-African Plate Boundary and the Cenozoic Orogenic Belts in the Eastern Mediterranean Region", *J. geol. Soc. Lond.*, 327, pp. 127–160, 2009.

Dilek Y., and S. Altunkaynak, "Geochemical and temporal evolution of Cenozoic magmatism in western Turkey: mantle response to collision, slab break-off, and lithospheric tearing in an orogenic belt", *J. geol. Soc. Lond.*, 311, pp. 213–233, 2009.

Dziewonski, A. M. and D. L. Anderson, "Preliminary reference Earth model, *Physics of the Earth and Planetary Interiors*, 25, pp. 297-356, 1981.

Evans, J., U. Achauer, "Teleseismic velocity tomography using the ACH method; theory and application to continental-scale studies", in: H. Iyer, K. Hirahara (Eds.), *Seismic Tomography: Theory and Practice*, Chapman and Hall, London, 319–360, 1993.

Faccenna, C., T. W. Becker, L. Auer, A. Billi, L. Boschi, J. P. Brun, F. A. Capitanio, F. Funiciello, F. Horváth, L. Jolivet, C. Piromallo, L. Royden, F. Rossetti, and E. Serpelloni, "Mantle dynamics in the Mediterranean", *Rev. Geophys.*, 52, pp. 283-332, 2014.

Faccenna, C., O. Bellier, J. Martinod, C. Piromallo, and V. Regard, "Slab detachment beneath eastern Anatolia: a possible cause for the formation of the North Anatolian fault". *Earth and Planetary Science Letters*, 242(1-2), 85–97, 2006.

Faccenna, C., L. Jolivet, C. Piromallo, and A. Morelli, "Subduction and the depth of convection in the Mediterranean mantle", *J. Geophys. Res.*, 108(B2), 2099, 2003.

Farra, V., and R. Madariaga, "Non-linear reflection tomography", *Geophysical Journal International*, 95(1), pp. 135–147, 1988.

Floyd, M.A., H. Billiris, D. Paradissis, G. Veis, A. Avallone, P. Briole, S. McClusky, J.M. Nocquet, K. Palamartchouk, B. Parsons, and P.C. England, "A new velocity field for Greece: implications for the kinematics and dynamics of the Aegean", *Journal of Geophysical Research*, 115, B10403, 2010.

Frederiksen, A.W., M.G. Bostock, J.C. Van Decar, and J.F. Cassidy, "Seismic structure of the upper mantle beneath the northern Canadian Cordillera from teleseismic travel-time inversion", *Tectonophysics*, 294, pp. 43-55, 1998

Gençaliolu Kuşçu, G., and F. Geneli, "Review of the postcollisional volcanism in the Central Anatolian Volcanic Province (Turkey), with special reference to the Tepekoy Volcanic Complex", *International Journal of Earth Sciences*, 99(3), pp. 593-621, 2010.

Govers, R., and M. J. R. Wortel, "Lithosphere tearing at STEP faults: response to edges of subduction zones", *Earth planet. Sci. Lett.*, 236, 505–523, 2005.

Graeber, F.M., and G. Asch, "Three-dimensional models of P wave velocity and P-to-S velocity ratio in the southern central Andes by simultaneous inversion of local earthquake data", *J. Geophys. Res.*, 104, pp. 20237–20256, 1999.

Grand, S. P., "Global seismic tomography: a snapshot of convection in the Earth", *GSA Today*, 7, pp. 1–7, 1997.

Gülen, L., “Isotopic characterisation of Aegean Magmatism and geodynamic evolution of the Aegean Subduction”, in <Intern. Earth Sci. Collq. on the Aegean Region - IESCA 90, Proceedings> eds. Savaşçın and Eronat, Vol. II, pp. 143-166, 1990.

Hearn, T. M., and R. W. Clayton, “Lateral velocity variations in southern California. I. Results for the upper crust from Pg waves”, *Bull. Seism. Soc. Am.*, 76, pp. 495–509, 1986.

İlkışık, M.O., “Regional heat flow in western Anatolia using silica temperature estimates from thermal springs”, *Tectonophysics*, 244, pp. 175–184, 1995.

Isik, V., O. Tekeli, and G. Seyitoglu, “The  $^{40}\text{Ar}/^{39}\text{Ar}$  age of extensional ductile deformation and granitoid intrusion in the northern Menderes core complex: implications for the initiation of extensional tectonics in western Turkey”. *Journal of Asian Earth Sciences*, 23, pp. 555–566, 2004.

Iyer, H., “Seismic tomography”, in D. James, ed., *The encyclopedia of solid earth geophysics*, Van Nostrand-Reinhold, pp. 1133– 1151, 1989.

Jackson, J., “Active tectonics of the Aegean region”, *Annual Review of Earth and Planetary Sciences*, 22, pp. 239–271, 1994.

Jolivet, L., J. P. Brun, “Cenozoic geodynamic evolution of the Aegean region”, *International Journal of Earth Sciences*, 99, pp. 109–138, 2010.

Jolivet, L., C. Faccenna, “Mediterranean extension and the Africa–Eurasia collision”, *Tectonics*, 19 (6), pp. 1095–1106, 2000.

Jolivet, L., C. Faccenna, B. Huet, L. Labrousse, L. Le Pourhiet, O. Lacombe, E. Lecomte, E. Burov, Y. Denèle, J. P. Brun, M. Philippon, A. Paul, G. Salaün, H. Karabulut, C. Piromallo, P. Monié, F. Gueydan, A. I. Okay, R. Oberhänsli, A. Pourceau, R. Augier, L. Gadenne, and O. Driussi, “Aegean tectonics: strain localisation, slab tearing and trench retreat”, *Tectonophysics*, 597–598, pp. 1–33, 2013.

Julian, B. R. and D. Gubbins, “Three-dimensional seismic ray tracing”, *J. Geophys.*, 43, 95–113, 1977.

Kahle, H.G., M. V. Müller, A. Geiger, G. Danuser, S. Mueller, G. Veis, H. Billiris, and D. Paradisis, “The strain field in NW Greece and the Ionian Islands: results inferred from GPS measurements”, *Tectonophysics*. 249, pp. 41–52, 1995.

Karabulut, H., A. Paul, A. D. Özbakır, T. Ergün, and S. Şentürk, “A new crustal model of the Anatolia-Aegean domain: evidence for the dominant role of isostasy in the support of the Anatolian plateau”, *Geophysical Journal International*, 218, 1, pp. 57–73, 2019.

Kennett, B. L. N., E. R. Engdahl, and R. Buland, “Constraints on seismic velocities in the Earth from travel times”, *Geophys. J. Int.*, 122, pp. 108-124, 1995.

Kennett, B. L. N., M. S. Sambridge, and P. R. Williamson, “Subspace methods for large-scale inverse problems involving multiple parameter classes”, *Geophysical Journal International*, 94, pp. 237–247, 1988.

Ketin, I., “Über die tektonisch-mechanischen Folgerungen aus den grossen anatolischen Erdbeben des letzten Dezenniums”, *Geol. Rundsch.*, 36, pp. 77-83, 1948.

Kissling, E., S. Husen, and F. Haslinger, “Model parametrization in seismic tomography: a choice of consequence for the solution quality”, *Phys. Earth Planet. Inter.*, 123, pp. 89-101, 2001.

Koçyiğit, A., “Superimposed basins and their relations to the recent strike-slip fault zone: a case study of Refahiye superimposed basin adjacent to the North Anatolian Transform Fault, northeastern Turkey”, *Int. Geol. Rev.*, 38, pp. 701–713, 1996.

Kulakov, I. Yu., S. A. Tychkov, and S. I. Keselman, “Three-dimensional structure of lateral heterogeneities in P-velocities in the upper mantle of the southern margin of Siberia and its preliminary geodynamical interpretation”, *Tectonophysics*, 241, pp. 239–257, 1995.

Laigle, M., A. Becel, B. de Voogd, A. Hirn, T. Taymaz, and S. Ozalaybey, “A first deep seismic survey in the Sea of Marmara: Deep basins and whole crust architecture and evolution”, *Earth planet. Sci. Lett.*, 270(3–4), pp. 168–179, 2008.

Le Pichon, X., and J. J. Angelier, “The Aegean Sea”, *Phil. Trans. R. Soc.*, 300, pp. 357–372, 1981.

Le Pichon, X., J. Angelier, “The Hellenic arc and trench system: a key to the neotectonic evolution of the eastern Mediterranean area”, *Tectonophysics*, 60, pp. 1–42, 1979.

Le Pichon, X., N. Chamot-Rooke, S. L. Lallemand, R. Noomen, and G. Veis, “Geodetic determination of the kinematics of Central Greece with respect to Europe: implications for eastern Mediterranean tectonics”, *Journal of Geophysical Research*, 100, pp. 12675–12690, 1995.

Le Pichon, and X., C. Kreemer, “The Miocene-to-Present kinematic evolution of the Eastern Mediterranean and Middle East and its implications for dynamics”, *Annual Review of Earth and Planetary Sciences*, 38, pp. 323–351, 2010.

Li, C., R. D. van der Hilst, E.R. Engdahl, and S. Burdick, “A new global model for P wave speed variations in Earth's mantle”, *Geochem. Geophys. Geosyst.*, 9, Q05018, 2008.

McClusky, S., S. Balassanian, A. Barka, C. Demir, S. Ergintav, I. Georgiev, O. Gurkan, M. Hamburger, K. Hurst, H. Kahle, K. Kastens, G. Kekelidze, R. King, V. Kotzev, O. Lenk, S. Mahmoud, A. Mishin, M. Nadariya, A. Ouzounis, D. Paradissis, Y. Peter, M. Prilepin, R. Reilinger, I. Sanli, H. Seeger, A. Tealeb, M. N. Toksöz, and G. Veis, “Global Positioning System constraints on plate kinematics and dynamics in the eastern Mediterranean and Caucasus”, *Journal of Geophysical Research*, 105, pp. 5695–5720, 2000.

McClusky, S., R. Reilinger, S. Mahmoud, D. Ben Sari, and A. Tealeb, “GPS constraints on Africa (Nubia) and Arabia plate motions”, *Geophys. J. Int.*, 155, 126–138, 2003.

McKenzie, D.P., “Active tectonics of the Alpine-Himalayan belt: The Aegean Sea and surrounding regions”, *Geophys. J. R. Astron. Soc.*, 55, pp. 217–254, 1978.

McMechan, G.A., “Seismic tomography in boreholes”, *Geophys. J. Royal Astr. Soc.*, 74, pp. 601–612, 1983.

Mutlu, A.K., and H. Karabulut, “Anisotropic Pn tomography of Turkey and adjacent regions”, *Geophysical Journal International*, 187, pp. 1743–1758, 2011.

Nakanishi, I., “Three-dimensional structure beneath the Hokkaido-Tohoku region as derived from a tomographic inversion of P-arrival times”, *J. Phys. Earth*, 33, pp. 241–256, 1985.

Nolet G., “Slabs do not go gently”, *Science*, 324, pp. 1152–1153, 2009.

Notsu, K., T. Fujitoni, T. Ui, J. Matsuda, and T. Ercan, “Geochemical features of collision related volcanic rocks in central and Eastern Anatolia, Turkey”, *J. Volc. Geotherm. Res.*, 64, pp. 171–192, 1995.

Oberhänsli, R., J. Partzsch, O. Candan, M. Cetinkaplan, “First occurrence of Fe–Mg-carpholite documenting a high-pressure metamorphism in meta sediments of the Lycian Nappes, SW Turkey”, *International Journal of Earth Sciences*, 89, pp. 867–873, 2001.

Okay, A. I., “Jadeite-chloritoid-glaucophane-lawsonite blueschists in northwest Turkey: unusually high P/T ratios in continental crust”, *Journal of Metamorphic Geology*, 20 (8), pp. 757–768, 2002.

Özacar, A. A., C. B. Biryol, G. Zandt, and S. L. Beck, “Deep Structure of Continental Strike-slip Faults Imaged by Receiver Functions”, *European Geophysical Union General Assembly 2010*, 2010, Vienna, Austria, 2010.

Pereyra, V., “Modelling, ray tracing, and block nonlinear travel-time inversion in 3D”, *Pure Appl. Geophys.*, 148, pp. 345–386, 1996.

Pereyra, V., W. H. K. Lee, and H. B. Keller, “Solving two-point seismic-ray tracing problems in a heterogeneous medium”, *Bull. Seism. Soc. Am.*, 70, pp. 79–99, 1980.

Piromallo, C., A. Morelli, “P wave tomography of the mantle under the Alpine-Mediterranean area”, *Journal of Geophysical Research: Solid Earth J. Geophys. Res.*, 108, B2, pp. 2156-2202, 2003.

Portner, D.E., J. R. Delph, C. B. Biryol, S. L. Beck, G. Zandt, A. A. Özacar, E. Sandvol, and N. Türkelli, “Subduction termination through progressive slab deformation across Eastern Mediterranean subduction zones from updated P-wave tomography beneath Anatolia”, *Geosphere*, 14(3), pp. 1–19, 2018.

Press, W.H., S. A. Teukolsky, W. T. Vetterling, and B. P. Flannery, *Numerical Recipes in FORTRAN*, Cambridge Univ. Press, New York, USA, 1992.

Price S., and B. Scott, “Fault block rotations at the edge of a zone of continental extension: southwest Turkey”, *J. Struct. Geol.*, 16, pp. 381–392, 1994.

Rawlinson, N., B. L. N. Kennett, and M. Heintz, “Insights into the structure of the upper mantle beneath the Murray basin from 3D teleseismic tomography”, *An International Geoscience Journal of the Geological Society of Australia*, 53:4, pp. 595-604, 2006a.

Rawlinson, N., S. Pozgay, and S. Fishwick, “Seismic tomography: A window into deep Earth”, *Physics of the Earth and Planetary Interiors*, 178, 3–4, pp. 101-135, 2010.

Rawlinson, N., A. M. Reading, and B. L. N. Kennett, “Lithospheric structure of Tasmania from a novel form of teleseismic tomography”, *J. Geophys. Res.*, 111, B2, pp. 2156-2202, 2006b.

Rawlinson, N., and M. Sambridge, “Seismic travelttime tomography of the crust and lithosphere”, *Adv. Geophys.*, 46, pp. 81–198, 2003.

Reilinger R. E., S. C. McClusky, M. B. Oral, W. King, and M. N. Toksöz, “Global Positioning System measurements of present-day crustal movements in the Arabia–Africa–Eurasia plate collision zone”, *J. geophy. Res.*, 102, pp. 9983–9999, 1997.

Reilinger, R., S. McClusky, D. Paradissis, S. Ergintav, and P. Vernant, “Geodetic constraints on the tectonic evolution of the Aegean region and strain accumulation along the Hellenic subduction zone”, *Tectonophysics*, 488, pp. 22–30, 2010.

Reilinger, R., S. McClusky, P. Vernant, S. Lawrence, S. Ergintav, R. Cakmak, H. Ozener, F. Kadirov, İ. Guliev, R. Stepanyan, M. Nadariya, G. Hahubia, S. Mahmoud, K. Sakr, A. ArRajehi, D. Paradissis, A. Al-Aydrus, M. Prilepin, T. Guseva, E. Evren, A. Dmitrotsa, S. V. Filikov, F. Gomez, R. Al-Ghazzi, and G. Karam, “GPS constraints on continental deformation in the Africa–Arabia–Eurasia continental collision zone and implications for the dynamics of plate interactions”, *J. Geophys. Res.*, 111, B004051, 2006.

Richardson-Bunbury, J.M., “The Kula volcanic field, western Turkey: the development of a Holocene alkali basalt province and the adjacent normal-faulting graben”, *Geol. Mag.*, 133, pp. 275–283, 1996.

Rimmelé, G., R. Oberhänsli, O. Candan, B. Goffé, and L. Jolivet, “The wide distribution of HP–LT rocks in the Lycian Belt (Western Turkey): implications for accretionary wedge geometry”, in: Robertson, A.H.F., and D. Mountrakis, (Eds.), *Tectonic Development of the Eastern Mediterranean: Special Publications*. Geological Society, London, pp. 447–466, 2006.

Ring, U., and A.S. Collins, “U–Pb SIMS dating of synkinematic granites: timing of corecomplex formation in the northern Anatolide belt of western Turkey”, *Journal of the Geological Society of London*, 162, pp. 1–10, 2005.

Ring, U., J. Glodny, T. Will, and S. Thomson, “The Hellenic subduction system: high-pressure metamorphism, exhumation, normal faulting, and large-scale extension”, *Annual Review of Earth and Planetary Sciences*, 38, pp. 45–76, 2010.

Ring, U., T. Will, J. Glodny, C. Kumerics, K. Gessner, S. Thomson, T. Güngör, P. Monie, M. Okrusch, and K. Drüppel, “Early exhumation of high-pressure rocks in extrusion wedges: Cycladic blueschist unit in the eastern Aegean, Greece, and Turkey”, *Tectonics*, 26, TC2001, 2007.

Roumelioti, Z., A. Kiratzi, and C. Benetatos, “Time-Domain Moment Tensors for shallow ( $h \leq 40$  km) earthquakes in the broader Aegean Sea for the years 2006 and 2007: the database of the Aristotle University of Thessaloniki”, *Journal of Geodynamics*, 51, pp. 179–189, 2011.

Salaün, G., H. Pedersen, A. Paul, V. Farra, H. Karabulut, D. Hatzfeld, D. M. Childs, C. Pequegnat, and the SIMBAAD Team, “High-resolution surface wave tomography beneath the Aegean-Anatolia region: constraints on upper mantle structure”, *Geophysical Journal International*. 190 (1), pp. 406–420, 2012.

Saltzer, R. L., and E. D. Humphreys, “Upper mantle P wave velocity structure of the eastern Snake River Plain and its relationship to geodynamic models of the region”, *J. Geophys. Res.*, 102, pp. 11829–11841, 1997.

Sambridge, M. S., “Non-linear arrival time inversion: Constraining velocity anomalies by seeking smooth models in 3-D”, *Geophys. J. Int.*, 102, pp. 653–677, 1990.

Savaşçın, M. Y., and T. Oyman, “Tectono-magmatic evolution of alkaline volcanics at the Kırka-Afyon-Isparta structural trend, SW Turkey”, *Turkish J. Earth Sci.*, 7, pp. 201–214, 1998.

Schildgen, T. F., C. Yıldırım, D. Cosentino, and M. R. Strecker, “Linking slab break-off, Hellenic trench retreat, and uplift of the Central and Eastern Anatolian plateaus”, *Earth-Science Reviews*, 128, pp. 147–168, 2014.

Şengör A. M. C., N. Görür, and F. Şaroğlu, “Strike-slip faulting and related basin formation in zones of tectonic escape: Turkey as a case study”, in *Strike-slip Faulting and Basin Formation*, pp. 227–264., Vol. 37, eds Biddle K.T., N. Christie-Blick, Soc. Econ. Paleont. Miner, 1985

Şengör A.M.C., O. Tüysüz, C. İmren, M. Sakıncı, H. Eyidoğan, N. Görür, X. Le Pichon, and C. Claude Rangin, “The North Anatolian Fault. A new look”, *Ann. Rev. Earth planet. Sci.*, 33, pp. 1–75, 2005.

Sethian, J. A. and A. M. Popovici, “3-D travelttime computation using the fast marching method”, *Geophysics*, 64, pp. 516–523, 1999.

Sethian, J. A., “A fast marching level set method for monotonically advancing fronts”, *Proc. Nat. Acad. Sci.*, 93(4), pp. 1591–1595, 1996a.

Sethian, J. A., “Theory, algorithms, and applications of level set methods for propagating interfaces”, *Acta Numerica*, 5, pp. 309–395, 1996b.

Seyitoğlu G., and B. C. Scott, “Late Cenozoic crustal extension and basin formation in west Turkey”, *Geol. Mag.*, 128, 155–166, 1991.

Seyitoğlu G., B. C. Scott, and C. C. Rundle, “Timing of Cenozoic extensional tectonics in west Turkey”, *J. Geol. Soc., Lond.*, 149, pp. 533–538, 1992.

Shaw, P. R., and A. Orcutt, “Waveform inversion of seismic refraction data and applications to young Pacific crust”, *Geophys. J. Royal Astr. Soc.*, 82, pp. 375–414, 1985.

Sobolev, S.V., H. Zeyen, G. Stoll, F. Werling, R. Altherr, and K. Fuchs, “Upper mantle temperatures from teleseismic tomography of French Massif Central including effects of composition, mineral reactions, anharmonicity, anelasticity and partial melt”, *Earth Planet. Sci. Lett.*, 139, pp. 147–163, 1996.

Sodoudi, F., R. Kind, D. Hatzfeld, K. Priestley, W. Hanka, K. Wylegalla, G. Stavrakakis, A. Vafidis, H.P. Harjes, and M. Bohnhoff, “Lithospheric structure of the Aegean obtained from P and S receiver functions”, *Journal of Geophysical Research*, 111, B12307, 2006.

Spakman W., “A Tomographic Image of the Upper Mantle in the Eurasian-African-Arabian Collision Zone”, *EOS*, 66, pp. 975, 1985.

Spakman, W., and R. Wortel, “A tomographic view on Western Mediterranean Geodynamics”, in: *The TRANSMED Atlas, The Mediterranean Region from Crust to Mantle*, Edited by: Cavazza W., F. Roure , W. Spakman, G. M. Stampfli , and P. Ziegler, pp. 31-52, 2004.

Spakman, W., M. J. R. Wortel, and N. J. Vlaar, “The Hellenic subduction zone: a tomographic image and its geodynamic implications”, *Geophysical Research Letters*, 15, pp. 60–63, 1988.

Steck, L. K., C. H. Thurber, M. Fehler, W. J. Lutter, P. M. Roberts, W. S. Baldrige, D. G. Stafford, and R. Sessions, “Crust and upper mantle P wave velocity structure beneath Valles caldera, New Mexico: results from the Jemez teleseismic tomography experiment”, *J. Geophys. Res.*, 103, pp. 24301–24320, 1998.

Suckale, J., S. Rondenay, , M. Sachpazi, , M. Charalampakis, , A. Hosa, , and L. H. Royden, “High-resolution seismic imaging of the western Hellenic subduction zone using teleseismic scattered waves”, *Geophysical Journal International*, 178, pp. 775–791, 2009.

Tarantola, A., *Inverse Problem Theory and Methods for Model Parameter Estimation*, Society for Industrial and Applied Mathematics, PA, USA, 1987

Taymaz T., and S. P. Price, “The 12.05.1971 Burdur earthquake sequence: a synthesis of seismological and geological observations”, *Geophys. J. Int.*, 108, pp. 589–603, 1992.

Taymaz T., T. Wright, S. Yolsal, O. Tan, E. Fielding, and G. Seyitoğlu, “Source Characteristics of June 6, 2000 Orta-Çankırı (Central Turkey) Earthquake: a synthesis of seismological, geological and geodetic (InSAR) observations, and internal deformation of Anatolian plate”, *J. Geol. Soc., Lond.*, 291, pp. 259–290, 2007b.

Taymaz T., Y. Yılmaz, and Y. Dilek, “The Geodynamics of the Aegean and Anatolia: Introduction”, in *The Geodynamics of the Aegean and Anatolia*, eds Taymaz T., Y. Yılmaz, Y. Dilek, *J. Geol. Soc., London, Special Publications*, 29, pp. 1–16, 2007a.

Taymaz, T., J. A. Jackson, and D. McKenzie, “Active Tectonics of the North and Central Aegean Sea”, *Geophysical Journal International-Oxford*, 106, pp. 433-490, 1991.

ten Veen J.H., M. Woodside, T. A. C. Zitter, J. F. Dumont, J. Mascle, and A. Volkonskaia, “Neotectonic evolution of the Anaximander Mountains at the junction of the Hellenic and Cyprus Arcs”, *Tectonophysics*, 391, pp. 35–65, 2004.

Thurber, C. H., “Earthquake locations and three-dimensional crustal structure in the Coyote Lake area, central California”, *J. Geophys. Res.*, 88, pp. 8226–8236, 1983.

Thurber, C. H., “Local earthquake tomography: velocities and  $V_P/V_S$  – theory”, in: Iyer H., K. Hirahara (Eds.), *Seismic Tomography: Theory and Practice*, Chapman and Hall, London, 1993, pp. 563-583, 1993.

Tirel, C., J. P. Brun, and E. Burov, “Thermo-mechanical modeling of extensional gneiss domes”, In: Whitney, D.L., Teyssier, C., Siddoway, C.S. (Eds.), *Gneiss Domes in Orogeny: Geological Society of America Special Paper*, Boulder, Colorado, pp. 67–78, 2004.

Tokçaer, M., S. Agostini, and M. Y. Savaşçın, “Geotectonic setting, origin and emplacement model of the youngest Kula Volcanics in Western Anatolia”, *Turkish Journal of Earth Sciences*, 142, pp. 145–166, 2005.

van Hinsbergen, D. J. J., N. Kaymakci, W. Spakman, T. H. Torsvik, “Reconciling the geological history of western Turkey with plate circuits and mantle tomography”, *Earth and Planetary Science Letters*, 297, pp. 674–686, 2010.

Vidale, J. E., “Finite-difference calculations of traveltimes”, *Bull. Seism. Soc. Am.*, 78, pp. 2062-2076, 1988.

Vidale, J. E., “Finite-difference calculations of traveltimes in three dimensions”, *Geophysics*, 55, pp. 521-526, 1990.

Wdowinski S., Z. Ben-Avraham, R. Arvidsson, and G. Ekstrom, “Seismo-tectonics of the Cyprus Arc”, *Geophys. J. Int.*, 164, pp. 176–181, 2006.

Wesson, R. L., “Travel-time inversion for laterally inhomogeneous crustal velocity models”, *Bull. Seismol. Soc. Amer.*, 61, pp. 729-746, 1971.

Wittlinger, G., P. Tapponier, G. J. Poupinet, J. Mei, S. Danian, G. Herquel, F. Masson, “Tomographic evidence for localized lithospheric shear along the Altyn Tagh Fault”, *Science*, 282, pp. 74–76, 1998.

Wortel, M.J.R., and W. Spakman, “Structure and dynamic of subducted lithosphere in the Mediterranean”, *Proceedings of the Koninklijke Nederlandse Akademie van Wetenschappen*, 95 (3), pp. 325–347, 1992.

Wortel, M.J.R., and W. Spakman, “Subduction and slab detachment in the Mediterranean–Carpathian region”, *Science*, 290, pp. 1910–1917, 2000.

Zhu, H., E. Bozdag, D. Peter, and J. Tromp, “Structure of the European upper mantle revealed by adjoint tomography”, *Nat. Geosci.*, 5, pp. 493–498, 2012.

Zhu, H., and J. E. Ebel, “Tomographic inversion for the seismic velocity structure beneath northern New England using seismic refraction data”, *J. Geophys. Res.*, 99, pp. 15331–15357, 1994.